

General Disclaimer

One or more of the Following Statements may affect this Document

- This document has been reproduced from the best copy furnished by the organizational source. It is being released in the interest of making available as much information as possible.
- This document may contain data, which exceeds the sheet parameters. It was furnished in this condition by the organizational source and is the best copy available.
- This document may contain tone-on-tone or color graphs, charts and/or pictures, which have been reproduced in black and white.
- This document is paginated as submitted by the original source.
- Portions of this document are not fully legible due to the historical nature of some of the material. However, it is the best reproduction available from the original submission.

NASA CR-135246
Univ. of Ill. ME-TR-395-4

VISCID-INVISCID INTERACTION ASSOCIATED WITH
INCOMPRESSIBLE FLOW PAST WEDGES AT HIGH
REYNOLDS NUMBER

N. R. Warpinski and W. L. Chow

University of Illinois at Urbana-Champaign
Urbana, Illinois 61801

{NASA-CR-135246} VISCID-INVISCID
INTERACTION ASSOCIATED WITH INCOMPRESSIBLE
FLOW PAST WEDGES AT HIGH REYNOLDS NUMBER
Final Report (Illinois Univ.,
Urbana-Champaign.) 142 p HC A07/HF A01

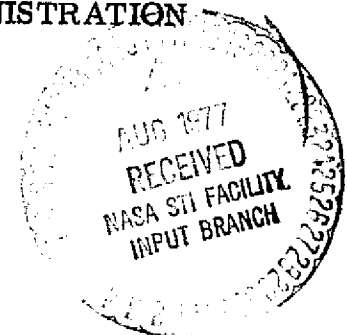
N77-28072

G3/02 Unclass
40712

Prepared for
NATIONAL AERONAUTICS AND SPACE ADMINISTRATION
Lewis Research Center
Cleveland, Ohio 44135

August 1977

Grant NGL-14-005-140



1. Report No. NASA CR-135246		2. Government Accession No.		3. Recipient's Catalog No.	
4. Title and Subtitle VISCID-INVISCID INTERACTION ASSOCIATED WITH INCOMPRESSIBLE FLOW PAST WEDGES AT HIGH REYNOLDS NUMBER				5. Report Date August 1977	
				6. Performing Organization Code	
7. Author(s) N. R. Warpinski and W. L. Chow				8. Performing Organization Report No. ME-TR-395-4	
9. Performing Organization Name and Address University of Illinois at Urbana-Champaign Urbana, Illinois 61801				10. Work Unit No.	
				11. Contract or Grant No. NGL-14-005-140	
12. Sponsoring Agency Name and Address National Aeronautics and Space Administration Washington, D.C. 20546				13. Type of Report and Period Covered Contractor Report	
				14. Sponsoring Agency Code	
15. Supplementary Notes Final report. Project Managers, Lawrence J. Bober and Bernhard H. Anderson, both of Wind Tunnel and Flight Division, NASA Lewis Research Center, Cleveland, Ohio 44135. Report is based on a thesis submitted by the first author in partial fulfillment of the requirements for the degree Doctor of Philosophy to the University of Illinois at Urbana-Champaign, Urbana, Illinois, in February 1977.					
16. Abstract An analytical method is suggested for the study of the viscid-inviscid interaction associated with incompressible flow past wedges with arbitrary angles. It is shown from this analysis that the determination of the nearly constant pressure (base pressure) prevailing within the near wake is really the heart of the problem, and this pressure can only be established from these interactive considerations. The basic free streamline flow field is established through two discrete parameters which should adequately describe the inviscid flow around the body and the wake. The viscous flow processes such as the boundary layer buildup, turbulent jet mixing, and recompression are individually analyzed and attached to the inviscid flow in the sense of the boundary layer concept. The interaction between the viscous and inviscid streams is properly displayed by the fact that the aforementioned discrete parameters needed for the inviscid flow are determined by the viscous flow condition at the point of reattachment. It is found that the reattachment point behaves as a saddle point singularity for the system of equations describing the recompressive viscous flow processes, and this behavior is exploited for the establishment of the overall flow field. Detailed results such as the base pressure, pressure distributions on the wedge, and the geometry of the wake are determined as functions of the wedge angle. The influence of the boundary layer thickness prior to separation, as well as the spread rate parameter within the turbulent mixing region, is demonstrated. The wind tunnel wall interference effect has been examined, and the difficulty in comparing the results with experimental data is also indicated. Experimental exploration of the mean and fluctuating turbulent velocities in the wake and redevelopment regions through hot wire probing has been carried out for the flow past a backward facing step. The results are presented to provide assistance for future studies of the flow redevelopment after reattachment.					
17. Key Words (Suggested by Author(s)) Incompressible flow; Wedge flow; Base flow; Viscid-inviscid interaction			18. Distribution Statement Unclassified - unlimited STAR Category 02		
19. Security Classif. (of this report) Unclassified		20. Security Classif. (of this page) Unclassified		21. No. of Pages 141	
				22. Price*	

* For sale by the National Technical Information Service, Springfield, Virginia 22161

TABLE OF CONTENTS

	Page
1. INTRODUCTION-----	1
2. THEORETICAL ANALYSIS-----	9
2.1 CORRESPONDING INVISCID FLOW-----	9
2.2 ANALYSIS OF THE VISCOUS FLOW-----	14
2.2.1 Initial Boundary Layer-----	15
2.2.2 Quasi-constant Pressure Turbulent Jet Mixing Region-----	17
2.2.3 Recompression Region-----	21
2.2.3.1 Upper Layer-----	22
2.2.3.2 Wake Flow Region-----	24
2.2.3.3 Computational Form of the Equations-----	26
2.3 METHOD OF CALCULATION-----	29
3. RESULTS AND DISCUSSION OF THEORETICAL CALCULATIONS-----	31
4. EXPERIMENTAL INVESTIGATION-----	42
4.1 APPARATUS AND INSTRUMENTATION-----	42
4.1.1 Wind Tunnel Facility-----	42
4.1.2 Test Section-----	43
4.1.3 Hot Wire Anemometry-----	44
4.2 CALIBRATION-----	45
4.3 EXPERIMENTAL TECHNIQUES-----	46
5. RESULTS AND DISCUSSION OF THE EXPERIMENTAL INVESTIGATION-----	47
6. CONCLUSIONS-----	50
REFERENCES-----	119
APPENDIX A THE CORRESPONDING INVISCID FLOW WITH A TOP WALL BOUNDARY-----	123
APPENDIX B DETERMINATION OF THE POTENTIAL FLOW VELOCITY NEAR THE LEADING EDGE OF A WEDGE-----	131

NOMENCLATURE

c_1, c_2	general constants
c_f	coefficient of the shear stress on the wall
C_D	drag coefficient
C_p	pressure coefficient
C_{p_b}	base pressure coefficient
E	anemometer output voltage
E_o	anemometer output voltage at zero velocity
E_{out}	linearizer output voltage
F_1, F_2	velocity profile integrals
g	constant of proportionality defined in Eq. (2.62)
h_b	height of reverse flow region
H	step height
k_1, k_2, k_3, k_4	parameters of the corresponding inviscid flow
K_1, K_2	constants appearing in APPENDIX B
K_o	constant gain of the linearizer output
ℓ	intermediate mapping plane for inviscid flow with a top-wall boundary
ℓ_m	length of the mixing region
m	power of x in Faulkner-Skan flow
M_e	Mach number at the outer edge of the viscous layer
n	power of the initial boundary layer profile
p	pressure
p_b	base pressure
p_e	pressure at the outer edge of the viscous layer for compressible flow
p_w	pressure on the wall
p_a	pressure at the outer edge of the viscous layer

P_{∞}	freestream pressure
\bar{q}	complex velocity
R	height of the top wall upstream of the step
R_c	radius of curvature
Re_H	Reynolds number of the approaching flow
R_f	height of the top wall downstream of the step
$R_{\delta^{**}}$	Reynolds number base on the momentum thickness
s	slope of the velocity profile at the dividing streamline
t	final mapping plane for the inviscid flow
t'	final mapping plane for the inviscid flow past a backstep
T	thickness of the viscous layer
u	velocity in the x direction
u'	fluctuating component of the velocity in the x direction
\bar{U}	mean velocity in the x direction
U_a	velocity at the outer edge of the viscous layer
U_b	maximum velocity in the reverse flow region
U_d	velocity at the dividing streamline
U_m	velocity at the edge of the mixing region
U_s	velocity at the step
v	velocity in the y direction
v'	fluctuating component of the velocity in the y direction
v_a	normal velocity at the outer edge of the viscous layer
v_d	normal velocity at the dividing streamline
\bar{V}	mean velocity in the y direction
V_e	velocity at the edge of the viscous layer for compressible flow
V_o	velocity of the free streamline
V_s	longitudinal velocity in curvilinear coordinates

V_{∞}	freestream velocity
$V_{\infty A}$	upstream, freestream velocity for flow with a top wall boundary
$V_{\infty F}$	downstream, freestream velocity for flow with a top wall boundary
W	complex potential plane
x	horizontal coordinate
x_r	length along the recompression region
y	vertical coordinate
y_1	vertical coordinate at the separation point
y_d	location of the dividing streamline
y_m	location of the upper edge of the mixing layer
z	complex coordinate of the physical plane
α	recompression angle
β_a	flow angle at the outer edge of the viscous layer
γ	ratio of specific heats
δ_1	thickness of the boundary layer at the separation point
δ_a	thickness of the viscous layer above the dividing streamline
δ_b	thickness of the viscous layer below the dividing streamline
δ^*	displacement thickness
δ^{**}	momentum thickness
ϵ	eddy diffusivity
$\bar{\epsilon}$	dimensionless eddy diffusivity
ζ	intermediate mapping plane for the inviscid flow
ζ_1	normalized normal coordinate at the separation point
ζ_b	normalized vertical coordinate of the reverse flow region
ζ_l	normalized vertical coordinate of the lower viscous layer

ζ_m	normalized vertical coordinate at edge of mixing layer
ζ_u	normalized vertical coordinate of the upper viscous layer
η	transformed coordinate of the mixing process
θ	wedge half angle
ν	kinematic viscosity
ξ_1, ξ_2	transformation of the inviscid flow near singularities
ρ	density
ρ_e	density at the outer edge of the viscous layer for compressible flow
σ	spread rate parameter
τ	shear stress
τ_d	shear stress along the dividing streamline
ϕ	normalized velocity
ϕ_b	normalized maximum velocity in the reverse flow region
ϕ_d	normalized velocity at the dividing streamline
ϕ_m	normalized velocity at the outer edge of the mixing layer
ϕ_D	proportionality constant defined in Eq. (2.6)
ω	intermediate mapping plane of the inviscid flow

SUBSCRIPTS

a	outer edge of the viscous layer
b	region below the dividing streamline
d	dividing streamline
D	point D
e	outer edge of the viscous layer for compressible flow
F	point F
l	lower viscous layer
m	mixing region
u	upper viscous layer
∞	freestream condition

1. INTRODUCTION*

Investigations of flows over bluff bodies conducted since the early part of this century resulted in a slow unraveling of the processes and mechanisms which control and establish these flows. In the classical potential theory, the fluid is assumed to hug the body contour and the drag coefficient so obtained from the pressure distribution on the blunt body is zero regardless of the body shape. This is completely unrealistic since experimental observations clearly indicate that the drag is substantial and dependent upon the body shape. It was also recognized that this drag cannot be entirely accounted for solely from skin friction on the surface. The inherent feature of these flows is the occurrence of separation which drastically modifies the pressure distribution on the body.

The first significant improvement of the classical theory was achieved by Kirchoff [2]**. He introduced a model with a free streamline which separates from the body and extends to infinity leaving a wake behind the body. The pressure inside the wake region was assumed to be the same as that of the undisturbed free stream flow. Although this model was far superior to the classical model, the drag coefficient was still considerably underestimated.

Riabouchinsky [3] realized that the wake was closed and introduced a mirror image of the body to simulate downstream reattachment of the free streamline. Obviously the drag on the two-body system is zero. However, if it is stipulated that the cavity region is under a low

*The major part of the material discussed in this report is based on a Ph.D. thesis by the first author [1].

**Numbers in brackets refer to entries in REFERENCES.

pressure condition (obtained from experiments), the drag on the front body can be evaluated.

Von Karman, et al. [4], recognized that the wake region was not under a steady flow condition and devised a theory to account for the effect of periodic vortex shedding. Again, empirical data was required to obtain results. Heisenberg [5] improved Von Karman's analysis and obtained good agreement for the drag on a flat plate normal to the flow, but his analysis yielded the same value for any other shaped cylinder.

In an attempt to improve the original Kirchhoff analysis, other investigators employed inviscid models to obtain a more accurate drag coefficient. Kreisel [6] and Efros [7] proposed the reentrant jet model in which the bounding free streamline reverses its direction near the end of the wake to form a reverse jet flow. Some investigators favored this model because of its marginal resemblance to real wake flows. Eppler [8], Roshko [9], and Wu [10] employed a "dissipative wake model" in which the near wake region, extending downstream from the separation point to some undetermined location, follows a free streamline and the far wake region is described by a potential flow whose pressure increases continuously toward the original free stream value. All these methods, however, employ the experimentally observed value of the base pressure as a parameter in order to determine the drag coefficient. Recently, Parkinson and Jandali [11] tried to reproduce experimentally observed pressure distribution on the circular cylinder immersed in a uniform flow. They require, in addition to the base pressure, also the location of the point of separation as input to their analysis. Since the governing equation is of the elliptic nature, the pressure distribution and thus the drag coefficients so obtained should be in good agreement with

the experimental data (see discussion). The determination of the base pressure, which is the principle contributor to the pressure drag, was not considered by these investigators.

It is understood today that the inviscid analyses alone are incapable of dealing with the base pressure problem even in an approximate manner because the overall flow pattern is an ultimate result of the interaction between the viscid and inviscid streams. The basic flow mechanisms were pointed out by Crocco and Lees [12] in their original study of the interaction problems within the high-speed flow regime. It is realized that although the inviscid stream guides and controls the viscous flow processes occurring along and within the wake region in the sense of the boundary layer concept, the configuration and structure of the inviscid flow, as well as the value of the base pressure, are influenced by the viscous flow mechanisms.

In order to establish a model for these problems, it was first necessary to identify the viscous flow processes occurring along the jet boundary and account for its interaction with the inviscid stream. For supersonic approaching flows, this interaction study has been carried out along two distinct avenues. One approach, which is now called the Korst-Chapman model, delineates the individual flow components associated with the flow and obtains solutions for the problem by integrating the analyses for these components.

Korst, in his consideration of supersonic turbulent base pressure problems [13], divided the region into components of (1) flow expansion around the corner, (2) turbulent mixing along the constant pressure jet boundary, (3) recompression-reattachment of the viscous layer at the end of the wake, and (4) redevelopment of flow downstream of the wake.

Chapman [14,15] had similar considerations for the laminar flow. He employed Korst's original "discriminating criterion" to determine the resulting base pressure, namely, that the stagnation pressure of the dividing streamline at the end of the mixing region should be equal to the static pressure of the adjacent freestream prevailing at the end of the wake. He also extended this consideration to incompressible flow problems [15,16]. Solutions were obtained for vanishing initial boundary layer thickness ahead of the mixing region so that the results are the lowest possible base pressure within the respective flow regimes (which correspond to the highest Reynolds numbers). In any actual physical situation, the flow at the end of the mixing region would not be fully developed due to the presence of the initial boundary layer of the flow approaching the base of the body. Carriere and Sirieix [17], Golik [18], and Nash [19] investigated the effect of these approaching boundary layers on the base flow phenomena.

Experimental evidence, however, has repeatedly shown that the pressure at the point of reattachment is considerably less than that prevailing in the adjacent freestream. Nash [19,20] later suggested the introduction of a recompression coefficient to correlate these pressure levels. It was found experimentally that this factor was also Mach and Reynolds number dependent and it could not be established analytically.

McDonald [21,22] tried to improve the Korst-Chapman model by considering the redeveloping flow after reattachment. He stipulated that the value of the boundary layer shape parameter at the end of the pressure rise should be equal to that of a flow over a flat plate.

The second approach is based on Crocco and Lees mixing theory [12]. Lees and Reeves [23,24] formulated a theory for supersonic laminar flows

by considering the moment of momentum equation along with the basic conservation laws. The equations were integrated along the recompression region and it was found that the system of equations possesses a critical point downstream of the point of reattachment. The solution of this problem is obtained from the assumed base pressure which allows the calculations to proceed smoothly through this critical point. Alber and Lees [25,26] extended the analysis to consider supersonic turbulent separated flows, and the base pressure results were too high when compared with the experimental data. Shamroth and McDonald [27] included the normal momentum equation in their analysis and devised a method of solution that eliminated the saddle-point-type singularity downstream of the reattachment point. Reviews of previous work dealing with supersonic base pressure problems were provided earlier by Korst, et al. [28], and recently by Carpenter and Tabakoff [29], Chang [30], Berger [31], and Page [32].

Most of the analyses mentioned previously were based exclusively on the boundary layer concept. Experiments have shown, however, that for supersonic flows, there is a considerable pressure difference across the turbulent viscous layer near the reattachment point. Chow and Spring [33, 34] accounted for this effect on the recompression process. They divided the viscous flow into two subregions along the dividing streamline and applied the conservation principles, including the normal momentum equation, to these two subregions. In conjunction with the flow conditions prevailing at the end of the constant pressure jet mixing region, the system of equations was integrated numerically. These procedures fully illustrated the elliptic nature of separated flow problems since the downstream flow conditions, particularly with the regions of recompression and redevelopment, offer predominant influences to the solution.

In addition, in their study of the redevelopment after reattachment with a supersonic external stream, they recognized that the pressure difference across the viscous layer is important and they suggested that the process of redevelopment can be treated as a relaxation of this pressure difference [35]. They further showed that the fully relaxed asymptotic flow condition is a saddle-point-type singularity for the system of equations governing the flow which would also provide the closure condition for the problem. A method of solution was developed for this flow field and good agreement with experimental data was obtained. Weng [36] extended the Chow and Spring method [33,35] to supersonic axially symmetric flow problems. Calculations for isoenergetic flow cases for three Mach numbers with various sting radius ratios were performed; good agreement with experimental data was observed.

Separated flow problems always exhibit elliptic behavior even though the governing equations of the external inviscid stream may be hyperbolic in nature. For supersonic flows, this hyperbolic character of the external stream considerably simplifies the establishment of the external inviscid flow. For incompressible flows, the elliptic nature of the problem results from the characteristics of the inviscid external stream as well as the viscous interaction, a feature that greatly increases the complexity of the problem. An early attempt to study the incompressible viscid-inviscid interaction was made by Green [37] who suggested that the thin air foil theory be employed to determine the external inviscid flow, and the required source distribution is determined from viscous flow considerations. No successful calculations were produced, however.

Tanner [38] conducted an extensive experimental investigation of base pressure problems associated with incompressible flows over wedges and

obtained detailed pressure measurements as well as the approximate dimensions of the closed wake bubbles. He further presented a model for wedges at an angle of attack in an incompressible flow [39] and conducted a series of experiments [40] to determine the effect of Reynolds number and boundary layer thickness on the base pressure. He observed that the base pressure coefficient decreases with decreasing boundary layer thickness. Later he presented a semi-empirical theory [41,42] in which he correlated the base pressure and the base drag with a volumetric coefficient of outflow from the wake and observed good agreement with experimental data for the base pressure results. In his publication [42], he pointed out that previous considerations by Chapman [15] are inadequate, even though it has been widely quoted [16]. He also presented a relation between the spread rate parameter for the turbulent jet mixing process as a function of wedge angle. Schlichting [43] reviewed Tanner's work and presented improved values for this spread rate parameter σ .

Based on the experience of studying the viscid-inviscid interaction problem with supersonic approaching flows, Chow and Spring [44] presented a method to analyze incompressible flow over a two-dimensional backstep. Upon employing the conformal mapping technique in conjunction with the free streamline theory, a flow model was devised to treat this type of problem. The basic idea of accounting for the interaction lies in the description of the corresponding inviscid flow through certain discrete parameters and the analysis of the viscous flow, which must be attached and guided by the inviscid flow, serves to determine the correct values of these parameters. Turbulent viscous processes within the recompression region was considered and an empirical expression to estimate the eddy diffusivity along the dividing streamline under such situations was introduced. It was found that for incompressible flows, the pressure difference

across the viscous layer is negligibly small and the boundary layer simplifications were subsequently employed [45] for the recompression region. The resulting base pressure showed good agreement with experimental data from Tanner [41,42] and Tani [46]. The influences of the initial boundary layer prior to mixing and the spread rate parameter of the mixing process were also investigated.

In the present work, the same philosophy is implemented to study the separated flow problems associated with incompressible flow past a wedge with an arbitrary angle. Indeed, it will be seen that it is very fruitful to examine flow problems associated with a wedge on such a basis, and the previous investigation of the flow over a backward facing step [45] becomes a special case of the present general analysis. In addition, the possible effect of interference from the top bounding wall (such as the case with a wind tunnel wall) has also been examined. It is also recognized that redevelopment of flow after reattachment usually offers a unique example with a non-equilibrium turbulent structure as its special feature.

2. THEORETICAL ANALYSIS

For an incompressible flow past a wedge, it is expected that the flow stagnates at the front tip of the wedge and accelerates along the surface afterwards until a low pressure is reached at the base of the wedge. Thereafter, the flow separates and a low pressure wake region extends some distance downstream behind the body. For sufficiently large Reynolds numbers, a turbulent jet mixing process occurs along the wake boundary. Near the end of the wake, the fluid must realign itself to the original flow direction initiating a recompression process. As a result of this recompression, a portion of the fluid is turned back to form the recirculating wake flow while the rest of the fluid proceeds downstream. After the flow reattaches to the wall, the fluid undergoes a redevelopment process until the original freestream pressure is restored at far downstream locations.

As pointed out by Chow and Spring [44,45], if a suitable inviscid flow field can be established, the viscous flow process can be attached to and guided by the inviscid stream in the sense of the boundary layer concept. The geometry or configuration of this corresponding inviscid flow, however, is dependent upon the viscous flow processes. It is obvious that the viscous and inviscid streams play equally important roles in the establishment of the flow field and this type of phenomenon has been classified as "strong interaction."

2.1 CORRESPONDING INVISCID FLOW

The basic idea of the analysis lies in the establishment of a corresponding inviscid flow which adequately approximates the actual inviscid flow. The particular model utilized in this analysis is similar to the one employed by Chow and Spring [44,45]. It is, however, a general one in that it will

accommodate a wedge of any arbitrary angle including a flat plate normal to the flow and the limiting case of a rearward facing step. The corresponding inviscid flow established in the manner shown in Fig. 2.1a hopefully would describe the behavior of the inviscid portion of the flow when a wedge of angle θ is inserted in a uniform infinite stream. If one assumes that the flow is symmetric about the centerline, only the upper half plane needs to be considered. This would also imply that a splitter plate must exist along the centerline of the wake to suppress the unsteady-alternating-vortex shedding at the base. It is stipulated that the fluid on the bounding streamline of this half plane decelerates as it approaches the wedge and stagnates at point B. At this location, it changes direction and then accelerates over the face of the wedge. At the base of the wedge (point C), the streamline separates from the body and follows a constant pressure boundary (a free streamline of constant velocity) until the flow has turned into an angle α with respect to the centerline at point D. It is then assumed that the recompression process follows a straight line path until it intersects the centerline at point E. This point, however, should not be confused with the reattachment point of the actual flow. Subsequently, the flow accelerates until it reattains the original free stream condition at far downstream locations. The corresponding hodograph for this model is shown in Fig. 2.1b where

$$\bar{q} = u - i v = \frac{1}{v_0} \frac{dW}{dz} \quad (2.1)$$

as it is usually defined for a potential flow. Figure 2.2a shows the graph in the ζ plane which is defined as the inverse of the hodograph variable, i.e.:

$$\zeta = 1/\bar{q} \quad (2.2)$$

and Fig. 2.2b represents the mapping obtained by employing the transformation

$$\omega = \ln \zeta \quad (2.3)$$

The graph in the ω plane is polygonal so that a Schwarz-Christoffel transformation of the form

$$\omega = c_1 \int \frac{dt}{\left(t + \frac{1}{k_1}\right)\left(t - \frac{1}{k_2}\right)\sqrt{1-t^2}} + c_2 \quad (2.4)$$

can be used to map the polygon into the upper half of the t -plane as shown in Fig. 2.2c. k_1 and k_2 are unknown parameters which must be determined from the analysis and c_1 and c_2 are constants to be evaluated from conditions of

$$\omega(t = 1) = -i\alpha \quad \text{and} \quad \omega(t = -1) = i\theta \quad (2.5)$$

The final W -plane can be obtained from the t -plane by setting

$$W = \Phi_D t \quad (2.6)$$

where Φ_D is a constant and is the value of the velocity potential at point D ($t = 1$). If the transformation given by Eq. (2.4) is examined around either the singularity at $t = 1$ or $t = -1$, an additional relationship of

$$\sqrt{\frac{k_2^2}{1 - k_2^2}} = \frac{\alpha}{\theta} \sqrt{\frac{k_1^2}{1 - k_1^2}} \quad (2.7)$$

can be obtained.

Upon carrying out the integration of Eq. (2.4) and determining the constants c_1 and c_2 , the conjugate velocity \bar{q} is found to be given by

$$\bar{q} = \frac{1}{\zeta} = \left[\frac{t - \frac{1}{k_2}}{\sqrt{\left(\frac{1}{k_2^2} - 1\right)(t^2 - 1) + \frac{t}{k_2} - 1}} \right]^{\alpha/\pi} \left[\frac{t + \frac{1}{k_1}}{\sqrt{\left(\frac{1}{k_1^2} - 1\right)(t^2 - 1) + \frac{t}{k_1} + 1}} \right]^{\theta/\pi} \quad (2.8)$$

The velocity ratio v_0/v_∞ can be determined by taking the limit of Eq. (2.8) as $t \rightarrow +\infty$. The expression for the inverse of \bar{q} for this condition reduces into

$$\bar{r}_\infty = \frac{1}{\bar{q}_\infty} = \frac{v_0}{v_\infty} = \left[\sqrt{\frac{1}{k_2^2} - 1} + \frac{1}{k_2} \right]^{\alpha/\pi} \left[\sqrt{\frac{1}{k_1^2} - 1} + \frac{1}{k_1} \right]^{\theta/\pi} \quad (2.9)$$

which is directly related to the base pressure coefficient from Bernoulli's equation according to

$$c_{p_b} = \frac{p_b - p_\infty}{\frac{1}{2} \rho v_\infty^2} = 1 - \left(\frac{v_0}{v_\infty} \right)^2 \quad (2.10)$$

Since v_0 is the velocity along the constant pressure boundary, it is clear that the parameters α , k_1 , and k_2 are related to the base pressure coefficient. In view of Eq. (2.7), only two of these parameters are independent, however.

The velocity at any location in the t -plane can be determined from Eq. (2.8). To utilize this equation, however, it is necessary to relate the location in the t -plane to the location in the physical plane. This is accomplished by rewriting Eq. (2.1) as

$$\frac{v_0 H}{\Phi_D} \frac{d(z/H)}{dt} = \left[\frac{\sqrt{\left(\frac{1}{k_2^2} - 1\right) (t^2 - 1)} + \frac{t}{k_2} - 1}{t - \frac{1}{k_2}} \right]^{\alpha/\pi} \cdot \left[\frac{\sqrt{\left(\frac{1}{k_1^2} - 1\right) (t^2 - 1)} + \frac{t}{k_1} + 1}{t + \frac{1}{k_1}} \right]^{\theta/\pi} \quad (2.11)$$

where relations from Eqs. (2.6) and (2.8) have been inserted and H has been introduced as a length of normalization.

To determine the scale factor $v_0 H/\Phi_D$, it is necessary to integrate the expression on the right-hand side of Eq. (2.11) from $-(1/k_1)$ to -1 in the t -plane which corresponds to the distance from B to C in the physical plane and the factor $v_0 H/\Phi_D$ is such that the two sides of the above equation agree. The correspondence of the locations in both the t -plane and the physical plane is established through numerical integration of Eq. (2.11). The integration must be handled carefully near the singularities of $t = -(1/k_1)$ and $t = 1/k_2$. Transformation of

$$\xi_1 = \left[\frac{t + \frac{1}{k_1}}{-1 + \frac{1}{k_1}} \right]^{\theta/\pi} \quad \text{or} \quad \xi_2 = \left[\frac{t - \frac{1}{k_2}}{1 - \frac{1}{k_2}} \right]^{\alpha/\pi} \quad (2.12)$$

should be employed wherever one of these singularities appears as the limit of integration. Finally, it should be noted that the negative branch of both of the square root functions within Eq. (2.11) must be employed when $t < -1$. Equation (2.11) can now be integrated from $t = -1$ to $t = +1$ to trace the configuration of the free streamline CD and also the inviscid rear stagnation point E. This essentially establishes the corresponding inviscid flow.

It should be mentioned that the transformations presented above for a wedge reduce to those for the backstep problem as $\theta \rightarrow 0$. From Eq. (2.7), as $\theta \rightarrow 0$, k_1 must approach to zero and point B will coincide with point A. Under this condition, Eq. (2.8) becomes

$$\frac{1}{\zeta} = \left[\frac{t - \frac{1}{k_2}}{\sqrt{\left(\frac{1}{k_2^2} - 1\right)(t^2 - 1)} + \frac{t}{k_2} - 1} \right]^{\alpha/\pi} \quad (2.13)$$

which is equivalent to

$$\frac{1}{\zeta} = \left[\frac{t' - 1}{2k \sqrt{\left(t'^2 + \frac{t'}{k}\right)\left(\frac{1+k}{k}\right)} + (1 + 2k) t' + 1} \right]^{\alpha/\pi} \quad (2.14)$$

as presented by Chow and Spring [44,45] for the backstep configuration shown in Fig. 2.3. This equivalence can be easily observed when expression of

$$t' = \frac{t - 1}{\frac{1}{k_2} - 1} \quad (2.15)$$

and

$$\frac{1}{k_2} = (1 + 2k) \quad (2.16)$$

are employed to relate the variables t' and t and the parameters k_2 and k in the two presentations.

2.2 ANALYSIS OF THE VISCOUS FLOW

It has been pointed out in Chapter 1 that the viscous flow processes are equally important in the establishment of the overall flow field. Specifically, within the framework of the flow model adopted for this present study, the viscous flow analysis serves to determine the correct values of k_1 and α which are intimately related to the establishment of the corresponding inviscid flow.

It is recognized that initially a wall boundary layer starts to build up from the leading edge along the wedge surface. After the flow separates at the base, it undergoes a mixing process to energize the slowly moving viscous layer to prepare itself for the subsequent recompression process. Specifically, the dividing streamline experiences an increase in velocity within the mixing region before it decreases in the recompression region

and eventually stagnates at the end of the wake. The fluid above the dividing streamline should continue to proceed downstream while the fluid entrained below the dividing streamline is turned back along the course of recompression. Due to the presence of the initial boundary layer at the point of separation and the pressure gradient along the wake region, it is obvious that this mixing process does not exhibit similar behavior; that is, the governing partial differential equations cannot be transformed into ordinary differential equations and meanwhile satisfy the initial and boundary conditions. A detailed analysis on the basis of solving these partial differential equations would be extremely complex. Furthermore, in such an analysis it would be necessary to employ a turbulence model which would adequately describe the turbulent transport processes throughout the entire flow field. Our lack of knowledge of the turbulence structure especially within the recompression region would extremely hamper such an analysis. Chow and Spring [44,45] suggested that these interactive viscous flow effects can be adequately represented by integral properties of flow while keeping the empirical information required to describe the turbulence transport processes at a minimum. It is natural to expect that such an analysis is relatively simplified and yet still retains the essential features of the flow. This is the basic reason that an integral analysis is adopted for the study of the viscous flow.

2.2.1 Initial Boundary Layer

It has been shown by Nash [19] and Tanner [40] that the size of the initial boundary layer at the point of separation has an important effect on the ensuing mixing and recompression processes. It is thus

necessary to examine the development of the boundary layer on the face of the wedge.

It is well known that accelerated flows are considerably more stable than decelerated flows or flows with zero pressure gradient. It should be expected that for any reasonable wedge angle, the boundary layer will be laminar over most of the wedge face. The velocity at any location on the face of the wedge can be found from the inviscid analysis and the development of the laminar boundary layer can be determined by the method of Pohlhausen [47] incorporating the improvements of Holstein and Bohlen [48]. The critical Reynolds number based on the displacement thickness at which transition occurs is given by Schlichting [43] as a function of the pressure gradient on the surface. After the flow changes into turbulent flow, the method of Truckenbrodt [49] is employed to determine the turbulent boundary layer development. To perform these calculations, it is necessary to choose a Reynolds number, Re_H ($Re_H = (U_\infty H)/\nu$ where H is the step height). Since Re_H has a strong influence on the boundary layer development, this is equivalent to choosing the initial boundary layer thickness at the point of separation.

For large wedge angles, the boundary layer over the entire face of the wedge will be laminar. Since turbulent viscous processes usually occur in the mixing region, it is important to clarify the effect of the initial laminar boundary layer on the flow. Chapman, et al. [15] have shown that if transition occurs near the separation point, there is a minimal influence on the flow field. Using their criterion ($Re_t \equiv 3 \times 10^5$), transition for most of the present calculations occurs less than one step height downstream of separation. Therefore, for large wedge angles, the entire wake flow is considered to be turbulent and it is expected that this

simplification would not introduce any serious error. The thickness of the boundary layer at the separation point is determined in this manner and is used as the initial condition for the turbulent mixing analysis.

2.2.2 Quasi-constant Pressure Turbulent Jet Mixing Region

After the flow separates at the base, a free turbulent jet mixing process occurs. Since the mixing region has finite thickness, it is obvious that the guiding inviscid flow of this mixing process would not have a constant velocity so that the process would not be under a truly constant pressure condition. Brink and Chow [50] have shown that a locally similar mixing process can adequately describe the non-similar mixing flow in the presence of a pressure gradient. Therefore, it is assumed that this process can be described by a quasi-constant pressure turbulent jet mixing, namely, the velocity profile at any section can be derived from a constant pressure mixing analysis starting from the same origin with the same initial profile.

The initial boundary layer at the point of separation is assumed to be given by the $1/n$ power law profile ($n = 7$) expressed as

$$\phi = \zeta_1^{1/n} \quad (2.17)$$

where $\zeta_1 = y_1/\delta_1$, $\phi = U/U_a$, δ_1 is the thickness of the initial boundary layer and U_a is the velocity at the edge of the boundary layer.

Since the turbulence level within the wall boundary layer is usually much less than that within a free turbulent jet mixing flow, it is expected that the major mixing activities will occur along the dividing streamline while the condition within the upper part of the initial viscous layer is essentially unchanged until the mixing effect reaches there.

The analysis for the mixing region is, therefore, divided into two parts. Initially, there is a region where the effect of the mixing has not reached the upper edge of the original viscous layer and farther downstream the effect of the mixing has spread throughout the original layer. Denoting y_m as the upper edge of the new mixing layer with respect to the inviscid flow boundary, these regions are identified as $\zeta_m = y_m/\delta_1 < 1$ and $\zeta_m > 1$, respectively. For simplicity, a linear velocity profile is selected for the mixing region and a diagrammatic sketch of the mixing process is illustrated in Fig. 2.4.

Application of the continuity principle to the region where $\zeta_m \leq 1$ yields

$$\phi_d = \frac{U_d}{U_a} = \phi_m \sqrt{1 - \left(\frac{2n}{n+1}\right) \left(\frac{\delta_1}{\delta_a + \delta_b}\right) \zeta_m} \quad (2.18)$$

where δ_a is the thickness of the viscous layer above the dividing streamline, δ_b is the thickness of the viscous layer below the dividing streamline, and $\phi_m = U_m/U_a$. The momentum principle for the same region yields

$$\left(\frac{\delta_1}{\delta_a + \delta_b}\right) \zeta_m = \frac{n+2}{3n} \quad (2.19)$$

Combining the foregoing two equations, it is found that

$$\phi_d = \zeta_m^{1/n} \sqrt{1 - \frac{2}{3} \frac{n+2}{n+1}} \quad (2.20)$$

$$\frac{\delta_a}{\delta_b} = \frac{1}{\sqrt{1 - \frac{2}{3} \frac{n+2}{n+1}}} - 1 = \frac{\zeta_m^{1/n}}{\phi_d} - 1 \quad (2.21)$$

and

$$\frac{\delta_b}{\delta_1} = \phi_d \zeta_m^{1-(1/n)} \left(\frac{3n}{n+2}\right) \quad (2.22)$$

For $\zeta_m \geq 1$, continuity and momentum principles yield, respectively,

$$\phi_d = \sqrt{1 - \left(\frac{\delta_1}{\delta_a + \delta_b} \right)^2 \left(\zeta_m - \frac{1}{n+1} \right)} \quad (2.23)$$

and

$$\frac{\delta_1}{\delta_a + \delta_b} = \frac{1}{3 \left(\zeta_m - \frac{2}{n+2} \right)} \quad (2.24)$$

Combining these two equations, it is found that

$$\phi_d = \sqrt{1 - \frac{2}{3} \frac{\zeta_m - \frac{1}{n+1}}{\zeta_m - \frac{2}{n+2}}} \quad (2.25)$$

and

$$\frac{\delta_a}{\delta_b} = \frac{1}{\phi_d} = 1 \quad (2.26)$$

To relate the downstream location with the particular value of ζ_m and the corresponding velocity profile, it is stipulated that the slope of the linear profile is essentially the same as the maximum slope of the error function profile for a fully developed turbulent jet mixing process, i.e.:

$$\left. \frac{\partial \phi}{\partial \eta} \right|_{\eta=0} = \frac{1}{\pi^{1/2}} \quad (2.27)$$

where $\eta = \sigma(y/x)$ with σ being the similarity parameter for turbulent mixing flows. It should be stressed here that the concept of similarity does not apply to this problem. It is expedient, however, to borrow the spread rate parameter σ for a similar flow to estimate the rate of spread of the present nonsimilar flow problem. Unfortunately, the correct value of σ is still a matter of controversy and it must be obtained from empirical data. Although it has been well accepted that σ is 12 for plane

incompressible flow, recent evidence shows $\sigma = 11$ gives a better correlation with experimental data for fully developed flows. Upon introducing

$$\left. \frac{\partial \phi}{\partial \eta} \right|_{\eta=0} = \frac{x}{\sigma \delta_1} \frac{\partial \phi}{\partial \left(\frac{y}{\delta_1} \right)} = \frac{1}{\sqrt{\pi}}, \quad (2.28)$$

one obtains for $\zeta_m \leq 1$

$$\frac{x}{\delta_1} = \frac{\sigma}{\sqrt{\pi}} \frac{3n}{n+2} \zeta_m^{(n-1)/n} \quad (2.29)$$

and for $\zeta_m \geq 1$,

$$\frac{x}{\delta_1} = \frac{3\sigma}{\sqrt{\pi}} \left[\zeta_m - \frac{2}{n+2} \right]. \quad (2.30)$$

The rate of change of momentum of the fluid below the dividing streamline is due to the shear stress at the dividing streamline and is given by

$$\frac{\tau_d}{\rho} = \frac{d}{dx} \int_{y_d - \delta_b}^{y_d} u^2 dy \quad (2.31)$$

which can be reduced to

$$\frac{\tau_d}{\rho U_a^2} = \frac{1}{3} \frac{d}{dx} [(\delta_a + \delta_b) \phi_d^3]. \quad (2.32)$$

From the given geometry, y_d can also be determined from

$$\frac{y_d}{\delta_1} = \frac{y_m - \delta_a}{\delta_1} = \zeta_m - \frac{\delta_a}{\delta_1} \quad (2.33)$$

and the transverse velocity at the dividing streamline is determined from

$$\frac{dy_d}{dx} = \frac{v_d}{u_d}. \quad (2.34)$$

To evaluate the eddy diffusivity in the mixing region, one may express the shear stress along the dividing streamline as

$$\tau_d = \rho \epsilon \left. \frac{\partial u}{\partial y} \right|_d = \rho \epsilon U_a \frac{\phi_d}{\delta_b} \quad (2.35)$$

and ϵ can be solved for and given by

$$\frac{\epsilon}{U_a \delta_a} = \frac{\tau_d}{\rho U_a^2} \frac{1}{\phi_d} \frac{\delta_b}{\delta_a} \quad (2.36)$$

which can be rearranged into

$$\bar{\epsilon} \frac{U_a}{U_\infty} \frac{H}{\delta_a} = \frac{\tau_d}{\rho U_a^2} \frac{\delta_b}{\delta_a} \frac{1}{\phi_d} \quad (2.37)$$

where $\bar{\epsilon} = \epsilon/U_\infty H$.

2.2.3 Recompression Region

The recompression region as shown in Fig. 2.5 is divided into two subregions. The upper region is the shear layer above the dividing streamline which interacts directly with the external inviscid stream and the lower region is the viscous layer below the dividing streamline which will eventually be turned back to form the reverse wake flow. As pointed out by Chow and Spring [44] and also observed from preliminary investigations of the present effort, the pressure differences across the viscous layer are small and can be neglected. This can also be explained by considering the normal momentum equation for a viscous flow written as

$$\rho \frac{v_s^2}{R_c} = - \frac{\partial p}{\partial n} + \frac{\partial \tau_{sn}}{\partial s} \quad (2.38) *$$

The term $\partial \tau_{sn} / \partial s$ is usually small and can be neglected.* Upon integrating this equation across a viscous layer, one obtains:

*Note that if $\partial \tau_{sn} / \partial s$ were not negligible due to turbulence, there would be no such terminology as "turbulent boundary layer."

$$p_w - p_e = \frac{\rho_e v_e^2 \delta}{R_c} \int_0^\delta \frac{\rho}{\rho_e} \phi^2 d\zeta \quad (2.39)$$

where R_c is a representative radius of curvature of the streamline and the subscript e denotes the state at the upper edge of the viscous layer. The integral is ordinarily of the order of unity and Eq. (2.48) obviously yields

$$\left(\frac{p_w}{p_e} - 1 \right) = O \left(\frac{\gamma M_e^2 \delta}{R_c} \right) \quad (2.40)$$

where O denotes an estimation of the order of magnitude. Thus one can see that if the external Mach number is small or the characteristics radius of curvature is large, the pressure difference across the viscous layer is indeed negligibly small.

2.2.3.1 Upper Layer

For the upper viscous layer, continuity principle stipulates that

$$\frac{\partial u}{\partial x} + \frac{\partial v}{\partial y} = 0 \quad (2.41)$$

Integrating this equation from the dividing streamline to the upper edge of the shear layer as depicted in Fig. 2.5, one obtains

$$v_a - v_d = - \int_{y_d}^T \frac{\partial u}{\partial x} dy \quad (2.42)$$

which can be reduced according to Liebnitz rule to yield

$$v_a - v_d = - \frac{\partial}{\partial x} \int_{y_d}^T u dy + u_a \frac{dT}{dx} - u_d \frac{dy_d}{dx} \quad (2.43)$$

Upon employing the relationship

$$U_d \frac{dy_d}{dx} = v_d \quad (2.44)$$

and defining $\zeta_u = (y - y_d)/\delta_a$, Eq. (2.43) becomes

$$\frac{dT}{dx} - \frac{U_\infty}{U_a} \frac{d}{dx} \left[\frac{U_a}{U_\infty} \delta_a \int_0^1 \phi d\zeta_u \right] = \tan \beta_a \quad (2.45)$$

where $\tan \beta_a = v_a/U_a$.

The momentum principle applied to a differential control volume as shown in Fig. 2.5 would yield

$$\begin{aligned} \frac{d}{dx} \left[\int_{y_d}^T \rho u^2 dy \right] dx - U_a \frac{d}{dx} \left[\int_{y_d}^T \rho u dy \right] dx &= \int_{y_d}^T P_a dy - P_a dy_d \\ &- \left\{ \int_{y_d}^T P_a dy + \frac{d}{dx} \left[\int_{y_d}^T P_a dy \right] dx \right\} + P_a dT - \tau_d dx \end{aligned} \quad (2.46)$$

This can be rearranged and written as

$$\frac{d}{dx} \int_{y_d}^T \rho U(U_a - U) dy - \int_{y_d}^T \rho U dy \frac{dU_a}{dx} + (T - y_d) \frac{dP_a}{dx} = \tau_d \quad (2.47)$$

Upon introducing the relationship for the free stream,

$$\frac{dP_a}{dx} = -\rho U_a \frac{dU_a}{dx} \quad (2.48)$$

and defining $\delta_a = (T - y_d)$, $\phi = U/U_a$, and $\zeta_u = (y - y_d)/\delta_a$, Eq. (2.47)

becomes

$$\frac{d}{dx} \left[\delta_a \left(\frac{U_a}{U_\infty} \right)^2 \int_0^1 \phi(1 - \phi) d\zeta_u \right] + \delta_a \left(\frac{U_a}{U_\infty} \right) \int_0^1 (1 - \phi) d\zeta_u \frac{d}{dx} \left(\frac{U_a}{U_\infty} \right) = \frac{\tau_d}{\rho U_\infty^2} \quad (2.49)$$

To evaluate the integrals in Eqs. (2.45) and (2.44), a third-order polynomial velocity profile of the form

$$\phi = A + B\zeta_u + C\zeta_u^2 + D\zeta_u^3 \quad (2.50)$$

is assumed for this upper layer. The boundary conditions required to evaluate the constants are

at $\zeta_u = 0$:

$$\phi = \phi_d \text{ and } \frac{\partial\phi}{\partial\zeta_u} = s; \quad (2.51)$$

at $\zeta_u = 1$:

$$\phi = 1 \text{ and } \frac{\partial\phi}{\partial\zeta_u} = 0$$

where $s = (\partial\phi/\partial\zeta)|_d$. Equation (2.50) is thus reduced into

$$\phi = \phi_d + s\zeta_u + [3(1 - \phi_d) - 2s]\zeta_u^2 + [s - 2(1 - \phi_d)]\zeta_u^3 \quad (2.52)$$

To assure that both ϕ_d and s vanish at the point of reattachment, it is assumed [33,45] that

$$s = g\phi_d \quad (2.53)$$

where g is a proportionality constant to be determined from the condition at the end of the mixing region.

2.2.3.2 Wake Flow Region

The wake flow region as shown in Fig. 2.5 consists of a forward flow below the dividing streamline and a backward flow above the lower wall (splitter plate). For simplicity, the forward flow assumes a linear velocity profile given by

$$\phi = \frac{U}{U_a} = \phi_d \zeta_\ell \quad (2.54)$$

where $\zeta_\ell = (y - h_b)/\delta_b$ and the reverse flow assumes a cosine velocity profile given by

$$\phi = \frac{U}{U_a} = -\phi_b \cos\left(\frac{\pi}{2} \zeta_b\right) \quad (2.55)$$

where $\zeta_b = y/h_b$.

The principle of conservation of mass below the dividing streamline requires that

$$\int_{h_b}^{\delta_b + h_b} \rho u \, dy = \int_0^{h_b} \rho u \, dy \quad (2.56)$$

By employing the assumed profiles, Eq. (2.56) can be integrated and simplified to yield

$$\frac{U_b}{U_d} = \frac{\phi_b}{\phi_d} = \frac{\pi}{4} \frac{\delta_b}{h_b} \quad (2.57)$$

The momentum principle for this region requires that

$$\frac{d}{dx} \left[\int_0^{h_b} \rho u^2 \, dy \right] + \frac{d}{dx} \left[\int_{h_b}^{\delta_b + h_b} \rho u^2 \, dy \right] = y_d \frac{d P_a}{dx} + \tau_d. \quad (2.58)$$

Upon inserting the appropriate velocity profiles and utilizing Eq. (2.48) Eq. (2.58) is reduced to

$$\frac{d}{dx} \left[\left(\frac{U_a}{U_\infty} \right)^2 \left\{ \frac{\delta_b^2 \phi_d^2}{3} + \frac{h_b^2 \phi_b^2}{2} \right\} \right] - y_d \left(\frac{U_a}{U_\infty} \right) \frac{d(U_a/U_\infty)}{dx} = \frac{\tau_d}{\rho U_\infty^2}. \quad (2.59)$$

It should be mentioned that this analysis is valid only for steady flows (i.e., no vortex shedding) and this would require a lower wall or a splitter plate inserted behind the wedge. Obviously, this would give rise to a reverse flow boundary layer which is not accounted for by the cosine profile. However, if it is assumed that a cosine profile can also describe the reverse wall boundary layer, the mass and momentum flux integrals of the reverse flow with boundary layer would produce the same

results as Eqs. (2.55) and (2.59) as long as h_b and ϕ_b have the same meaning as the present case. The remaining difference is the small wall shear stress which is usually neglected.

Although the slope of the velocity profile will not be continuous at the dividing streamline and at the centerline of the wake, local smoothing techniques may be used to improve this situation. This, however, should not significantly affect the mass and momentum flux.

2.2.3.3 Computational Form of the Equations

Equations (2.45), (2.49), (2.57), and (2.59) can be rewritten, respectively, as

$$\frac{dT}{dx} - \frac{U_\infty}{U_a} \frac{d}{dx} \left[\delta_a \frac{U_a}{U_\infty} F_1 \right] = \tan \beta_a \quad (2.60)$$

$$\frac{d}{dx} \left[\left(\frac{U_a}{U_\infty} \right)^2 \delta_a F_2 \right] + \delta_a (1 - F_1) \left(\frac{U_a}{U_\infty} \right) \frac{d(U_a/U_\infty)}{dx} = \frac{\tau_d}{\rho U_\infty^2} \quad (2.61)$$

$$\phi_b = \frac{\pi}{4} \frac{\delta_b}{h_b} \phi_d \quad (2.62)$$

and

$$\frac{d}{dx} \left[\left(\frac{U_a}{U_\infty} \right) \left(\frac{\delta_b \phi_d^2}{3} + \frac{h_b \phi_b^2}{2} \right) - y_d \left(\frac{U_a}{U_\infty} \right) \frac{d(U_a/U_\infty)}{dx} \right] = \frac{\tau_d}{\rho U_\infty^2} \quad (2.63)$$

Where F_1 and F_2 represent the integrals

$$F_1 = \int_0^1 \phi \, d \zeta_u \quad \text{and} \quad F_2 = \int_0^1 \phi(1 - \phi) \, d \zeta_u \quad (2.64)$$

which can be expressed explicitly as

$$F_1 = \frac{1}{2} - \frac{\phi_d}{2} + \frac{s}{12} \quad (2.65a)$$

and

$$F_2 = \frac{9}{70} + \frac{17}{70} \phi_d + \frac{3s}{140} - \frac{13 \phi_d^2}{35} - \frac{11}{105} s \phi_d - \frac{1}{105} s^2. \quad (2.65b)$$

Very little information is available about the turbulence structure in the recompression wake region and, in particular, the shear stress at the dividing streamline given by

$$\frac{\tau_d}{\rho U_\infty^2} = \frac{U_a}{U_\infty} \frac{\bar{\epsilon}}{\delta_a} \frac{H}{s} \quad (2.66)$$

cannot be confidently estimated. As suggested by Chow and Spring [44,45], an eddy diffusivity model is adopted for this problem and $\bar{\epsilon}$ is related to its value at the end of the mixing region through

$$\frac{\bar{\epsilon}}{\bar{\epsilon}_m} = \frac{U_a}{U_{a_m}} \left(\frac{\delta_a}{\delta_{a_m}} \right)^2 \left(\frac{\ell_m + x_r}{\ell_m} \right) \quad (2.67)$$

where the subscript m refers to the section of the end of the quasi-constant pressure jet mixing region, ℓ_m is the length of this mixing region, and x_r is the length along the recompression flow process.

One final relation is needed before the system of equations can be integrated. A locally triangular geometry shown in Fig. 2.6 is assumed so that extension of the dividing streamline and the line at zero velocity intersect at the same point on the wall. This condition assures the fact that the reverse flow height vanishes at the point of reattachment and is expressed as

$$\frac{dh_b}{dx} = \frac{dy_d}{dx} \frac{h_b}{y_d} \quad (2.68)$$

Equations (2.60), (2.61), and (2.63) can now be manipulated and rewritten as

$$(1 - F_1) \frac{dT}{dx} - (T - y_d) \frac{dF_1}{d\phi_d} \frac{d\phi_d}{dx} + F_1 \frac{dy_d}{dx} = \tan \beta_a + F_1 (T - y_d) \cdot \left(\frac{U_\infty}{U_a} \right) \frac{d(U_a/U_\infty)}{dx} \quad (2.69)$$

$$F_2 \frac{dT}{dx} + (T - y_d) \frac{dF_2}{d\phi_d} \frac{d\phi_d}{dx} - F_2 \frac{dy_d}{dx} = \bar{\epsilon} \left(\frac{U_\infty}{U_a} \right) \left(\frac{H}{\delta_a} \right) s - \left(\frac{U_\infty}{U_a} \right) \cdot \frac{d(U_a/U_\infty)}{dx} (T - y_d) (2F_2 + 1 - F_1) \quad (2.70)$$

and

$$\left(2 \frac{\phi_d^2 \delta_b}{3} + h_b \phi_b^2 \right) \frac{d\phi_d}{dx} + \phi_d \left(\frac{\delta_b}{y_d} \frac{\phi_d^2}{3} + \frac{h_b}{y_d} \frac{\phi_b^2}{2} \right) \frac{dy_d}{dx} = \phi_d \left[\bar{\epsilon} \left(\frac{U_\infty}{U_a} \right) \left(\frac{H}{\delta_a} \right) s + \left(\frac{U_\infty}{U_a} \right) \frac{d(U_a/U_\infty)}{dx} (y_d - \frac{2}{3} \delta_b \phi_d^2 - h_b \phi_b^2) \right]. \quad (2.71)$$

With the initial conditions provided from the preceeding mixing analysis, numerical integration of Eqs. (2.68), (2.69), (2.70), and (2.71) along with Eq. (2.62) establishes the appropriate values of T , y_d , ϕ_d , ϕ_b , δ_b , and h_b . The inviscid flow condition at the edge of the viscous layer is obtained from the corresponding inviscid flow field and depends upon the location of the edge of the viscous layer. It is, nevertheless, found that the term $(U_\infty/U_a) d(U_a/U_\infty)/dx$ is a slowly varying function. It is thus convenient to leave this term at the right-hand side of the system of equations as a quantity to be evaluated from the previous step of integration so that iteration can be avoided. Furthermore, all the differential equations and algebraic relations are homogeneous in length so that all length quantities can be considered to be already normalized by the step height H .

2.3 METHOD OF CALCULATION

Calculations begin with the selection of a pair of values, α and k_1 , and the corresponding inviscid flow field can be established. Of immediate importance is the arc length of the mixing region and the location of point D in the physical plane. The development of the boundary layer on the face of the wedge is calculated by employing the velocity along the bounding streamline as determined from the inviscid flow. A Reynolds number corresponding to the approaching flow condition must be determined in order to calculate the boundary layer thickness at the point of separation. The flow properties ϕ_d , δ_a/H , δ_b/H , $\tau_d/\rho U_\infty^2$, $\bar{\epsilon}_m$, and y_d at the end of the mixing region are determined from the quasi-constant pressure jet mixing analysis. These quantities provide the initial conditions for the recompression analysis.

To proceed with the numerical integration of the system of equations for the recompression region, it is necessary to locate the outer edge of the viscous layer at the initial step of recompression. The x,y coordinates of point F as shown in Fig. 2.7 are given by

$$\begin{aligned}x_F &= x_D + (\delta_a + y_d) \sin \alpha \\x_F &= y_D + (\delta_a + y_d) \cos \alpha\end{aligned}\tag{2.72}$$

where x_D and y_D are determined from the corresponding inviscid flow and δ_a and y_d are determined from the mixing analysis. The location of point F in the t-plane is found by numerical integration of Eq. (2.11) and the velocity and flow direction at F can be determined from Eq. (2.8). Numerical step-by-step integration of Eqs. (2.69), (2.70), and (2.71) can now be carried out with the guiding inviscid stream determined in the similar manner.

As noted by Chow and Spring [44], the point of reattachment exhibits a "saddle point-type" singularity; that is, as the point of reattachment is

approached, slight variations in values of k_1 result in widely different values of ϕ_D . Figure 2.8 shows this behavior for a typical set of calculations where the dimensionless dividing streamline velocity ϕ_d is plotted against the step of integration with k_1 as a parameter. For a fixed value of α , it is observed that for smaller values of k_1 , ϕ_d is reduced drastically and will reach zero or negative numerical values (with fixed step length of integration Δx) before the lower wall is reached. For slightly larger values of k_1 , the value of ϕ_d will eventually increase. These patterns are not physically realistic and additional calculations should be carried out with intermediate k_1 values so that the condition of zero dividing streamline velocity can, hopefully, be reached on the lower wall. In practice, an effective means must be implemented so that the correct pair of values of α and k_1 can be determined. For a certain value of α , once the k_1 value has been established up to, e.g., the eighth digit after the decimal point, the point of reattachment, as well as the corresponding free stream flow conditions are established from extrapolation. For this set of values of α and k_1 , an unbalanced residue may be evaluated from Eq. (2.70) at the point of reattachment. The correct values of k_1 and α for the problem are such that this residue vanishes. It is the experience of this study that this scheme produces consistent and smooth residue curves as shown in Fig. 2.9.

3. RESULTS AND DISCUSSION OF THEORETICAL CALCULATIONS

Upon employing the method described in previous sections, calculations have been performed with a Reynolds number ($Re_H = V_\infty H/\nu$) of 5×10^4 and a well accepted value of 12 for α , the spread rate parameter in the mixing region. The established values of α , k_1 and k_2 , and the corresponding base pressure coefficient for various wedge angles are shown in Fig. 3.1. It should be noted that the established values of α and k_2 are nearly independent of the wedge angle. Since the free streamline region (from B to C) always spans the range from -1 to +1 in the t plane, this evidence of slight dependency upon the wedge angle suggests a certain affinity between the length and angle of recompression and the free streamline region in these corresponding inviscid flow fields. The value of k_1 , however, varies from 0.96 for $\theta = 90$ degrees to 0.032 for $\theta = 1$ degree. As θ approaches 0, k_1 also approaches 0 and the limiting case is a rearward facing step where the front stagnation point would be located at $-\infty$. Previous results [45] ($\alpha = 7.88$, $k_2 = 0.23$) obtained for this flow case with a different Reynolds number are also included for the purpose of comparison. It is probable that accurate calculations cannot be maintained with the existing computer program as the wedge angle is reduced.

Pressure distributions on the lower wall (splitter plate) within the wake region for different wedge angles are shown in Fig. 3.2. With the exception of small wedge angles, the pressure at the point of reattachment has not overshoot that of the freestream flow. The pressure upstream of the recompression region is obtained directly from the quasi-constant pressure mixing process.

With $\sigma = 12$, the effect of the initial boundary layer momentum thickness (δ^{**}/H) is illustrated in Fig. 3.3 for a 30-degree wedge angle from calculations for two different momentum thicknesses. It appears that the initial δ^{**}/H has a strong influence on the base pressure. To demonstrate this effect, Fig. 3.4 shows the variation of c_{pb} with respect to the initial momentum thickness.

It can be seen that as δ^{**}/H increases, the base pressure coefficient also increases; for small δ^{**}/H (< 0.003), however, this effect is negligible. These trends have two important implications: First, a δ^{**}/H of 0.005 corresponds to a Reynolds number of 10^4 and a larger δ^{**}/H (smaller Re_H) would be characterized by laminar flow over a large portion of the wake. Since this study is not designed to analyze laminar mixing and recompression processes, the section of the curve corresponding to large δ^{**}/H is only included to demonstrate the results that would be obtained if the initial boundary layer were manipulated (e.g., tripped) in order to study the effect of large initial boundary layer on the turbulent mixing and recompression processes. Secondly, for δ^{**}/H smaller than 0.003 ($Re_H > 2 \times 10^4$), the flow would definitely be turbulent over most of the wake region. In this regime, however, c_{pb} is nearly independent of δ^{**}/H (or Re_H). These effects agree quite well with Tanner's [40] experimental results, i.e., for turbulent flow processes, the base pressure is nearly independent of Reynolds number but increases somewhat with increasing boundary layer thickness.

The parameter having a relatively strong influence on the results of the calculations is the turbulent mixing spread rate parameter σ . In the strict sense, σ is a similarity parameter for plane mixing flows which is inversely proportional to the rate of spread of the mixing layer. Since

some empirical information is always necessary for turbulent flow calculations, the idea of a spread rate parameter is introduced for the mixing analysis even though the actual flow is nonsimilar. Although the value of σ has not been accurately established for similar two-dimensional incompressible turbulent mixing flows, it should not be far away from 12. In order to assess its influence to the results of the calculations, different values of σ have been employed. Figure 3.5 shows the results of calculations for a 30-degree wedge angle at $Re_H = 5 \times 10^4$ for three values of σ . It can be seen that σ has a relatively strong influence on the flow of the entire wake region. If σ is decreased, the base pressure is lowered and the recompression is strengthened.

Although $\sigma = 12$ seems to be an appropriate value for mixing between a uniform stream and a quiescent fluid, Tanner [42] suggested that for flow over wedges, the angle between the wall from which the flow separates and the wall upon which the flow reattaches has a strong influence on σ . Based on experimental data, Tanner estimated the dependency of σ on the wedge angle. Figure 3.6, which compares c_{pb} of the present investigation with Tanner's experimental data and one data point from Arie and Rouse's study [51], is useful in determining the dependency of σ on the wedge angle for the present analysis. Assuming that Tanner's data is correct, the results for $\sigma = 12$ for large θ are much too high. Since Tanner indicated that σ is a function of θ , an effort was made to determine the value of σ such that the present calculations agree with Tanner's results. Figures 3.7 and 3.8 illustrate the dependence of c_{pb} upon σ for two different wedge angles and the means by which the "adjusted" value of σ was determined. These results and the results of similar calculations for other wedge angles

are also shown in Fig. 3.6. It can be seen in Figs. 3.7 and 3.8 that the results are much more dependent upon σ for large wedge angles than is the case for small θ . Also, the larger the value of σ , the less dependent the calculations are for a particular wedge angle. This indicates that for very small θ , any value of σ from 12 to 15 would probably be adequate while for large θ , the precise value of σ is very important.

Figure 3.9 shows the value of σ that is necessary to obtain agreement with Tanner's experimental data. σ varies from about 9.3 for a flat plate normal to the flow to 14 for a 5-degree wedge. It should be mentioned that the values of σ for the present results and Tanner's data should not be expected to agree. σ in the present analysis is a parameter that is employed to estimate an average spread rate for the mixing analysis; the manner in which it is utilized, or the exact meaning attached to it, may be different for each individual investigation. What is significant is that the trends of each set of results are the same, i.e., σ decreases with increasing wedge angle.

In order to evaluate the results of this analysis, it is, of course, necessary to compare them with experimental results. The only available detailed results of separated flows past wedges are provided by Tanner [38]. There is some question, however, about the validity of Tanner's experimental data because of the problem of wind tunnel wall interference. For Tanner's experiments, Table 3.1 shows the ratio R/H for various wedge angle θ where R is the wind tunnel height and H is the wedge step height. It is expected that the effect of wind tunnel interference for a particular θ depends entirely on this ratio and only for $R/H \gg 1$ will the interference be negligible. For large θ , however, Tanner's R/H ratios are relatively small and it is important to investigate this effect on c_{pb} and the wake region in general.

Table 3.1

θ , degrees	R/H
7.5	115
15	55.8
30	30
45	27.2
60	17.4
90	No Information

To evaluate this effect, a second theoretical analysis was performed that was exactly the same as the one given in Chapter 2 except that the corresponding inviscid flow was modified to account for the existence of a top wall at an arbitrary distance from the model. The detailed analysis of this flow is given in APPENDIX A. Figure 3.10 shows the results of these calculations for a 30-degree wedge angle with $\sigma = 12$ and $Re_H = 5 \times 10^4$. It illustrates the manner in which c_{pb} is affected as R/H is decreased and its comparison with the value of c_{pb} for an infinite R/H. For R/H less than 50, the base pressure is significantly lowered and for R/H less than about 15, the effect becomes overwhelming. This phenomenon, however, is certainly not out of expectation. For a wedge in an infinite stream, streamlines are somewhat relieved across the normal direction. If a top wall is present, streamlines are compressed and the flow must be greatly accelerated. It should also be expected that this effect is greater for large θ . The graph shown in Fig. 3.11 is the same as that shown in Fig. 3.6 except that it shows additional results of calculations which correspond to R/H = 20 with $\sigma = 12$. Although values of R/H do not match Tanner's testing conditions, it appears

that wind tunnel effects would account mostly for the discrepancies in the results. This wall interference analysis, however, only considers the effect on the corresponding inviscid flow. Since the interference phenomenon is probably much more complex, these results are offered only as qualitative examples. Clearly what is needed is a thorough experimental investigation of wall interference effects in order to assess the dependence of this analysis (and other theoretical analyses) on R/H and σ .

Figures 3.12 through 3.17 show the pressure distributions on the surface of the wedge for various θ at $Re = 5 \times 10^4$ using the "adjusted" σ values. Excellent agreement with Tanner's data [38] has been observed in Figs. 3.13, 3.15, and 3.16 where the experimental data are available. By integrating this pressure distribution over the wedge surface, the drag coefficient can be obtained and is shown in Fig. 3.18 as a function of wedge angle. Also included is a data point from Arie and Rouse's experimental investigation [51] for $\theta = 90$ degrees. It is expected that the c_D results are quite good since both the base pressure and the pressure distributions on the surface of the wedge agree with Tanner's experimental data [38].

It is appropriate to point out that since the governing inviscid flow obeys the Laplace equation, any reasonable inviscid free streamline flow analysis incorporating the experimentally observed base pressure in the wake would lead to theoretical results of surface pressure and drag characteristics which should be in excellent agreement with experimental data. This is indeed the case reported in many existing inviscid flow analyses where the wake is not closed and extends indefinitely far downstream. The

present analysis has fully illustrated the fact that while the important role played by the viscous flow mechanisms is fully appreciated, determination of the base pressure is the most important part of the problem.

Figures 3.19 through 3.23 present pressure distributions along the wall (splitter plate) for various wedge angles using the adjusted value of σ . Figures 3.19 through 3.22 are compared with Tanner's experimental data [38]. For large wedge angles, the theoretical results are in excellent agreement with experimental data. For small wedge angles, recompression is not as strong as the experimental data has shown. Again, the experimental data has been modified by the effect of tunnel wall interference, and the phenomenon of recompression reattachment is exemplified by these calculations.

Figure 3.24 presents a comparison between the pressure distributions for a 1-degree wedge angle ($\sigma = 12$ and $Re_H = 5 \times 10^4$) and Chow and Spring's results [45] for a backstep.

It is impossible to perform the calculations for a wedge of smaller angle with the existing computer program because transformations of the corresponding inviscid analysis blow up as θ approaches 0. Initial boundary layers for both cases are nearly identical and it is expected that if θ could be reduced further, the pressure distribution would converge toward Chow and Spring's results [45]. As can be seen from Fig. 3.2, the largest changes in the pressure distributions as a function of θ occur at small angles.

The dividing streamline and maximum reverse flow velocities are shown in Figs. 3.25 thru 3.29 for various wedge angles. The dimensionless velocity of the dividing streamline, ϕ_d , increases in the mixing region as the slowly moving wake flow is energized and decreases in the recompression region,

eventually stagnating at the reattachment point. For large wedge angles, the flow is quickly energized and ϕ_d attains a nearly constant velocity throughout most of the mixing region. It is interesting to note that for large wedge angles, ϕ_d essentially attains the value (0.5774) of a fully developed flow. Since the initial boundary layer⁺ is thin and the mixing region is very long, a locally similar mixing analysis would be adequate for large θ and high Re_H . It should also be mentioned that the discontinuities in the rate of change of ϕ_d and ϕ_b exhibited within these figures are inherent results of component analyses as two different component regions are joined together.

Figure 3.30 presents the geometry of the wake region for a 30-degree wedge angle at $\sigma = 12$ and $Re_H = 5 \times 10^4$, and Fig. 3.31 shows a comparison between the wake configurations for five different wedge angles at $Re_H = 5 \times 10^4$ using the "adjusted" σ values. As expected, large wedge angles have thicker and longer wake regions; the maximum occurs for $\theta = 90$ degrees with a thickness of about $3H$ and a length of about $17H$. Figure 3.32 compares the wake configurations of a 1-degree wedge and a backstep. Calculations for small θ again approach the results given by Chow and Spring [45] for a backstep.

Figure 3.33 shows the turbulent shear stress along the dividing streamline for various wedge angles. It is interesting to note that the maximum shear stress, which occurs at the beginning of the recompression region, is in good agreement with the maximum shear stress measured experimentally as reported by Bradshaw and Wong [51]. The maximum shear stress varies from $0.0105 \rho U_\infty^2$ for a 5-degree wedge to $0.0188 \rho U_\infty^2$ for a flat plate normal to the flow. Arie and Rouse [52] obtained a maximum shear stress of about $0.02 \rho U_\infty^2$ for a normal flat plate and Bradshaw and

Wong [51] reviewed a number of investigations for a backstep in which values ranging from about $0.012 \rho U_\infty^2$ to $0.016 \rho U_\infty^2$ were obtained.

The shear stress along the dividing streamline is calculated through estimations of the eddy diffusivity. Very little is known about the turbulence structure within the wake region, and the validity of the adopted model for the eddy diffusivity can only be established by comparison of results with experimental data. Although the eddy diffusivity model appears to be adequate for this analysis, the poor agreement of pressure distributions for small wedge angle may be due in part to the adopted model.

An interesting result of these calculations is that once a solution for a particular wedge angle has been determined, the corresponding inviscid analysis can be used to determine the constant c_1 of an inviscid flow near the front stagnation point of a wedge with a velocity given by

$$u = c_1 x^m \quad (3.1)$$

for the Faulkner-Skan flow. The analysis necessary to determine c_1 and results of c_1 as a function of θ are given in APPENDIX B.

An analysis of separated incompressible turbulent flow past wedges, however, will not be complete until the problem of the redevelopment of the flow after reattachment is solved. As one may imagine, this region is occupied by a flow with non-equilibrium turbulent structure and an accurate analysis of the flow is not yet available. Additional recompression usually occurs before the pressure drops asymptotically toward the free stream value. The turbulent wall shear stress builds up sharply while the maximum intensity of turbulence within the viscous layer is reduced. Conceivably, a new wall shear layer starts to build up at the point of

reattachment. No turbulent boundary layer model in existence today is capable of handling these problems.

To obtain some idea of the flow redevelopment, a streamline is traced through the region starting at the outer edge of the viscous layer at the point of reattachment. Figure 3.34 shows the pressure distribution obtained for a 30-degree wedge. With the established corresponding inviscid flow field, this tracing is achieved by integrating

$$\frac{dT}{dx} = \tan \beta_a \quad (3.2)$$

toward the downstream direction. The pressure distribution overshoots that of the freestream value and then decreases afterwards asymptotically toward the latter. This simple calculation qualitatively illustrates the behavior of pressure after reattachment. All effort, however, to construct a detailed model to study flow redevelopment has been hampered by the extremely complex nature of the flow in this region.

It should be pointed out that assumptions have been employed in the establishment of the inviscid free streamline flow and the restriction of a straight line path of recompression has been imposed simply for the benefit of deriving a solution through conformal mapping. It is obvious that with the established flow field reported thus far, the corresponding inviscid flow boundary (bounding streamline) is not truly given by the originally assumed configuration which corresponds to the case of infinite Reynolds number. The bounding streamline for the case of finite Reynolds number should assume a profile which is shifted from the viscous dividing streamline toward the freestream by approximately an amount of the "displacement thickness" of the shear layer above the dividing streamline. The results reported here are thus the first approximation to the finite Reynolds number problem. Additional improvement to account for the effect

of finite Reynolds number is possible by employing other techniques (e.g., surface source-sink method) in generating the corrected corresponding inviscid flow field. Since the effect of Reynolds number within the high Reynolds number regime is small, this method of successive approximations is expected to be rapidly convergent. Moreover, the present scheme of first approximation should yield close prediction of, e.g. the base pressure coefficient.

Finally, it should be mentioned that under assumptions adopted for the steady viscous flow process of recompression, the point of reattachment exhibits itself as a saddle point singularity for the system of equations governing the flow and this special characteristic has been exploited to good advantage. Although the physical process does not seem to show any sensitive characteristics, as associated with a saddle point, the validity of this mathematical behavior should be judged only by the merits in its ultimate results when compared with experimental data. It is well known that as long as one adopts the Navier-Stokes equation to describe the viscous fluid motion and meanwhile demanding continuous solutions to this equation, saddle point singularity or singularity of other types can inherently exist.

4. EXPERIMENTAL INVESTIGATION

As previously discussed, the extremely complex nature of the redeveloping flow hampered the development of a theoretical analysis for this region. It is imperative that further experimental investigations be undertaken to sort out the various processes and mechanisms prevailing within this region. Arie and Rouse [52], Tani, et al. [53], and Mueller and Robertson [54] provided some data for the separated flow region, and Bradshaw and Wong [51] presented a good discussion of the problem associated with flow redevelopment and included some of their experimental data.

Although Bradshaw and Wong suggested that the redeveloping boundary layer is of non-equilibrium nature for at least 300 step heights downstream of separation, the region of critical importance is that immediately downstream of reattachment where the flow is undergoing further recompression and the wall shear stress coefficient c_f is increasing rapidly. It is obvious that the events occurring in this region are strongly influenced by the preceding wake flow and any experimental investigation should consider the ongoing process of the entire region. For this reason, the region under investigation extends from the point of separation to 20 step heights downstream of a backward facing step.

4.1 APPARATUS AND INSTRUMENTATION

4.1.1 Wind Tunnel Facility

The wind tunnel facility shown schematically in Fig. 4.1 is of the induced draft type. A General Electric Corporation, 30 hp, dc motor drives a centrifugal fan. The motor is controlled by a General Electric Corporation rheostat. Ambient air is drawn into the test section through a 27:1 contraction inlet that contains a series of screens

and filters and a splitter plate to condition the flow. The resulting velocity profile at the entrance of the test section is uniform and parallel with a maximum relative turbulence intensity of 0.02 percent outside the boundary layer on the splitter plate.

4.1.2 Test Section

Measurements are obtained in the 15-inch by 15-inch test section shown in Fig. 4.2. It is 60 inches long and the walls are made of 3/8-inch Plexiglas. A 3/8-inch aluminum plate, 48 inches in length, is inserted two inches below the centerline, and a 6-inch by 2-inch rectangular aluminum step is positioned on top the plate and joined smoothly to the upstream splitter plate. All joints are sealed with a silicone sealant which is sufficient since the pressures above and below the dividing plate are not too different. There are 21 step heights of working section downstream of the step and three step heights upstream. Since reattachment occurs about six step heights downstream of the step for problems of this type, this leaves about 15 step heights for measurements in the redevelopment region. The top wall of the test section has a 1-inch slot cut along the centerline for axial positioning of the probe traversing mechanism. Brass runners on either side of the slot allow the mechanism to traverse the entire length of the test section. Removable plugs are used to fill the slot at positions not in use. The traversing mechanism provides positioning over the entire vertical section accurate to about 0.01 inch. Pipe threaded ports on the side wall allow for pitot-static probe positioning at several locations.

4.1.3 Hot Wire Anemometry

Two different hot wires were employed for the present investigation. A Thermo-Systems, Inc. (TSI), 1218-T1.5, single-wire boundary layer probe was employed to determine mean velocity profiles in regions where the normal component of velocity is negligible. As shown in Fig. 4.3a, the probe body has a spike so that the sensor can be positioned accurately 0.005 inch above the wall. A 0.00015-inch diameter tungsten wire is stretched across two gold plated support pins spaced 0.06 inch apart with a sensing length of 0.05 inch for an aspect ratio of over 300.

A TSI 1243-T1.5 boundary layer x-probe, shown in Fig. 4.3b, was used for all turbulence $((\overline{u'^2})^{1/2}, (\overline{v'^2})^{1/2}, \overline{u'v'})$ measurements and for mean velocity $(\overline{U}, \overline{V})$ measurements in and around the wake region. It also has 0.00015-inch diameter tungsten wires attached to gold plated support pins. The two wires, each 0.06 inch in length, are positioned at right angles to each other and 0.04 inch apart.

Two DISA-type 55A01 anemometer units employed in the constant temperature mode were used for this study. The anemometer outputs were linearized for all data, and this operation was performed by two DISA-type 55D15 linearizers. A TSI Model 1015C correlator was used to obtain the sum and difference of the two x-wire signals after linearization as well as the $\overline{u'v'}$ correlation. Mean voltage outputs were measured with a Nonlinear Systems Series X-3, Model A digital voltmeter, and fluctuating voltage outputs were measured with a Hewlett-Packard H12-3400A rms voltmeter.

4.2 CALIBRATION

The hot wires were calibrated essentially by employing the linearizers. It is known that the relation between the voltage output of the anemometer bridge and the velocity impinging on the hot-wire probe can be expressed as $E^2 = E_0^2 + B(U)^n$ where E denotes the anemometer bridge output; E_0 , the same output at zero velocity; U , velocity normal to the probe; and B and n are constants. Since the transfer function employed in the linearizer is $E_{out} = K(E^2 - E_0^2)^m$, where K is the gain and the value of m for the hot wires operating in the range of 20 ft/s to 500 ft/s is 3, the velocity is linearized so that $U = K_0 E_{out}$ where K_0 is a constant gain that is adjusted so that the linearizer output is full scale at the maximum velocity encountered in order to obtain maximum resolution.

The hot wires are calibrated inside the wind tunnel, either upstream of the step or far downstream after reattachment, midway between the lower and upper walls where the velocity profile is uniform and parallel. The velocity at either of these locations is determined by a pitot-static probe. The calibration (linearization) is obtained by proper manipulation of the linearizer at two points: $U = 0$ and $U = U_{max}$.

The validity of the calibration can be checked by examining intermediate velocities.

For the x-wire, each sensor must be calibrated separately. This calibration is performed by rotating the probe until one sensor is perpendicular from the velocity measured by the pitot-static probe. The second sensor is calibrated by rotating the probe in the opposite direction until that sensor is normal to the flow.

4.3 EXPERIMENTAL TECHNIQUES

Data were obtained for a U_s (external velocity at the step) of 100 ft/s. Initially the single wire probe was employed to determine the boundary layer profile at the step and to insure that the boundary layer was turbulent. All mean velocity measurements in the upper wake region were obtained with the x-wire probe since it is in this region that the normal component of the mean velocity reaches its maximum. The mean velocity profile of the reverse flow region was obtained with the single wire. Just downstream of reattachment, the normal component of the mean velocity is still important and the x-wire was used for all measurements up to $x/H = 9$ ($x/H = 0$ is the base of the step, and reattachment occurs between $y/H = 5$ and $x/H = 6$). Farther downstream, the normal component of the mean velocity is less than 3 percent of the transverse component and the single wire was used for mean velocity profiles. All turbulent fluctuations were measured with the x-wire. The total region studied was between $x/H = 0$ and $x/H = 20$ and from $y/H = 0$ to $y/H = 3$ near the separated region and from $y/H = 0$ to $y/H = 4$ farther downstream.

5. RESULTS AND DISCUSSION OF THE EXPERIMENTAL INVESTIGATION

Hot wire measurements were obtained with the velocity at the step (U_s) at 100 ft/s which corresponds to a Reynolds number ($Re_H = U_\infty H/\nu$, where H denotes step height) of about 80,000. Figures 4.4 through 4.20 show all the pertinent data for various locations downstream of the step. Figure 4.4 shows the pressure distribution on the wall upstream and downstream of the step. This pressure distribution has been normalized by the reading obtained 7 inches ($3.5 H$) upstream of the step. It is obvious due to the change in cross-sectional area that the static pressure at far downstream positions would never approach the upstream free streamline. Mean velocity profiles are quite interesting in two respects: First, the \bar{U} profile is not continuous at the point of zero velocity near the end of the wake. This is probably due to the fact that the local flow is quite unsteady in this region and an average over time with a hot wire cannot discriminate between positive and negative directional flows. Secondly, the wall boundary layer downstream of reattachment develops extremely rapidly giving rise to a complex \bar{U} velocity profile in this region.

The magnitude of the normal component of the mean velocity, \bar{V} , increases as the main flow turns and the mixing layer spreads and reaches a maximum of about 12 percent of the external flow velocity. It subsequently decreases after reattachment, becoming less than 3 percent of the external velocity for $x/H > 10$.

The $(\overline{u'^2})^{1/2}/U_a$ and $(\overline{v'^2})^{1/2}/U_a$ turbulent velocity components increase throughout the wake region and achieve a maximum value of about 20 percent of the external velocity just downstream of reattachment. In the wake region, these components attain a maximum at the center of the shear layer. Far downstream in the redevelopment region, the turbulent components are steadily decreasing, but they have a nearly constant value across the entire shear layer.

The Reynolds stress component, $\rho \overline{u' v'} / \rho U_a^2$, increases throughout the wake region to a maximum value of 0.014 at about the point of reattachment and then decreases quite rapidly throughout the redevelopment region. This is shown more clearly in Fig. 4.21 where the maximum turbulent shear stress is plotted along with the data of Tani, et al. [53].

There have been some questions raised about why the maximum turbulent shear stress is so large in the wake region. For plane, two-dimensional mixing of a uniform stream with a quiescent fluid, the maximum $\rho \overline{u' v'}$ is about $0.01 \rho U_\infty^2$. Bradshaw and Wong [51] suggest that the shear stress is much larger because the effective velocity difference across the free shear layer is not U_∞ but $(1 + \phi_b) U_\infty$. They point out, however, that the reverse flow velocity does not seem to exceed $0.2 U_\infty$ so that this cannot entirely explain why some of the $\rho \overline{u' v'}$ measurements, e.g., that of Arie and Rouse [52] ($0.02 \rho U_\infty^2$), are so large. The maximum reversed flow for the present experiment is about $0.22 U_a$ which would lead through this argument to a $\rho \overline{u' v'}$ value of 0.148 which is in good agreement with the measured value. If a closer look is taken at the previously mentioned experiments and results of this study, it appears that Bradshaw and Wong's initial argument [51] for $\rho \overline{u' v'}|_{\max} = 0.01 (1 + \phi_b)^2 \rho U_a^2$ may be essentially correct. First, it is important that one employ the correct value for the free stream velocity in calculating this value. With flows over a wedge as an example, the local free stream velocity in the wake region may be as large as $1.3 U_\infty$ and the local effective velocity difference may be much larger than one would expect due to the large acceleration around the body. Secondly, and probably more important, the reverse flow velocity can exceed $0.2 U_a$. Figure 4.22a shows the variation of ϕ_b (the maximum reverse flow velocity) from the results of previous theoretical calculations as a function of wedge angle compared with the experimental data points of Tani, et al. [53], and Arie

and Rouse [52]. For a flat plate normal to the flow, ϕ_b attains a value of about 0.35. It is suspected that ϕ_b is dependent upon the size of the wake; this relationship is shown in Fig. 4.22b where ϕ_b is plotted against x_r/H and x_r is the reattachment point. It may be just as logical to correlate ϕ_b with the height of the wake bubble, since the length-to-height ratio of the wake appears to be almost constant with a value of the order of 5 or 6.

Utilizing these results to determine a maximum shear stress given by $0.01 (1 + \phi_b)^2 \rho U_a^2$, Fig. 4.23a correlates the $\rho \overline{u'v'}|_{\max}$ versus θ and Fig. 4.23b correlates $\rho \overline{u'v'}|_{\max}$ versus x_r/H . Agreement with experiments is excellent except for one of Mueller and Robertson's data points [54] which corresponds to an extremely large initial boundary layer ($\delta = 0.5H$).

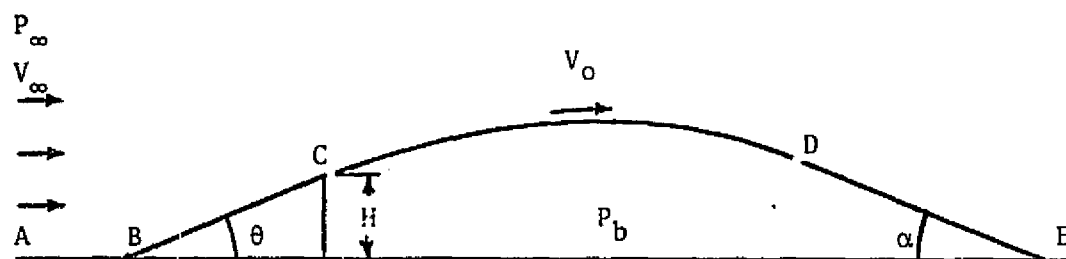
Figure 4.24 shows the displacement and momentum thickness obtained by integrating the experimental data. This information can be used to estimate the surface shear stress by employing the Ludwig-Tillman formula, $c_f = 0.246 \times 10^{-0.678H} \times R_{\delta^{**}}^{-0.268}$, where H is the shape factor and $R_{\delta^{**}}$ is the Reynolds number based on the momentum thickness. Figure 4.25 shows a comparison between the shear stress calculated in this manner, Bradshaw's experimentally measured shear stress, and the shear stress calculated with the Ludwig-Tillman formula using Bradshaw and Wong's data [51]. Although the boundary layer is severely disturbed, the relationship between the surface shear stress and the integral parameters still appears to be applicable and the results are in fairly good agreement. This behavior illustrates the capability of integral methods in dealing with very complex flow phenomena.

6. CONCLUSIONS

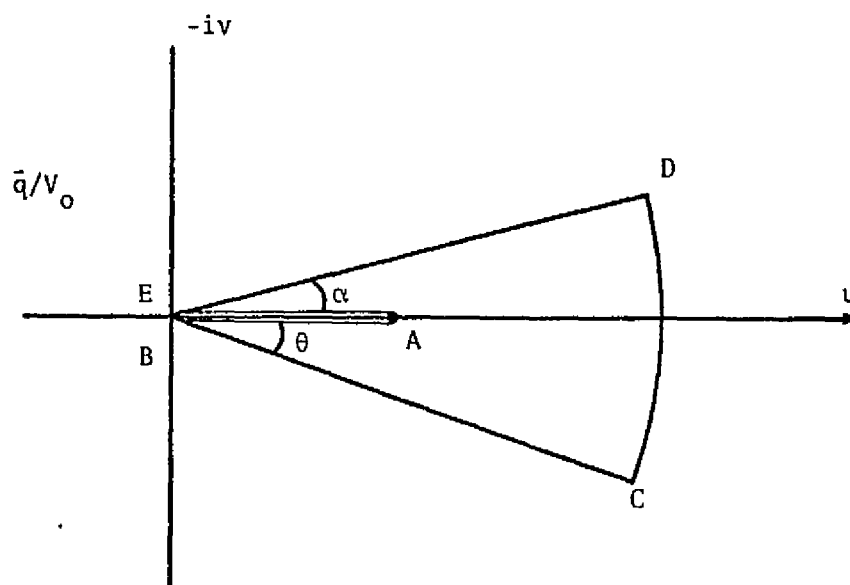
It is apparent from the present investigation that the most important aspect of separated flow problems of this type is the determination of the base pressure. Such a determination cannot be accomplished without consideration of the viscid-inviscid interaction phenomenon. Once this has been achieved, determination of the drag coefficient is straightforward. The present theoretical analysis has provided an effective method of determining this base pressure for separated flows past wedges with a minimum of empirical information.

Results of the theoretical analysis have been shown to be in good agreement with the available experimental data. It is obvious that the major remaining question is the dependency of results upon σ . Unfortunately, this aspect of the problem cannot be resolved until an extensive experimental study has been performed which will also include effects of the wind tunnel interference into consideration so that results that truly represent flow over a body in an infinite stream can be ascertained. Another aspect of the problem that requires further experimental study is the turbulence structure within, and downstream of, the wake. An eddy diffusivity model is employed that has proven to be adequate but it certainly deserves further consideration and improvement.

It is also expected that the redeveloping flow after reattachment can be described by an integral analysis which would consider the important overall properties of this region and efforts in this direction should be continued.



(a) Incompressible Flow past a Wedge



(b) Hodograph Plane

Figure 2.1 The Corresponding Inviscid Flow

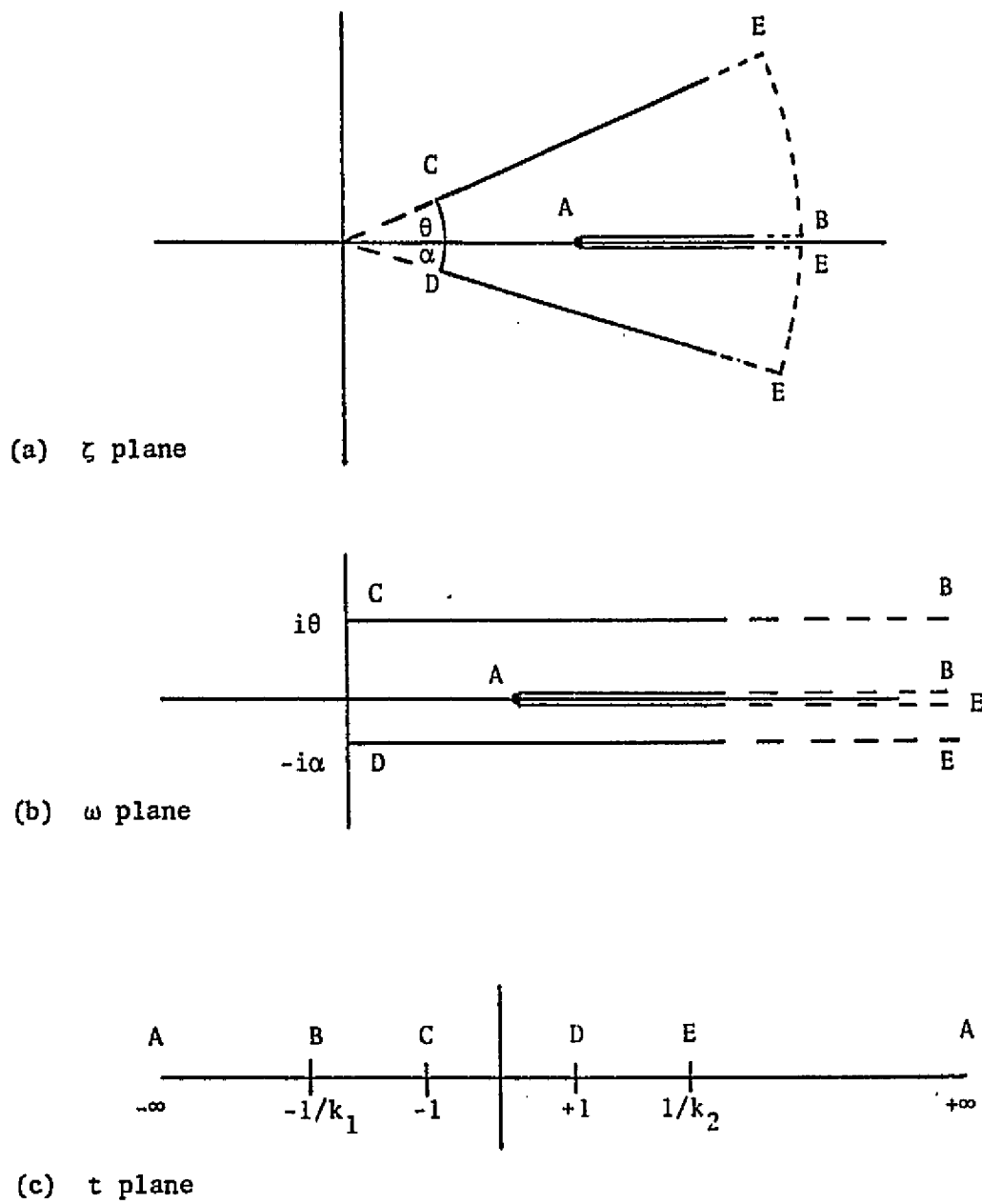
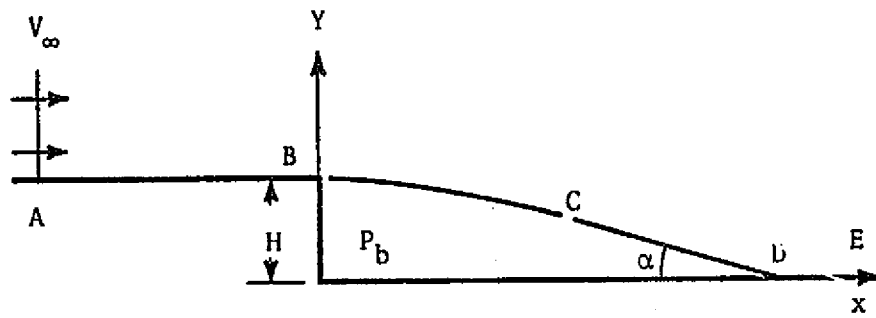
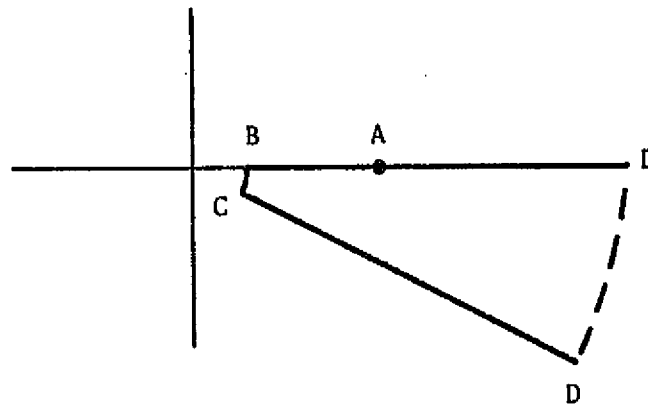


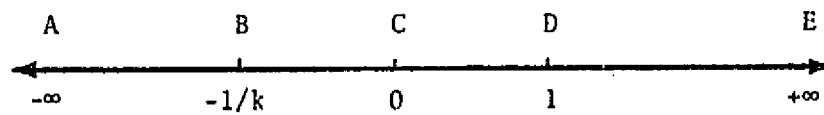
Figure 2.2 Transformations for the Corresponding Inviscid Flow



(a) Physical plane



(b) ζ plane



(c) t plane

Figure 2.3 Incompressible Flow past a Backstep [45]

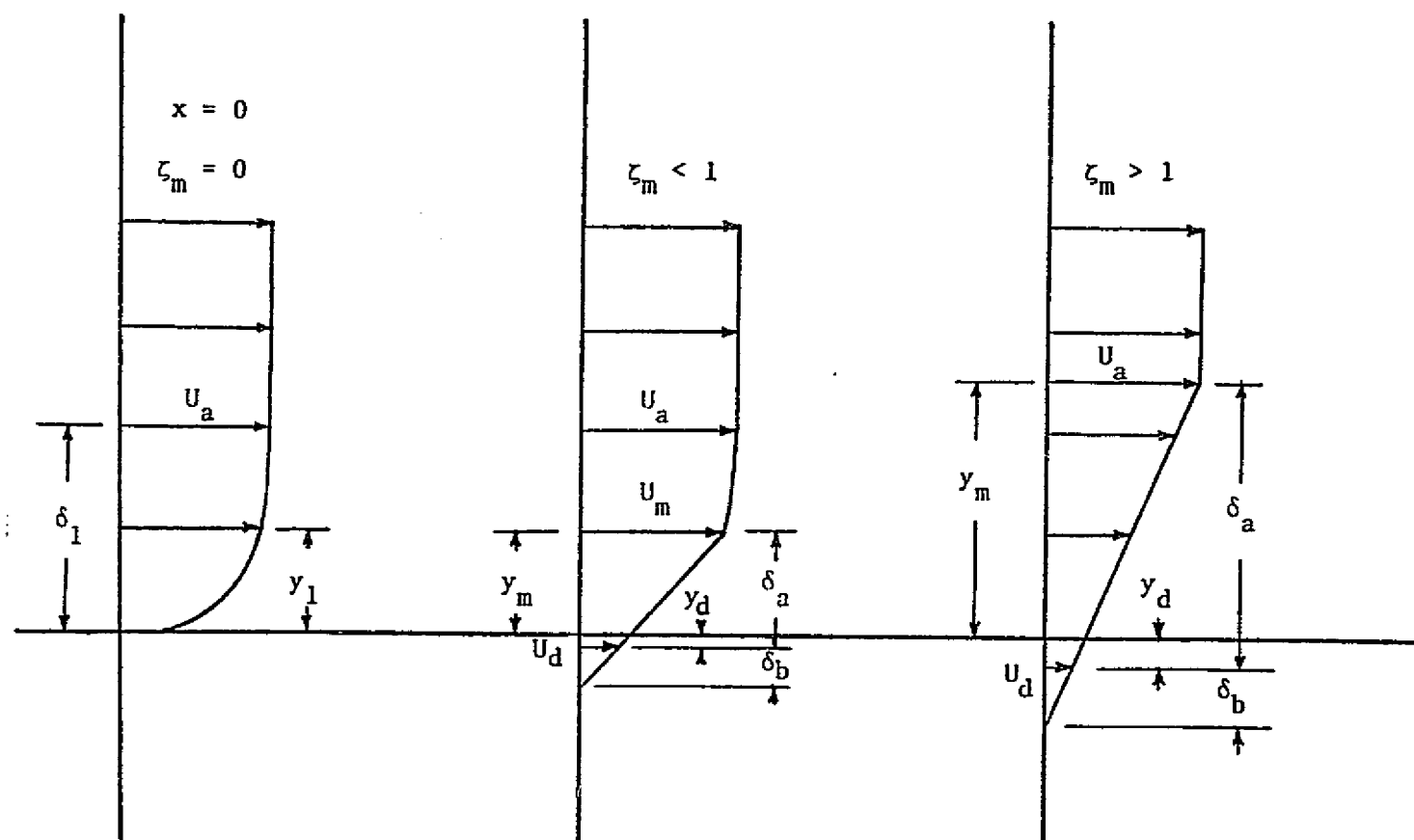


Figure 2.4 Quasi-constant Pressure Turbulent Jet Mixing Region

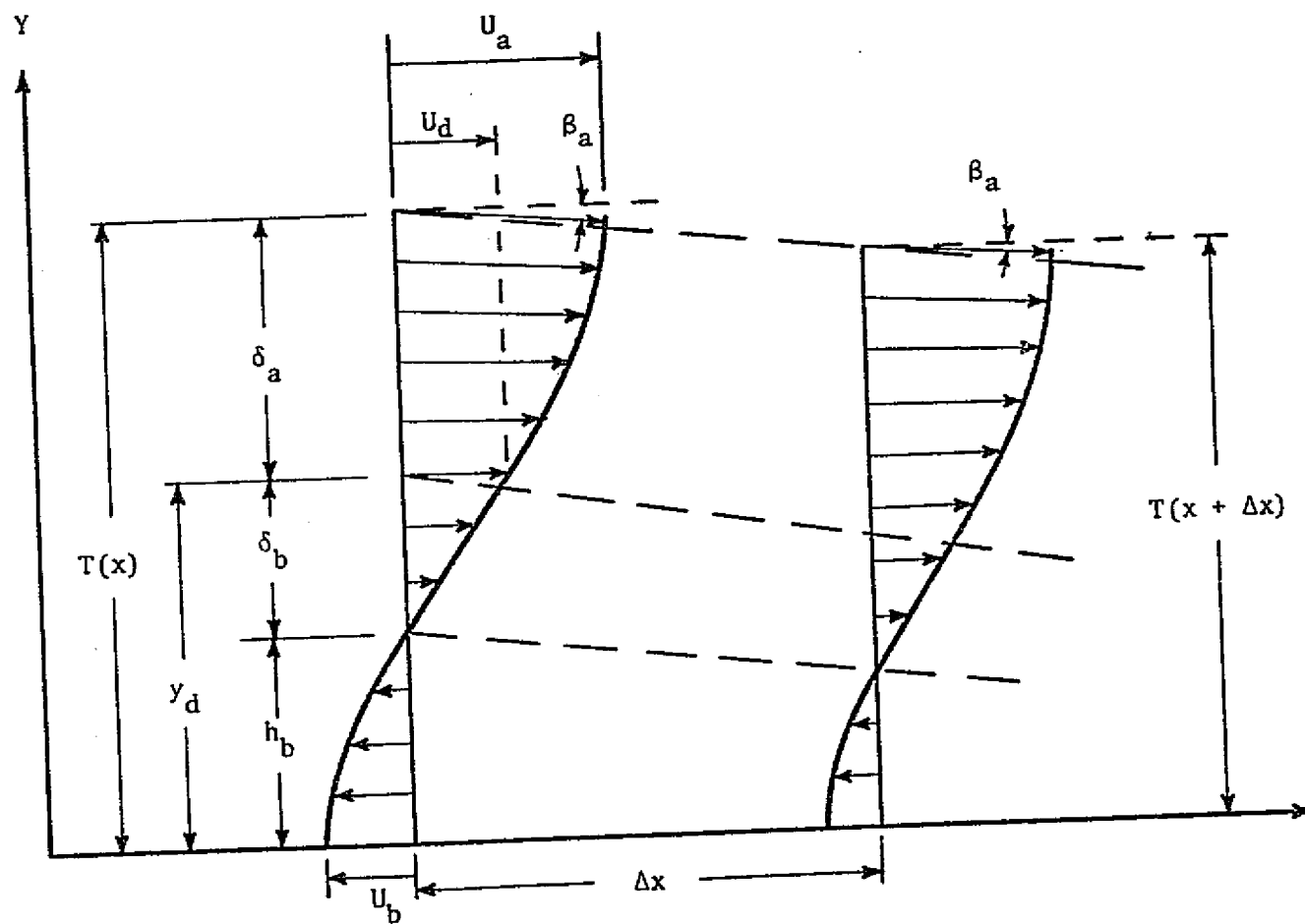


Figure 2.5 Recompression Region

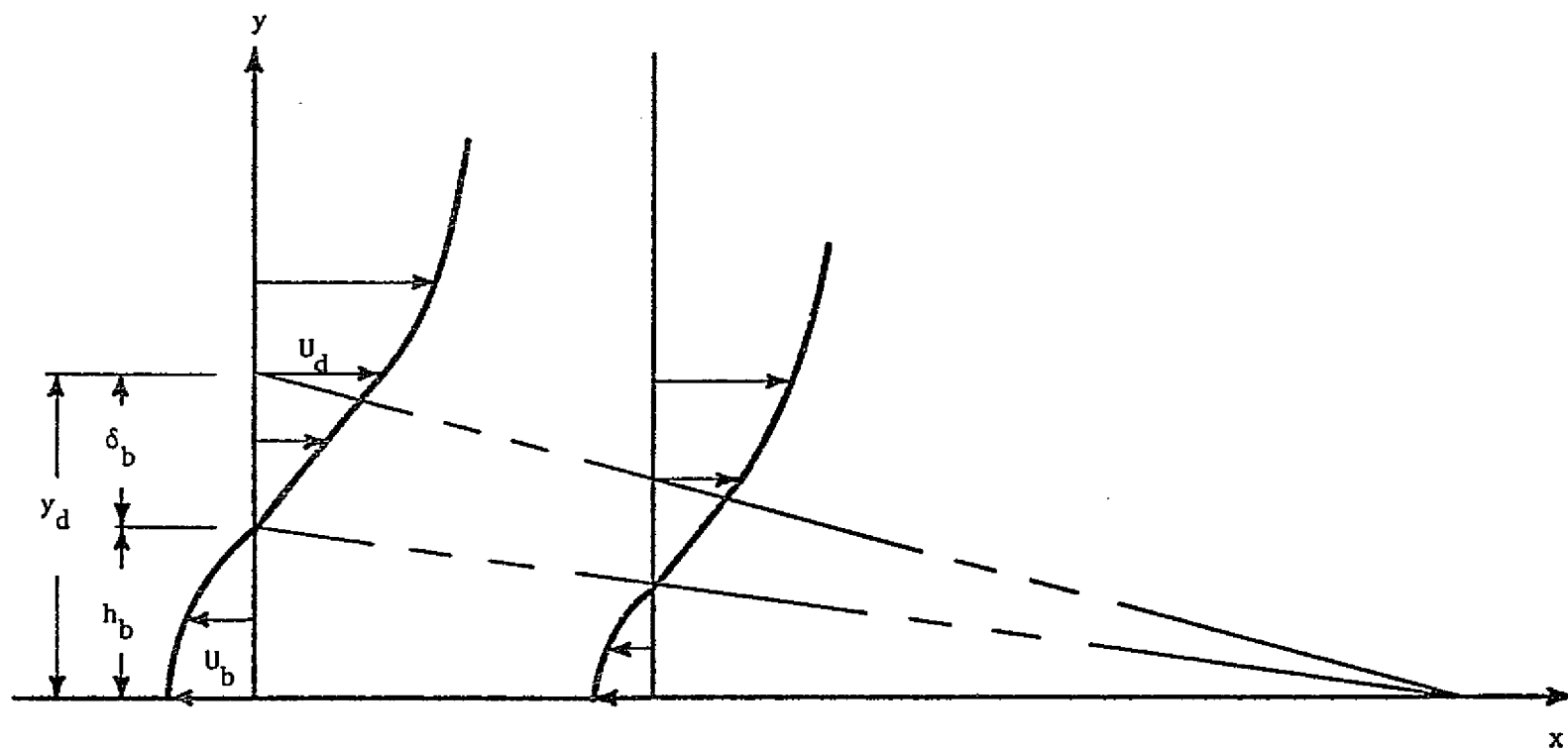


Figure 2.6 Locally Triangular Flow Geometry

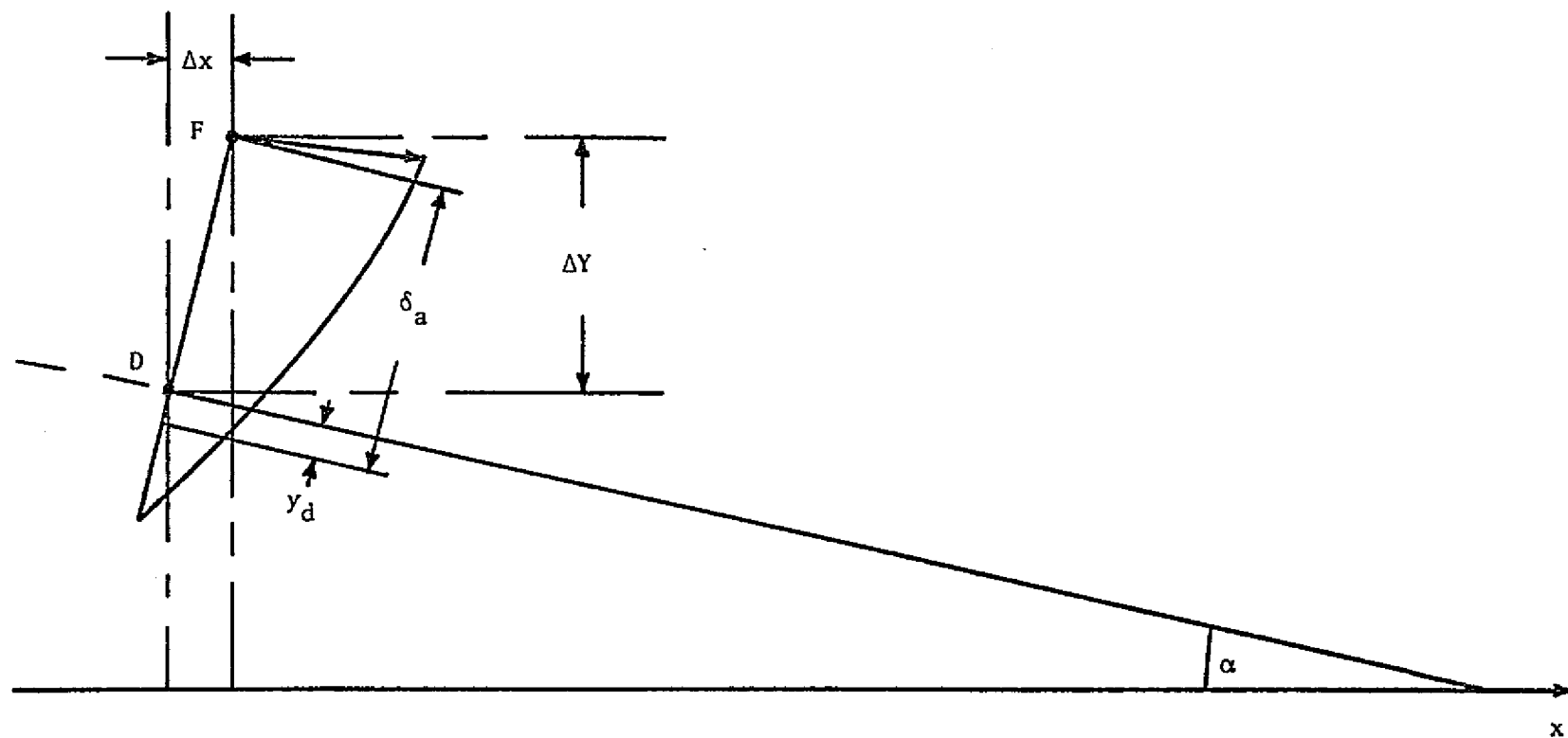


Figure 2.7 Location of the Initial Section for the Recompression Process

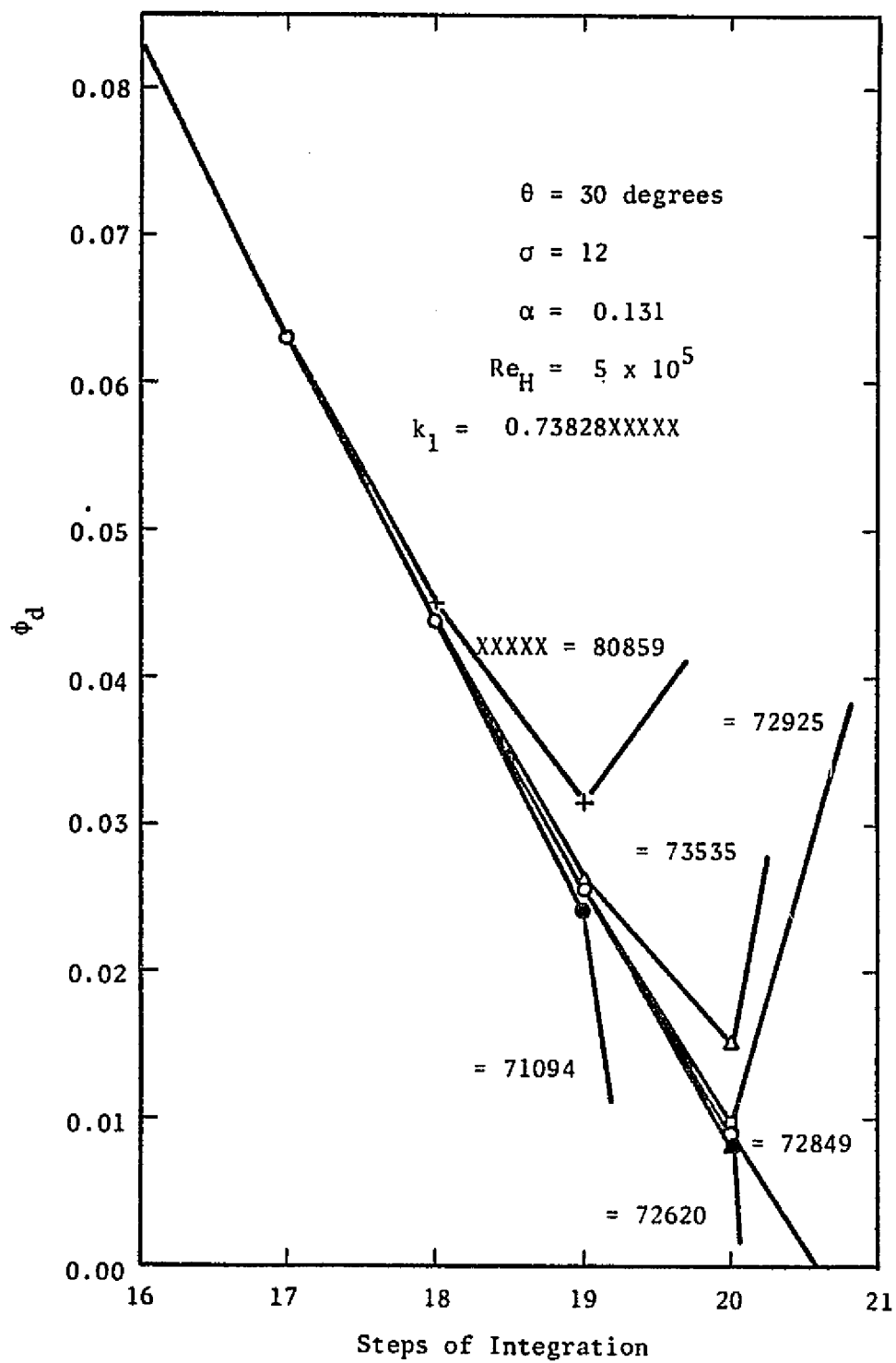


Figure 2.8 Saddle Point Type Singularity at the Reattachment Point

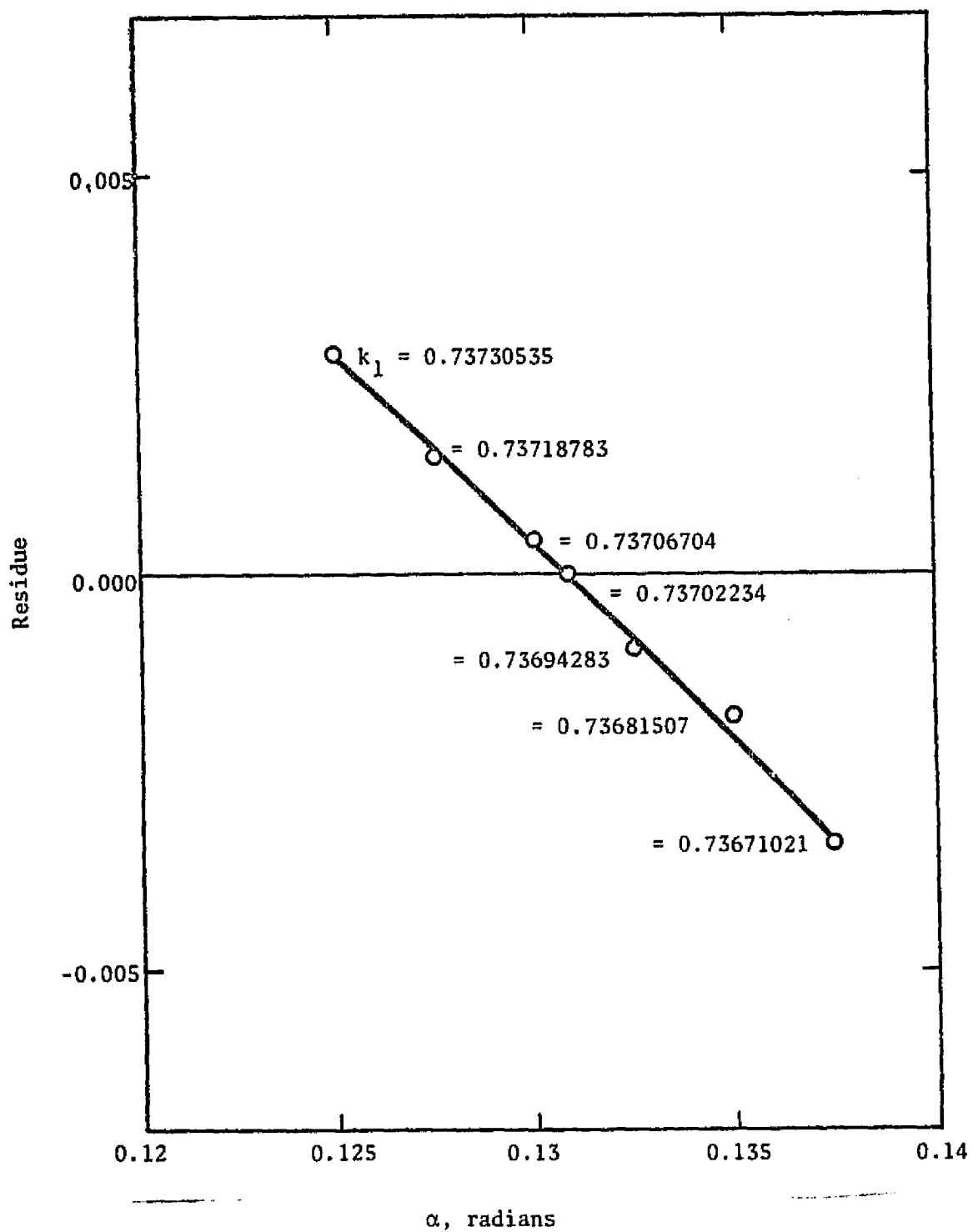


Figure 2.9 Residue Curve for $\theta = 30^\circ$ ($\sigma = 12$, $Re_H = 5 \times 10^4$)

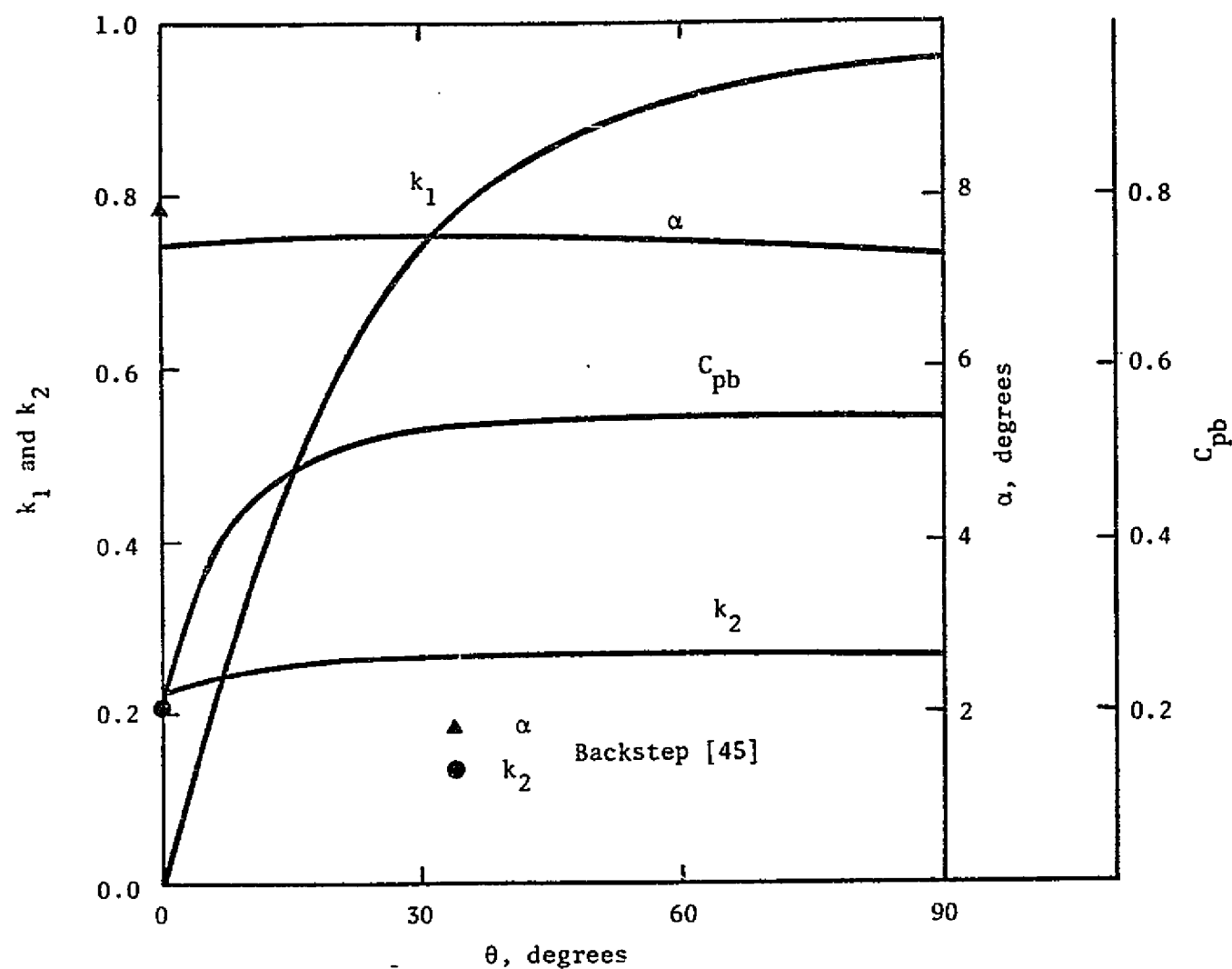


Figure 3.1 Parameters of the Corresponding Inviscid Flow for $\sigma = 12$

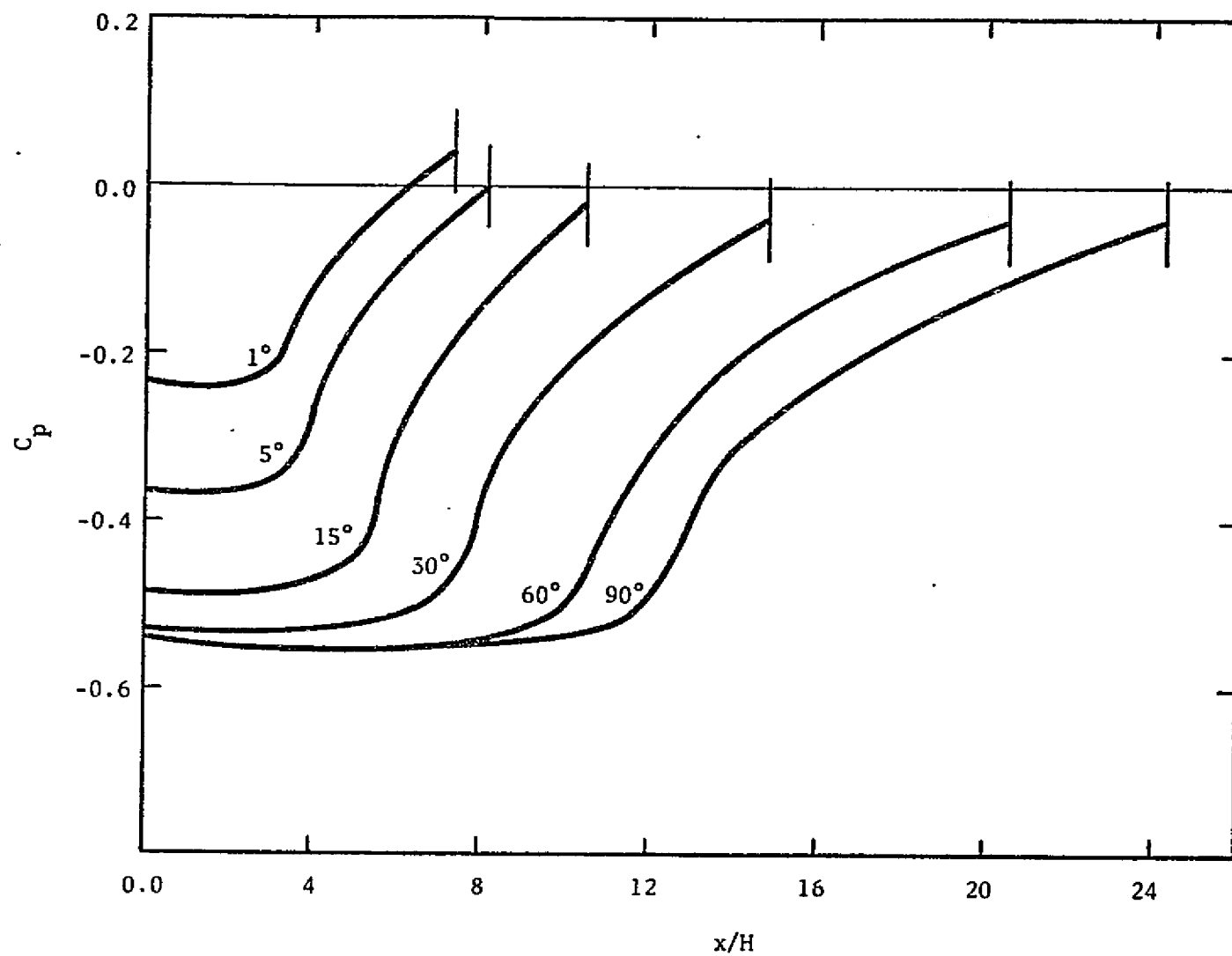


Figure 3.2 Pressure Distributions as a Function of Wedge Angle
($\sigma = 12$, $Re_H = 5 \times 10^4$)

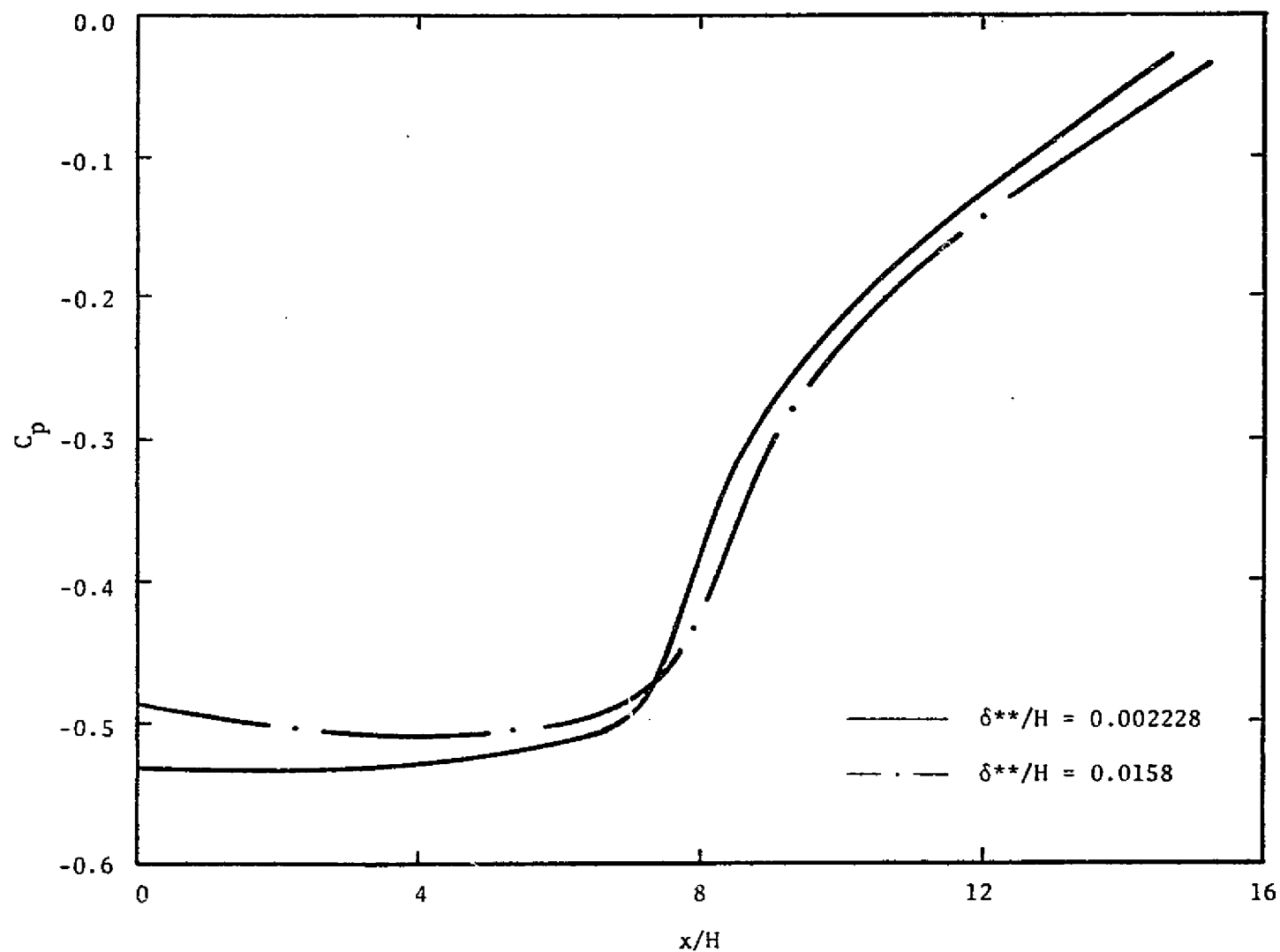


Figure 3.3 Pressure Distribution as a Function of the Initial Boundary Layer for $\theta = 30^\circ$, $\sigma = 12$

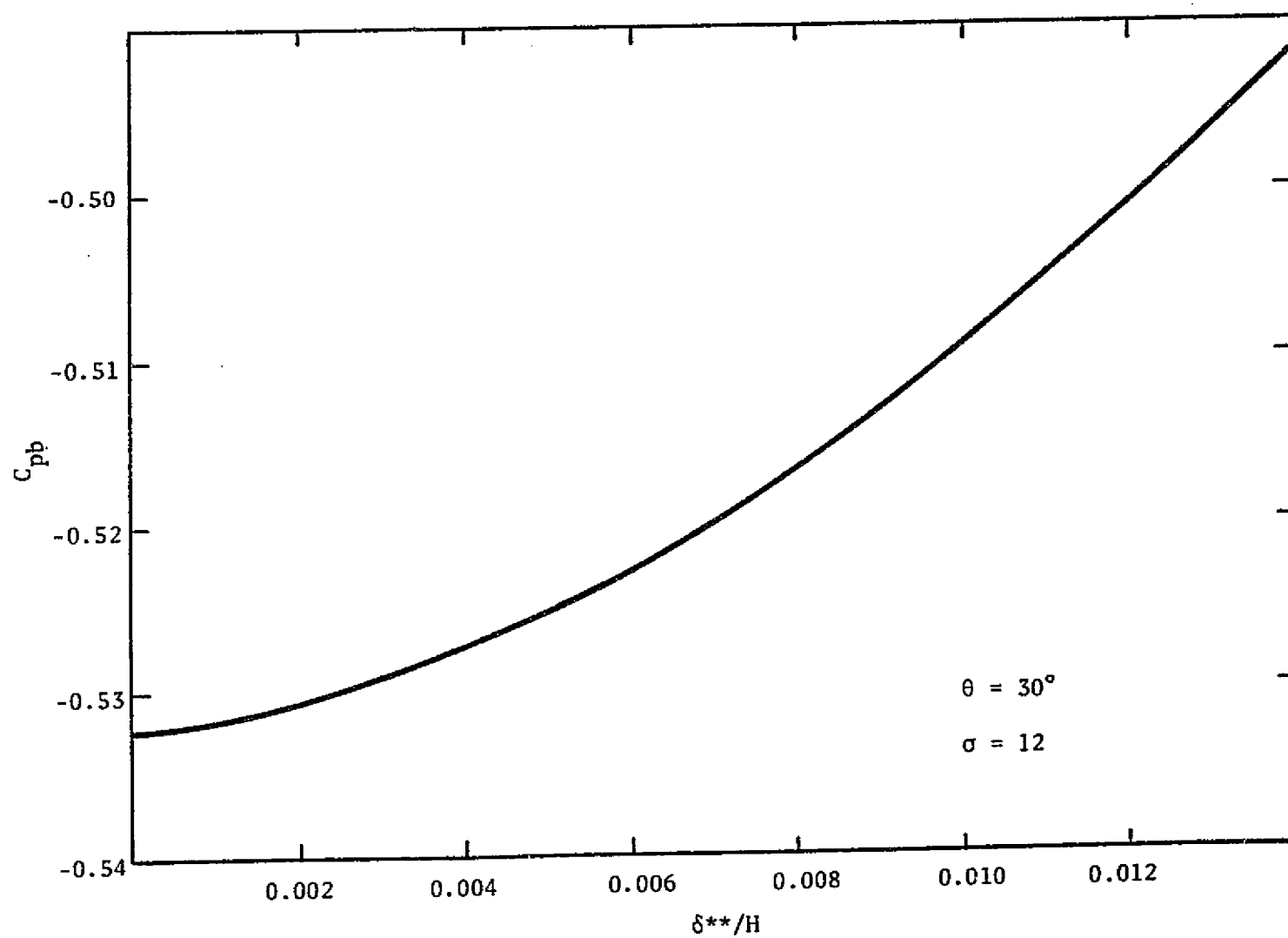


Figure 3.4 Variation of C_{pb} with the Initial Momentum Thickness

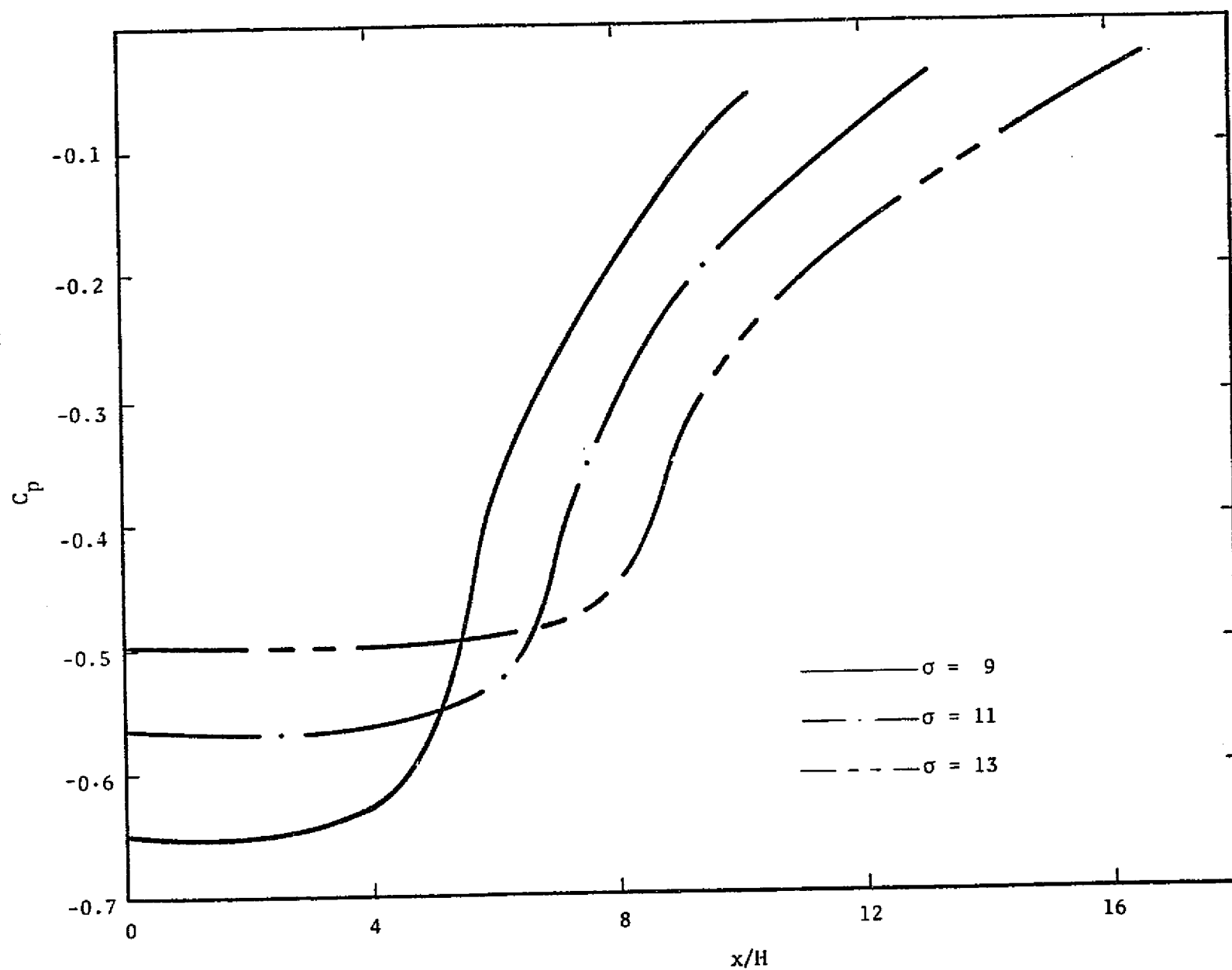


Figure 3.5 Pressure Distribution as a Function of σ for $\theta = 30^\circ$ and $Re_H = 5 \times 10^4$

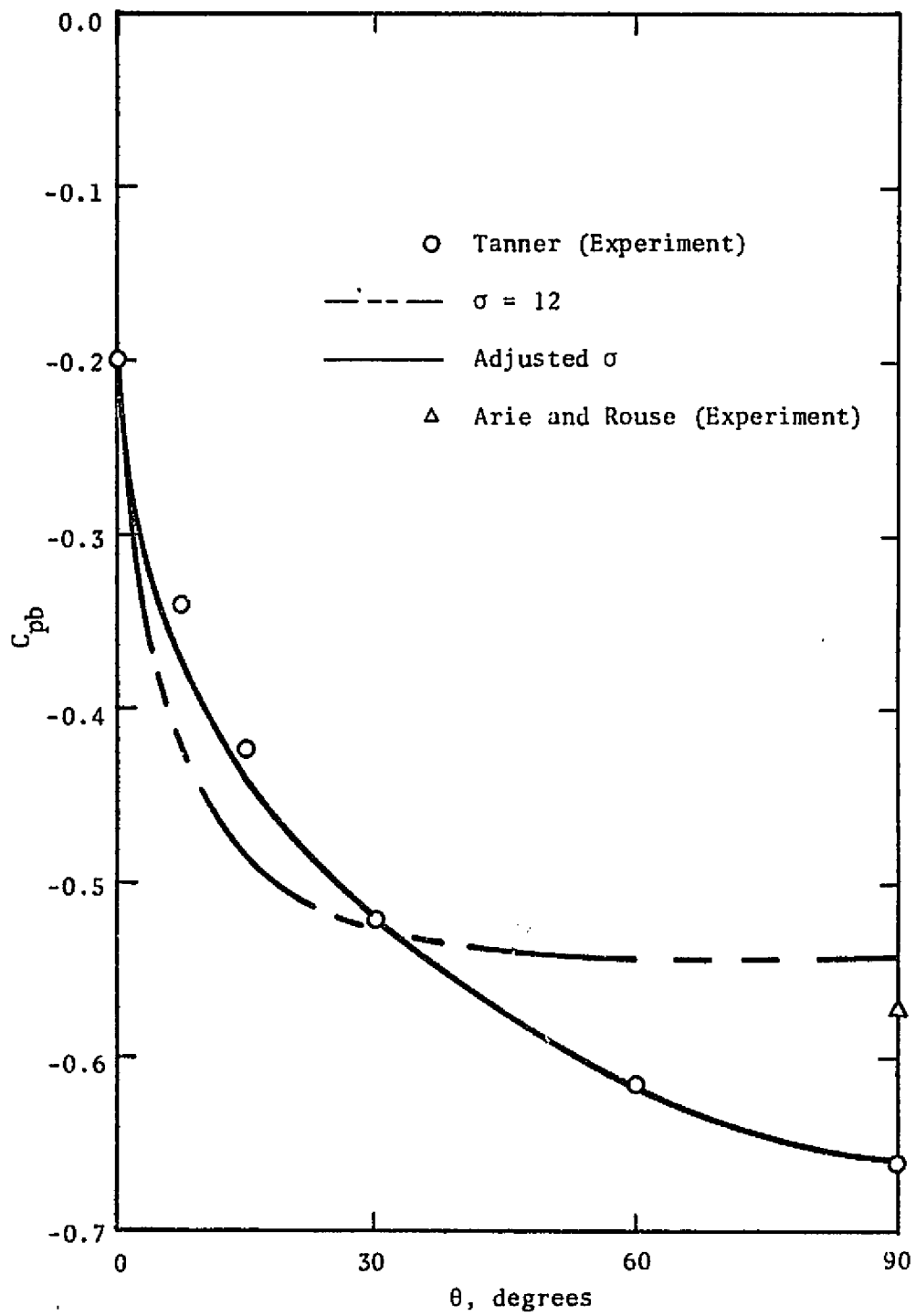


Figure 3.6 Variation of C_{pb} with θ for $Re_H = 5 \times 10^4$

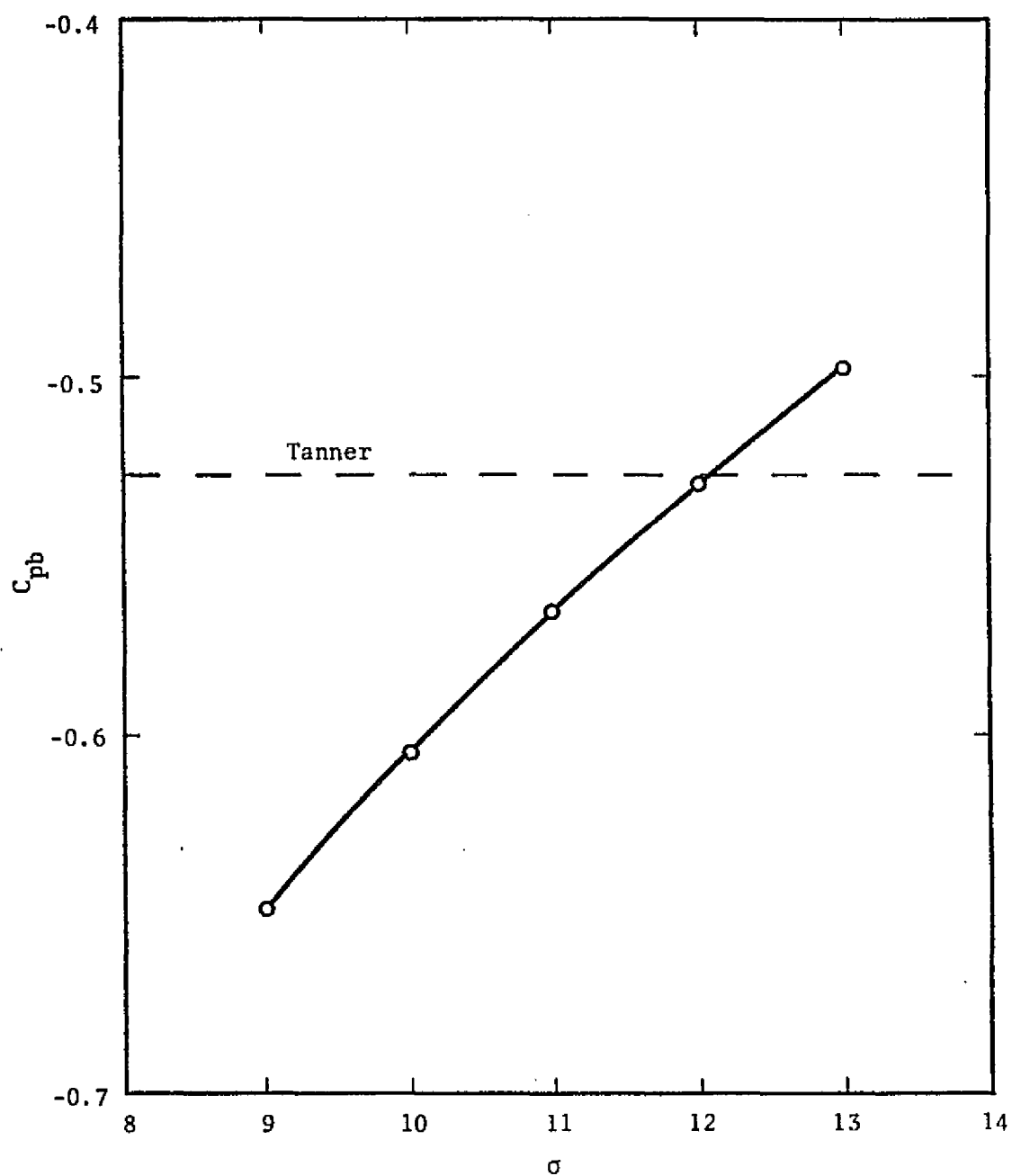


Figure 3.7 Determination of the Adjusted Value of σ
for $\theta = 30^\circ$ and $Re_{II} = 5 \times 10^4$

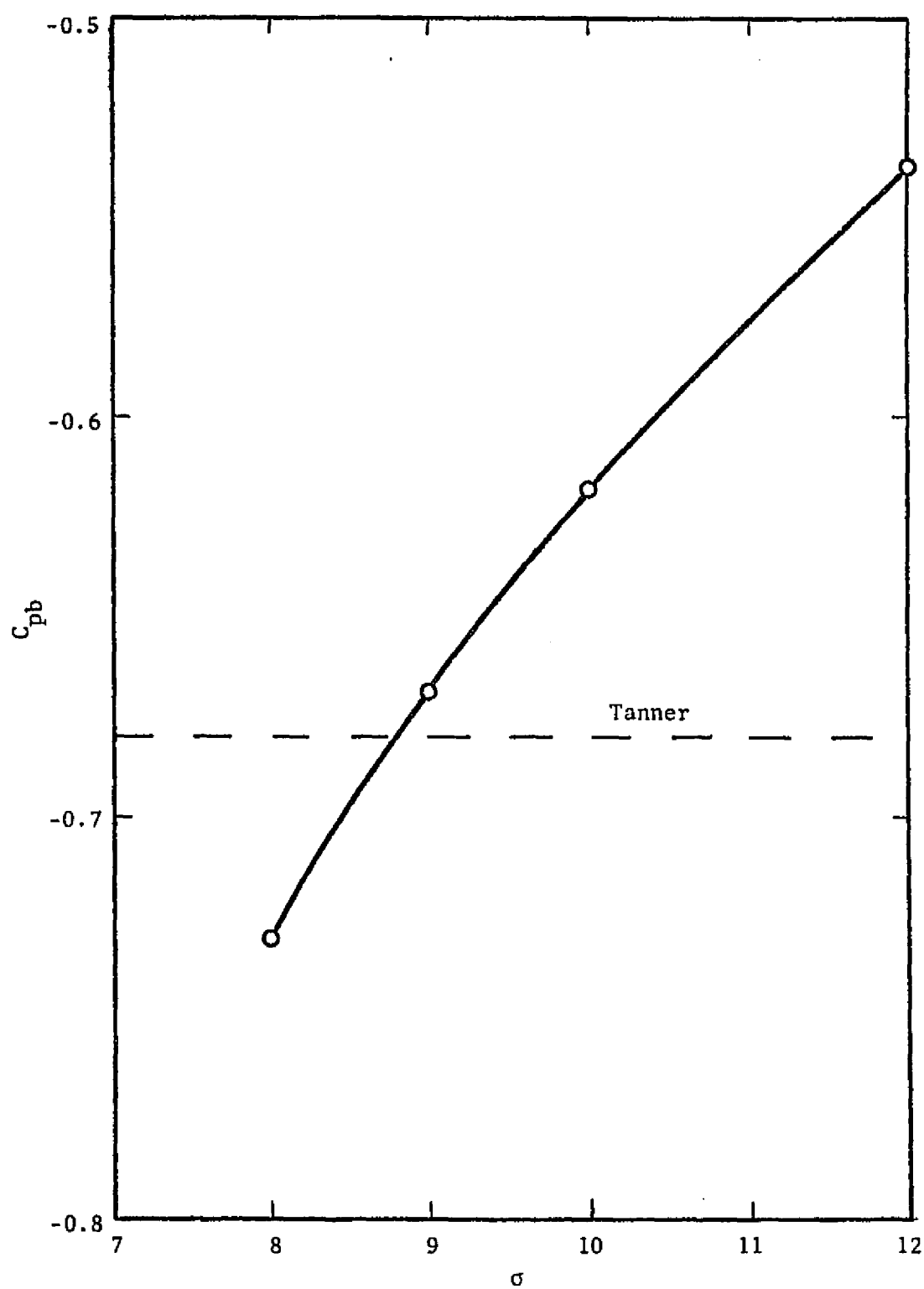


Figure 3.8 Determination of the Adjusted Value of σ
for $\theta = 90^\circ$ and $Re_H = 5 \times 10^4$

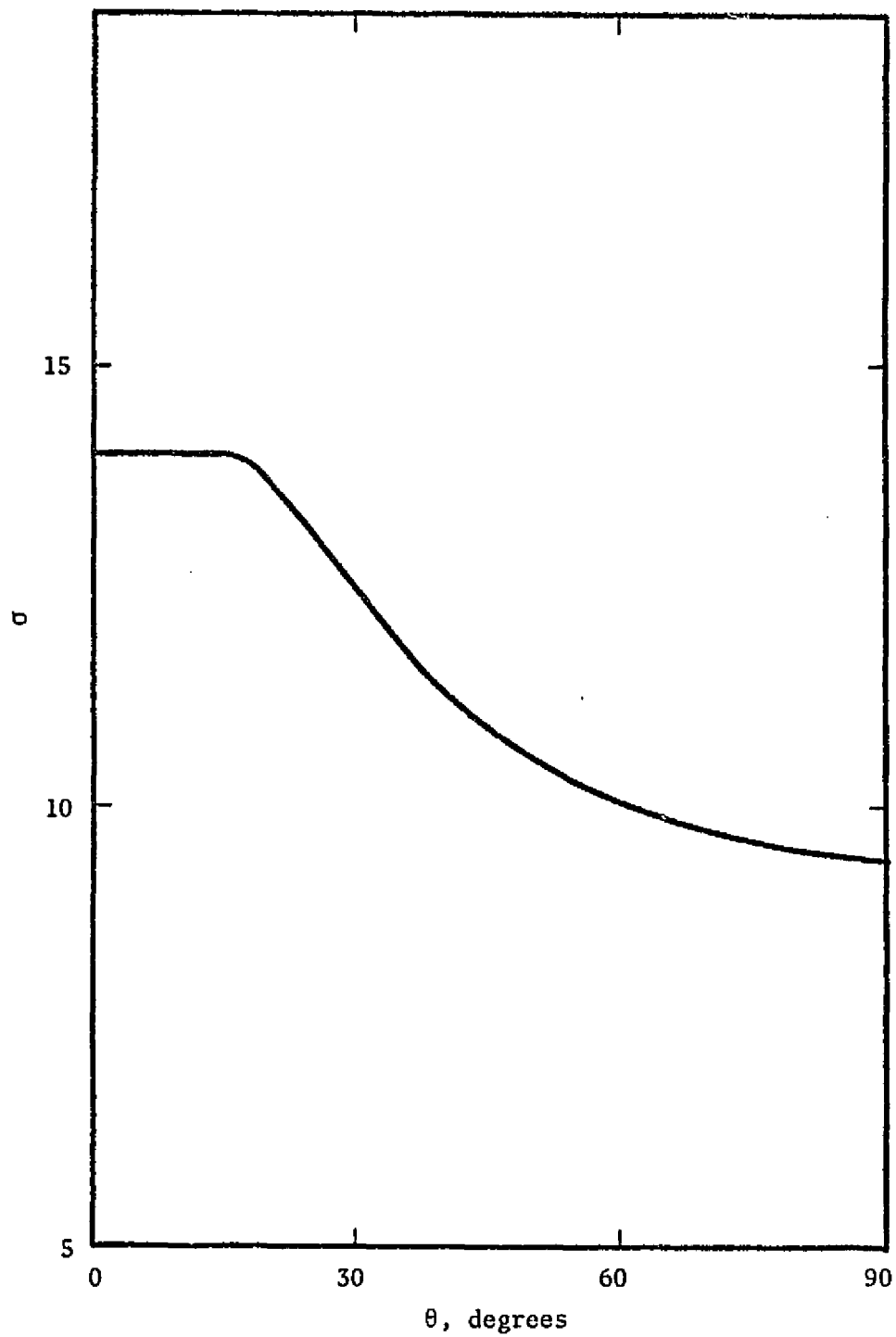


Figure 3.9 Variation of σ with θ Necessary to obtain Tanner's Base Pressure for $Re_H = 5 \times 10^4$

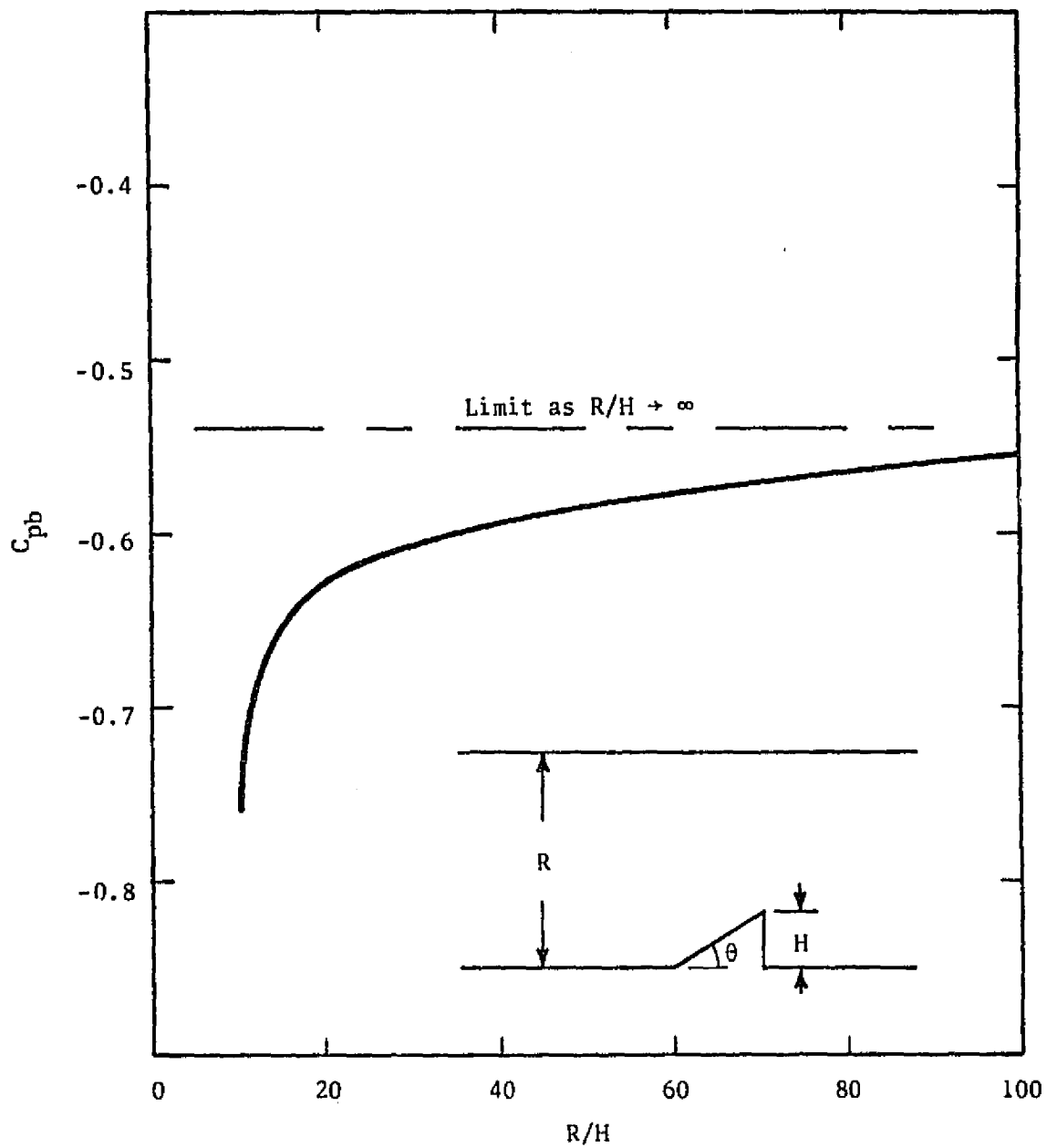


Figure 3.10 Effect of Wind Tunnel Wall on C_{pb} for $\theta = 30^\circ$, $\sigma = 12$, and $Re_H = 5 \times 10^4$

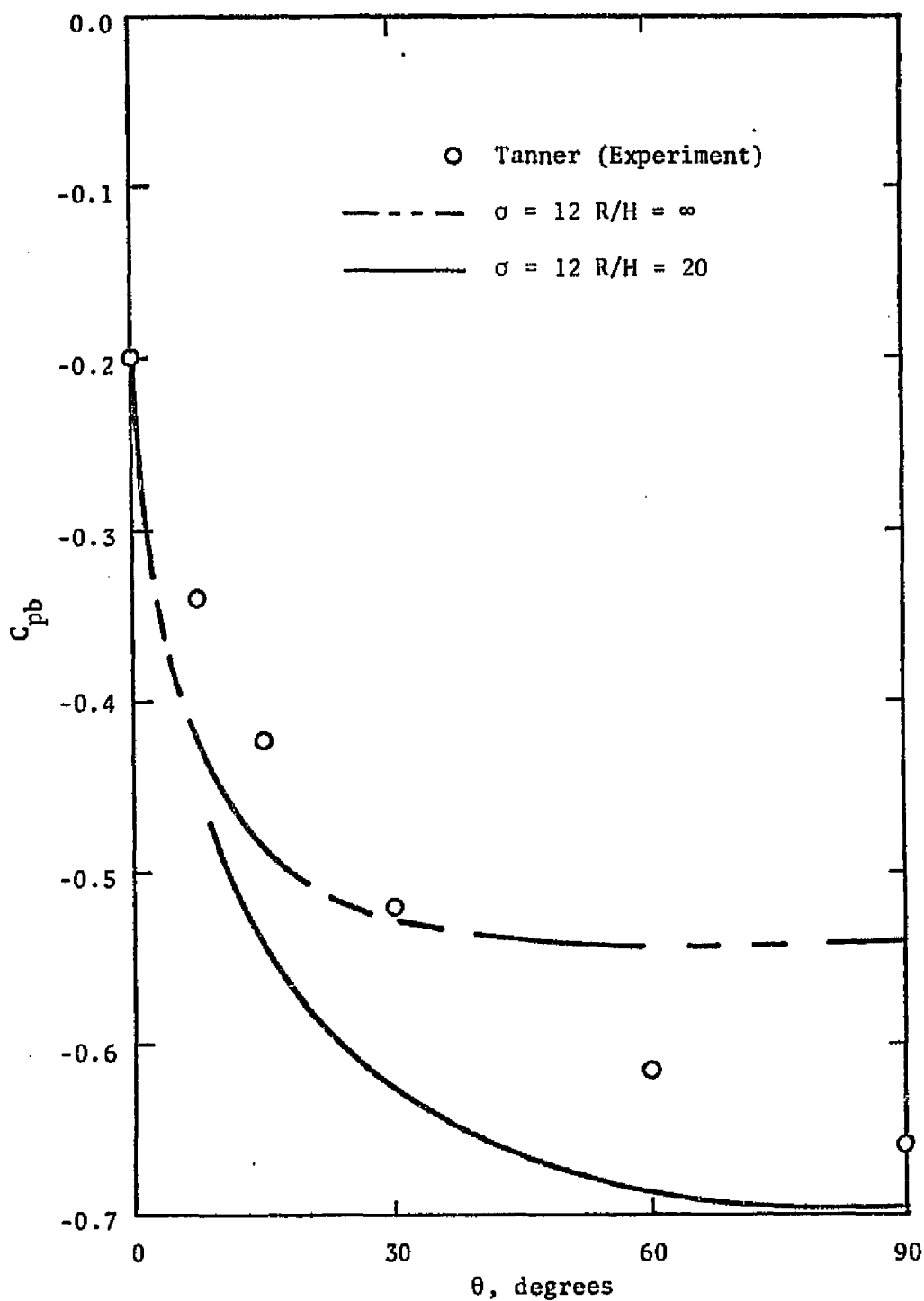


Figure 3.11 Effect of Wind Tunnel Wall compared to Tanner's Experimental Data for $Re_H = 5 \times 10^4$

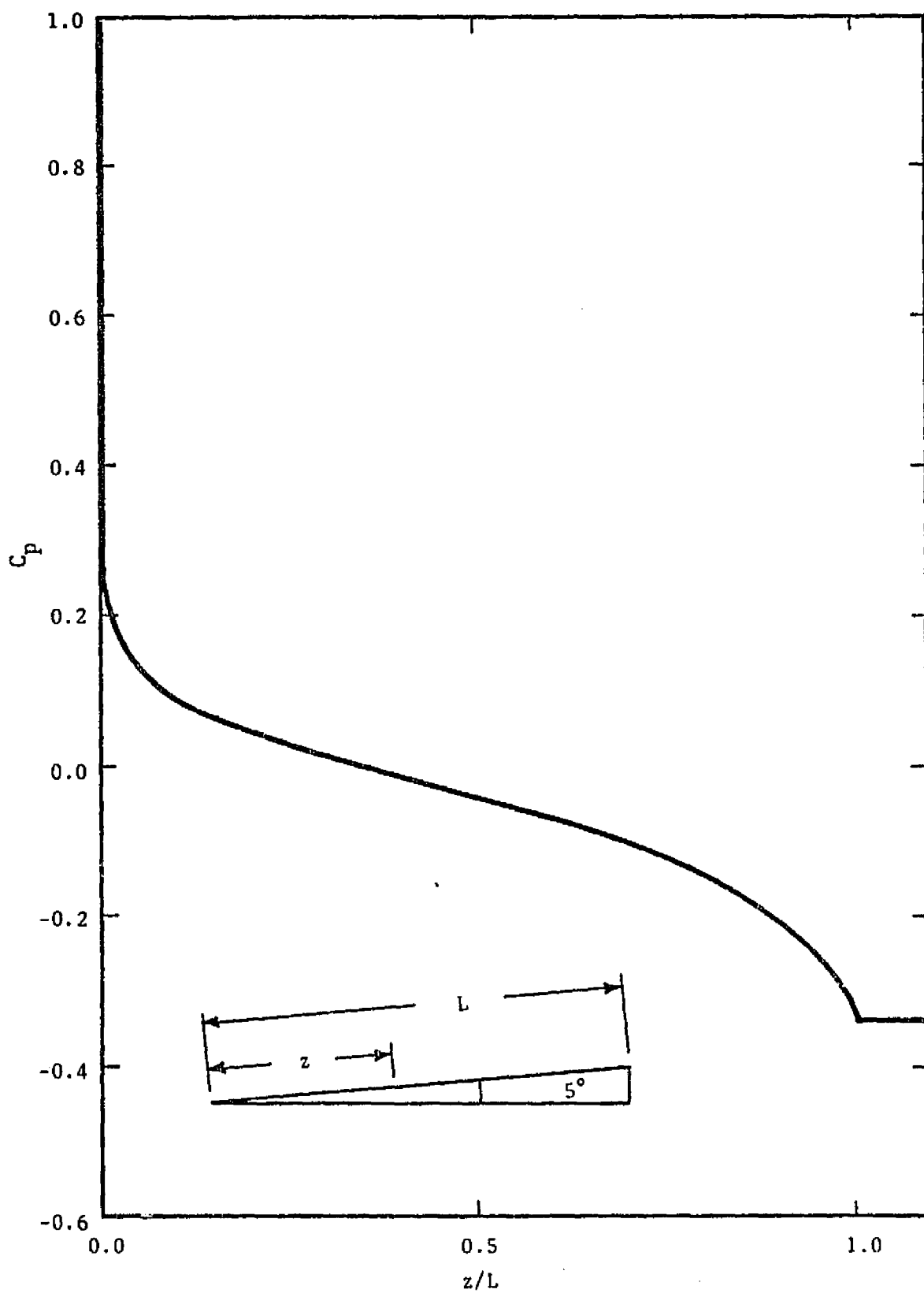


Figure 3.12 Pressure Distribution on the Surface of a 5° Wedge for $\sigma = 14$ and $Re_H = 5 \times 10^4$

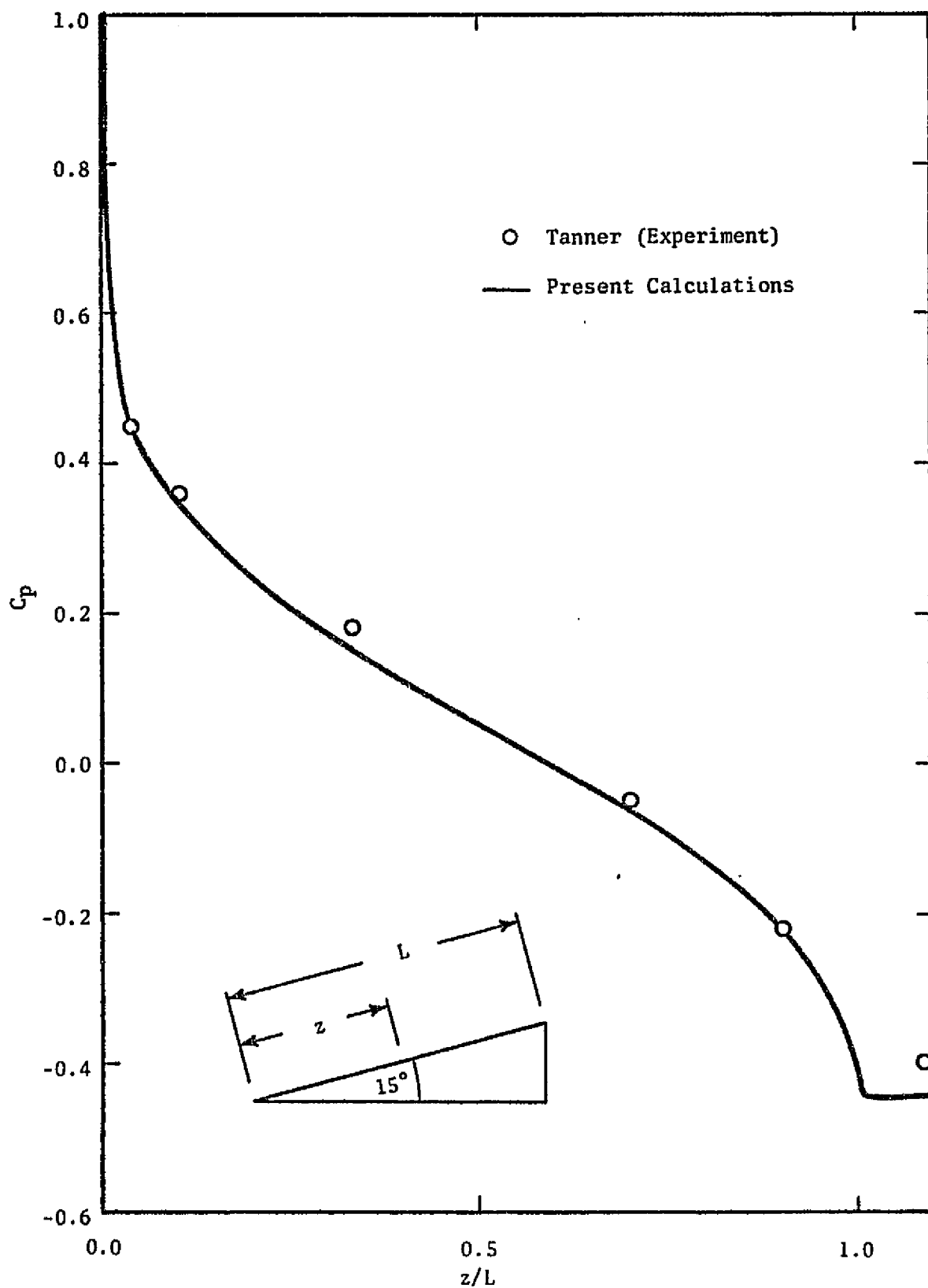


Figure 3.13 Pressure Distribution on the Surface of a 15° Wedge for $\sigma = 14$ and $Re_H = 5 \times 10^4$

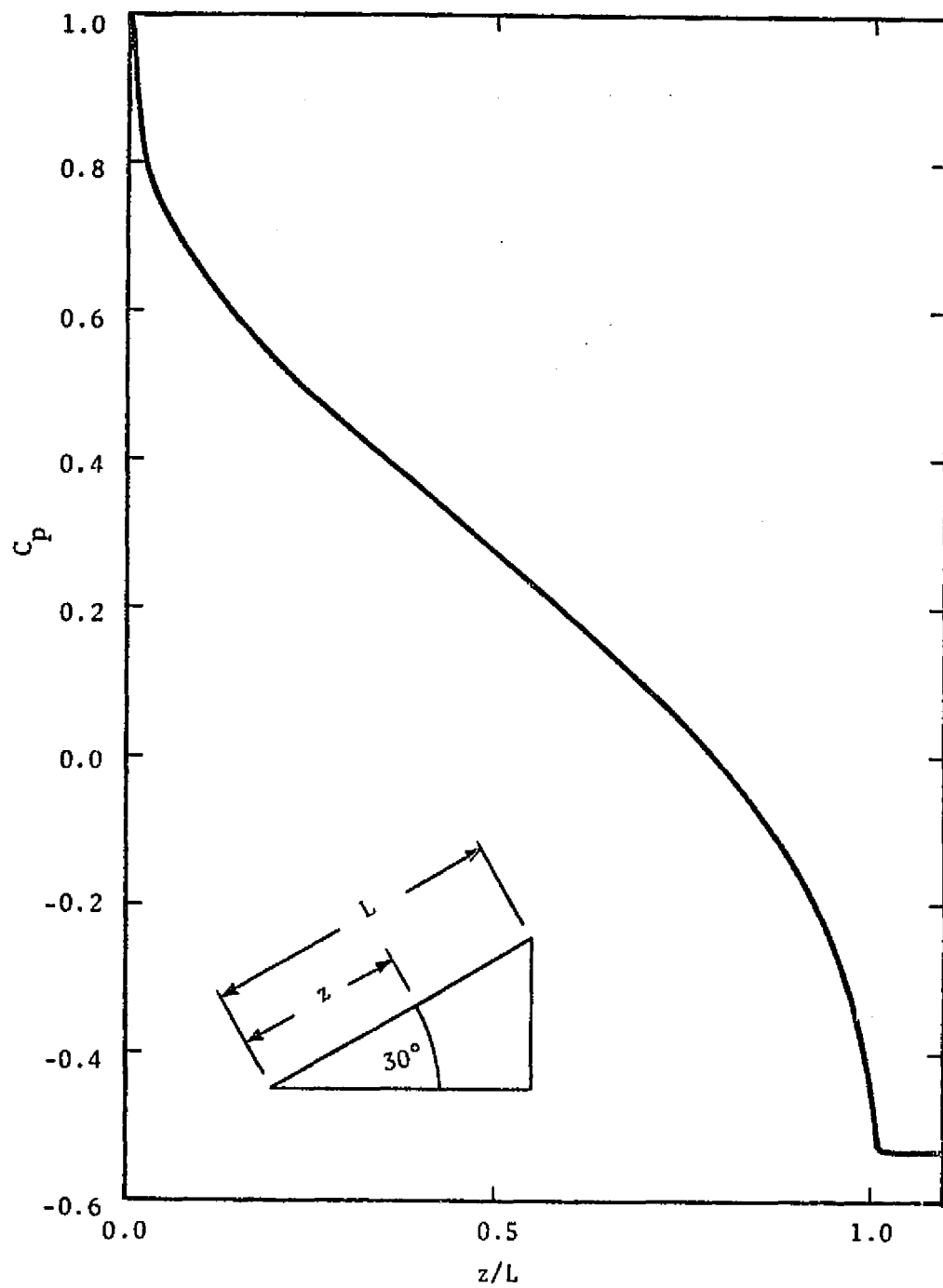


Figure 3.14 Pressure Distribution on the Surface of a 30° Wedge for $\sigma = 11$ and $Re_H = 5 \times 10^4$

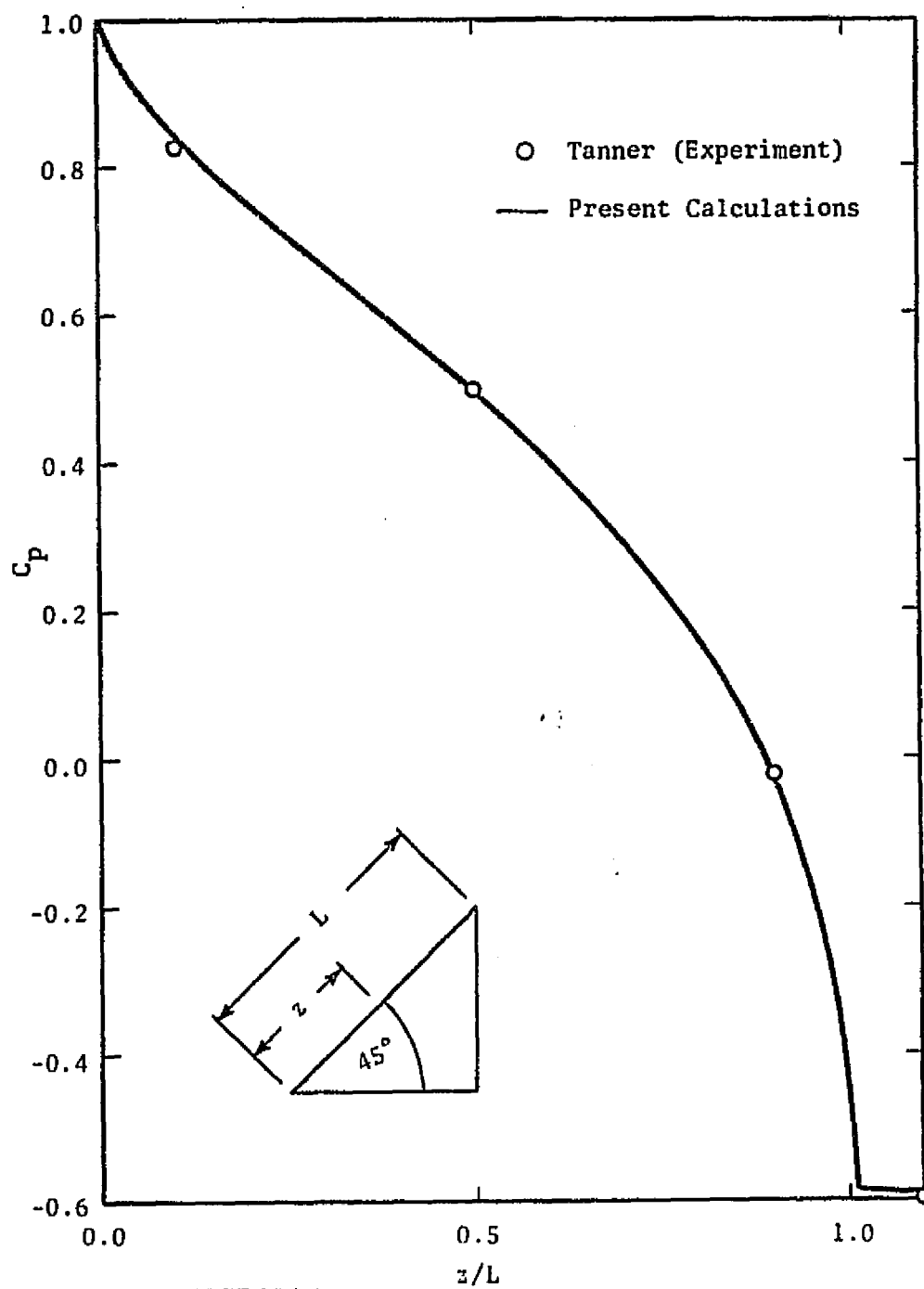


Figure 3.15 Pressure Distribution on the Surface of a 45° Wedge for $\sigma = 12$ and $Re_H = 5 \times 10^4$

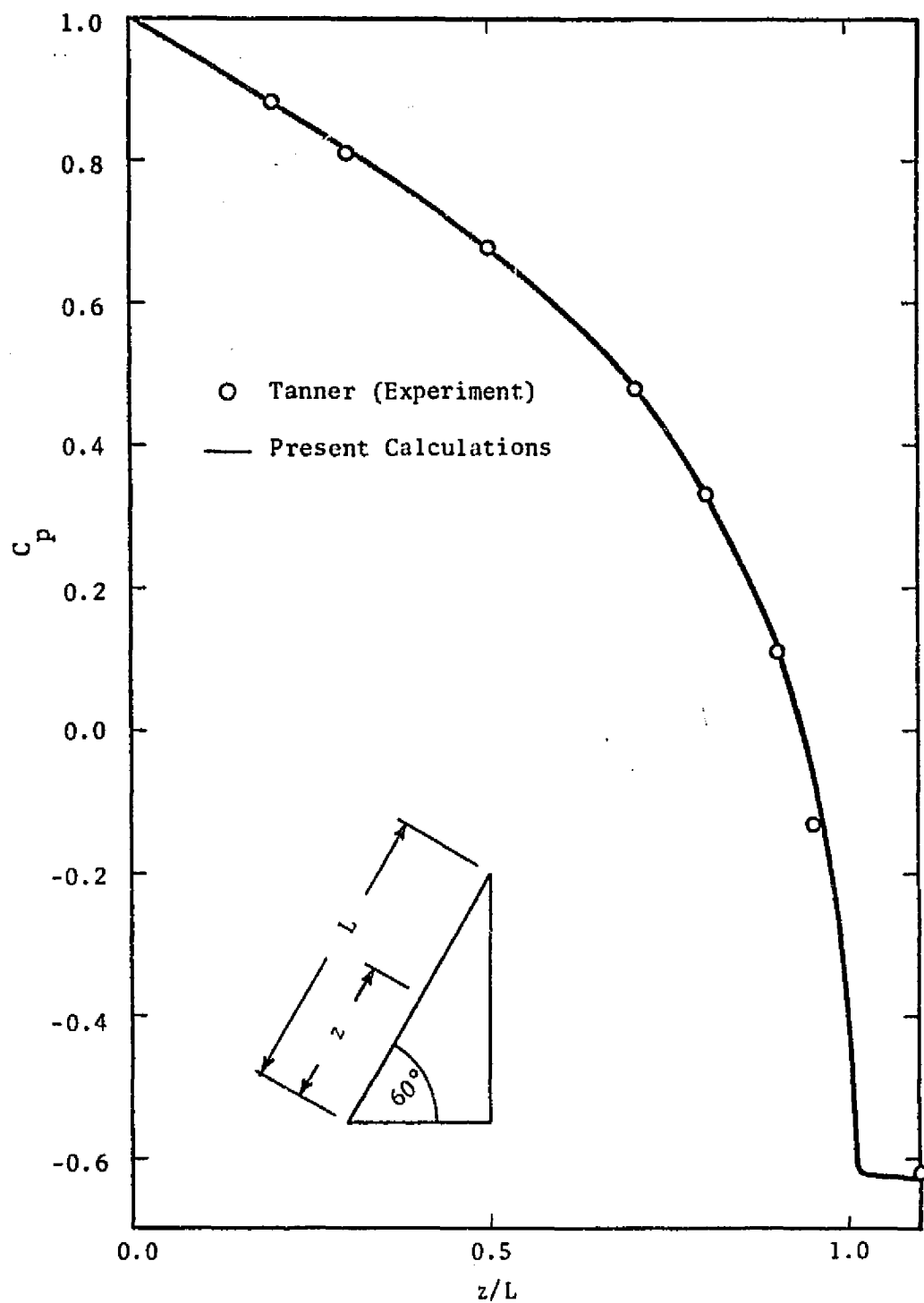


Figure 3.16 Pressure Distribution on the Surface of a 60° Wedge for $\sigma = 10$ and $Re_H = 5 \times 10^4$

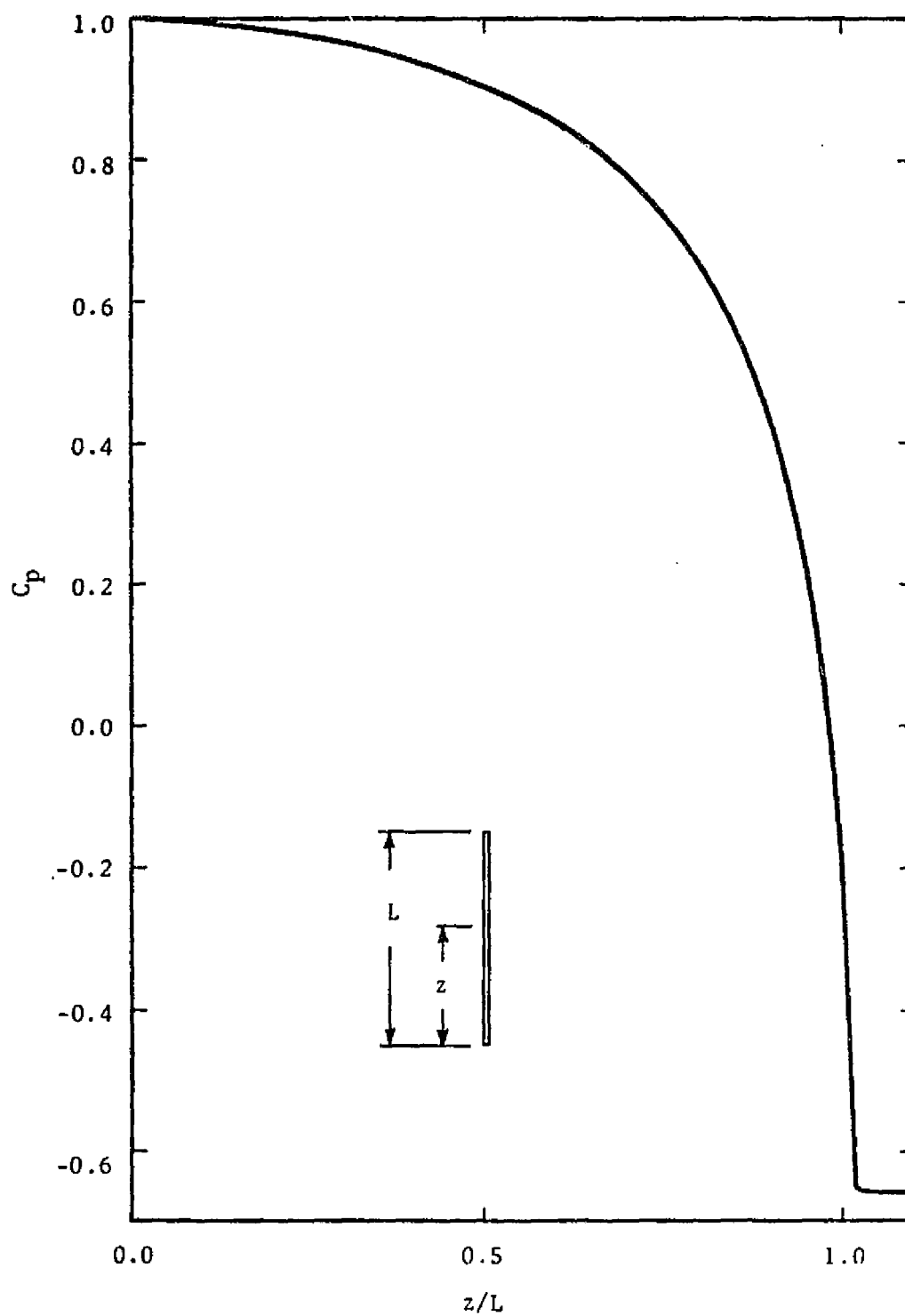


Figure 3.17 Pressure Distribution on the Surface of a 90° Wedge for $\sigma = 9.3$ and $Re_H = 5 \times 10^4$

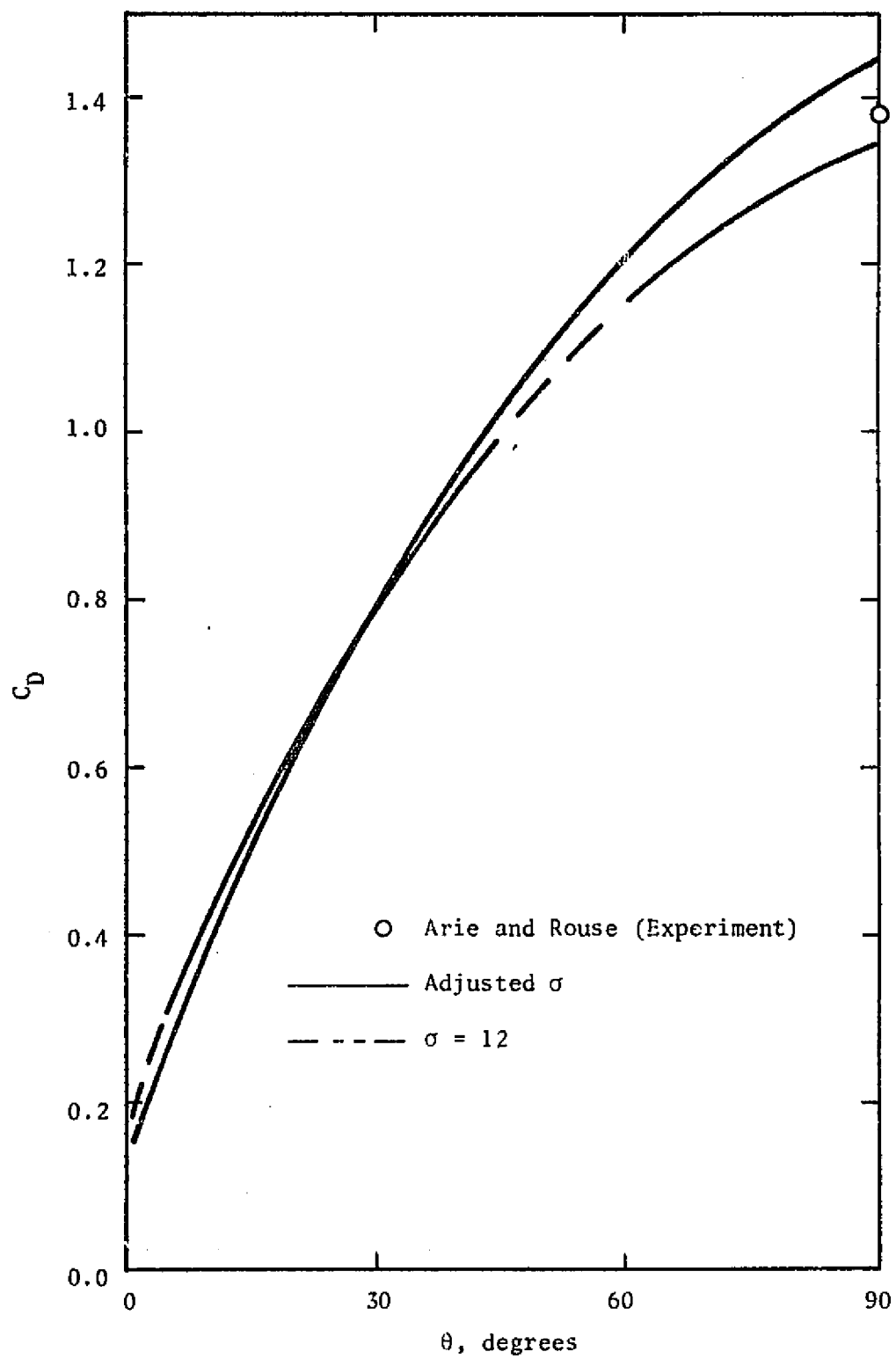


Figure 3.18 Variation of the Drag Coefficient with Wedge Angle for $Re_H = 5 \times 10^4$

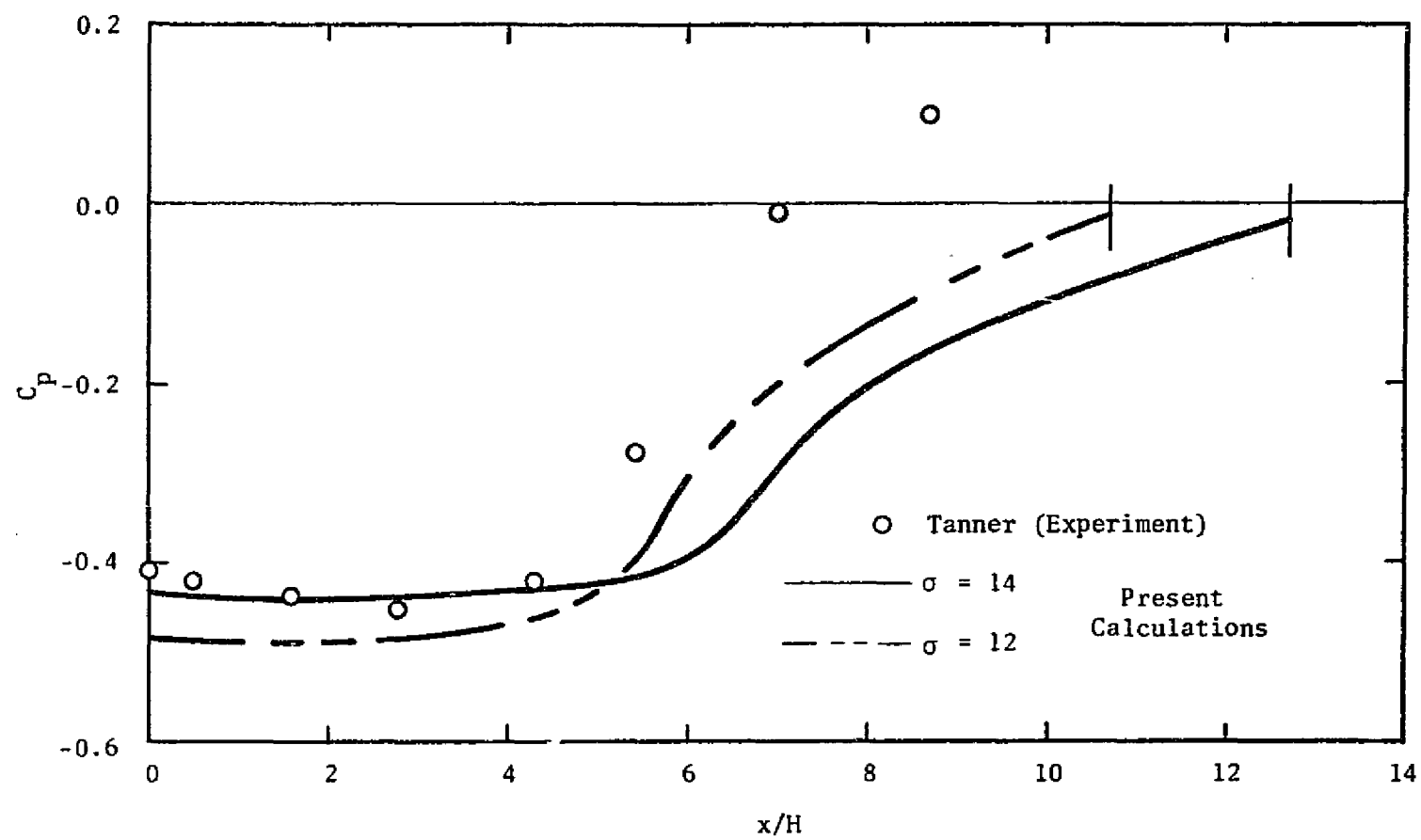


Figure 3.19 Pressure Distribution in the Wake Region for a 15° Wedge at $Re_H = 5 \times 10^4$

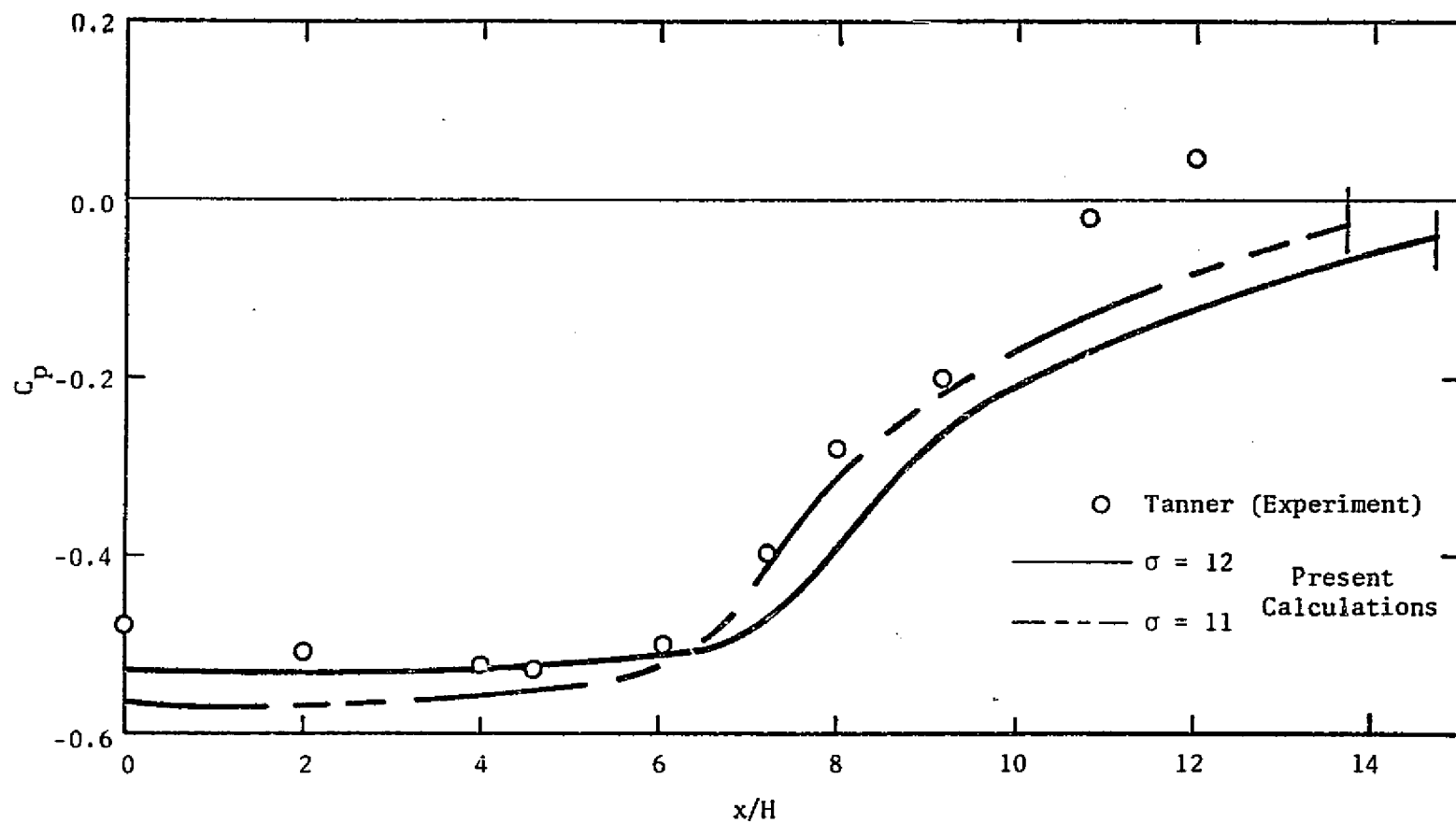


Figure 3.20 Pressure Distribution in the Wake Region for a 30° Wedge at $Re_H = 5 \times 10^4$

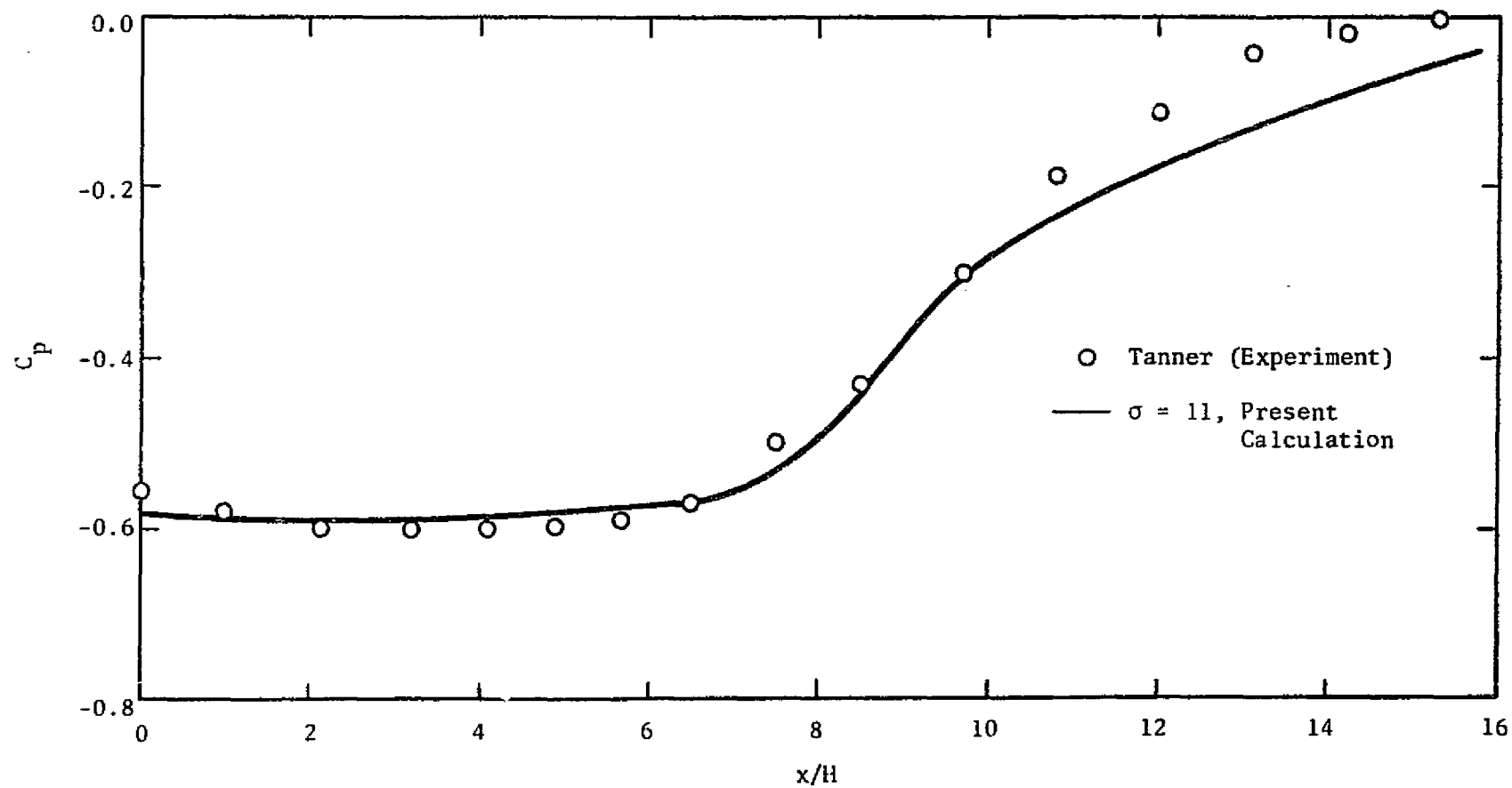


Figure 3.21 Pressure Distribution in the Wake Region for a 45° Wedge at $Re_H = 5 \times 10^4$

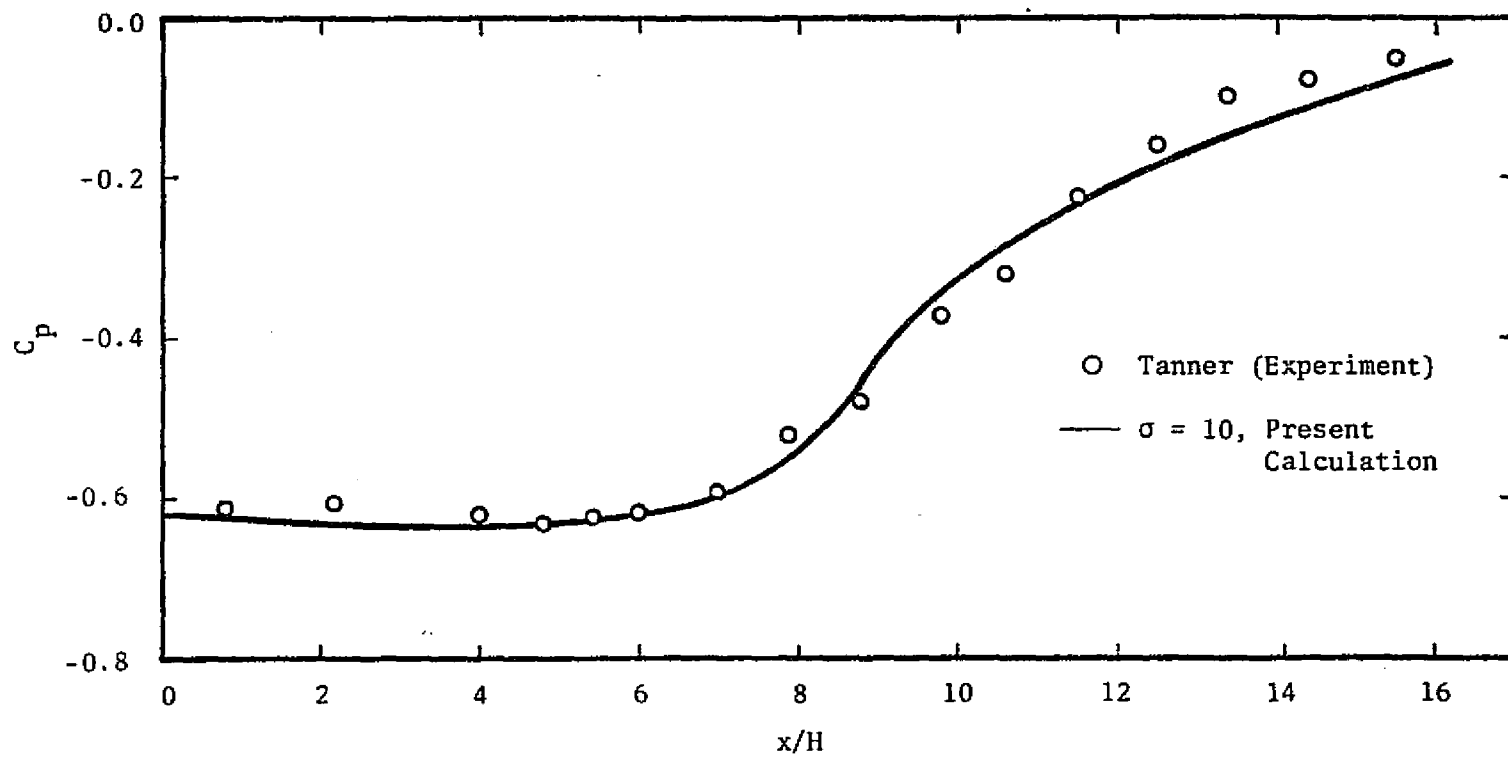


Figure 3.22 Distribution in the Wake Region for a 60° Wedge at $Re_H = 5 \times 10^4$

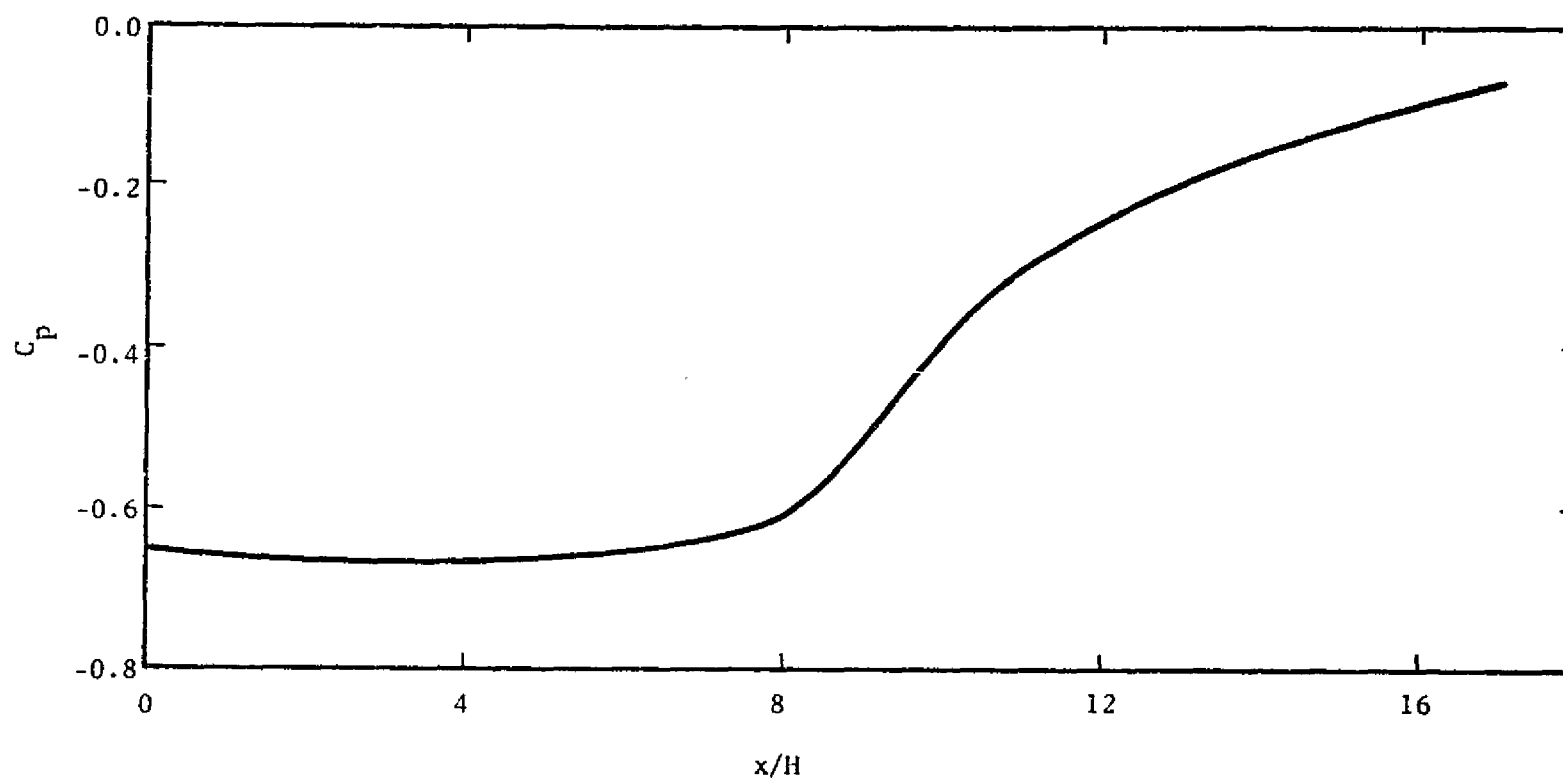


Figure 3.23 Pressure Distribution in the Wake Region for a 90° Wedge with $\sigma = 9.3$ and $Re_H = 5 \times 10^4$

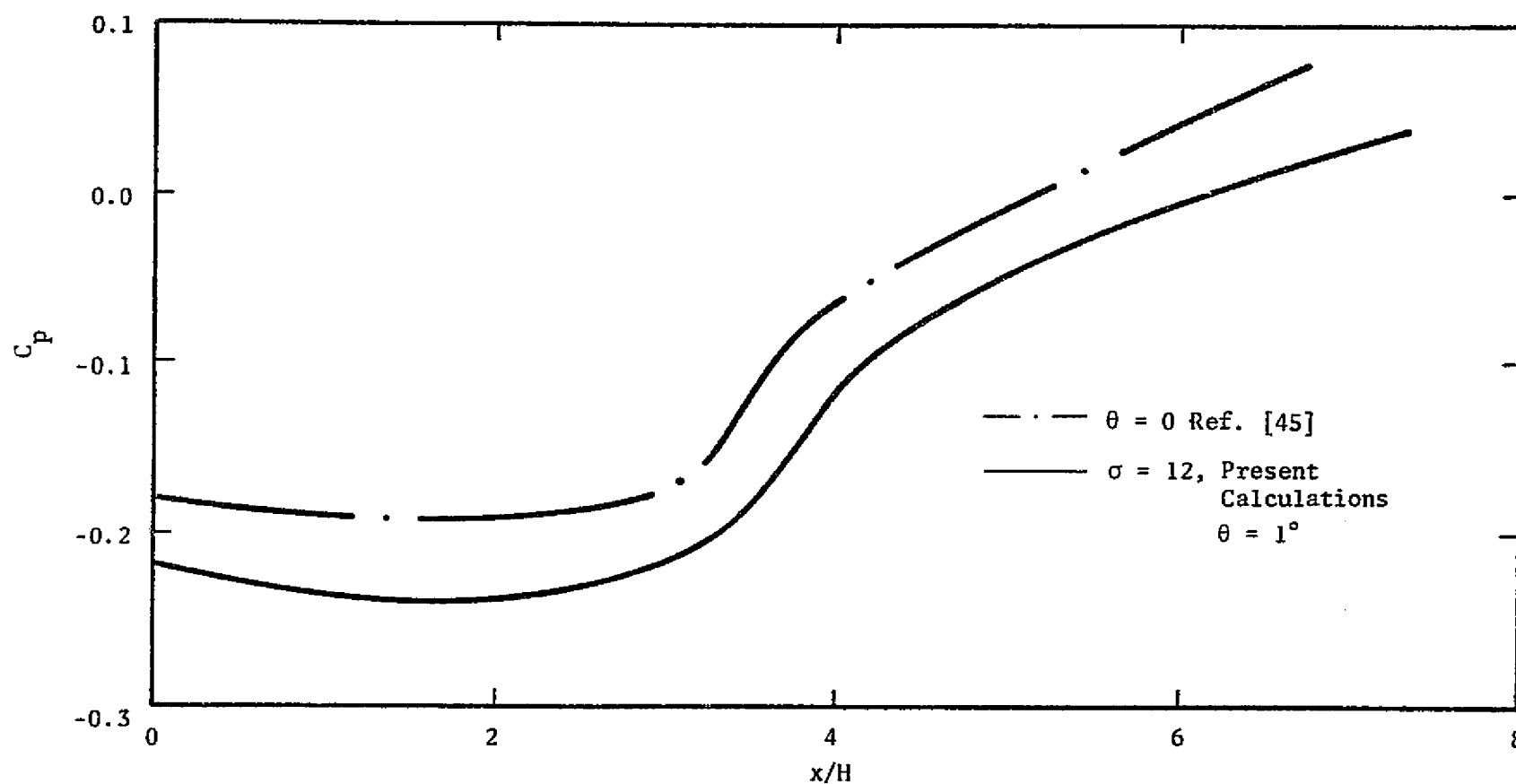


Figure 3.24 Pressure Distribution in the Wake Region for a 1° Wedge at $Re_H = 5 \times 10^4$ compared to Previous Calculations for a Backstep

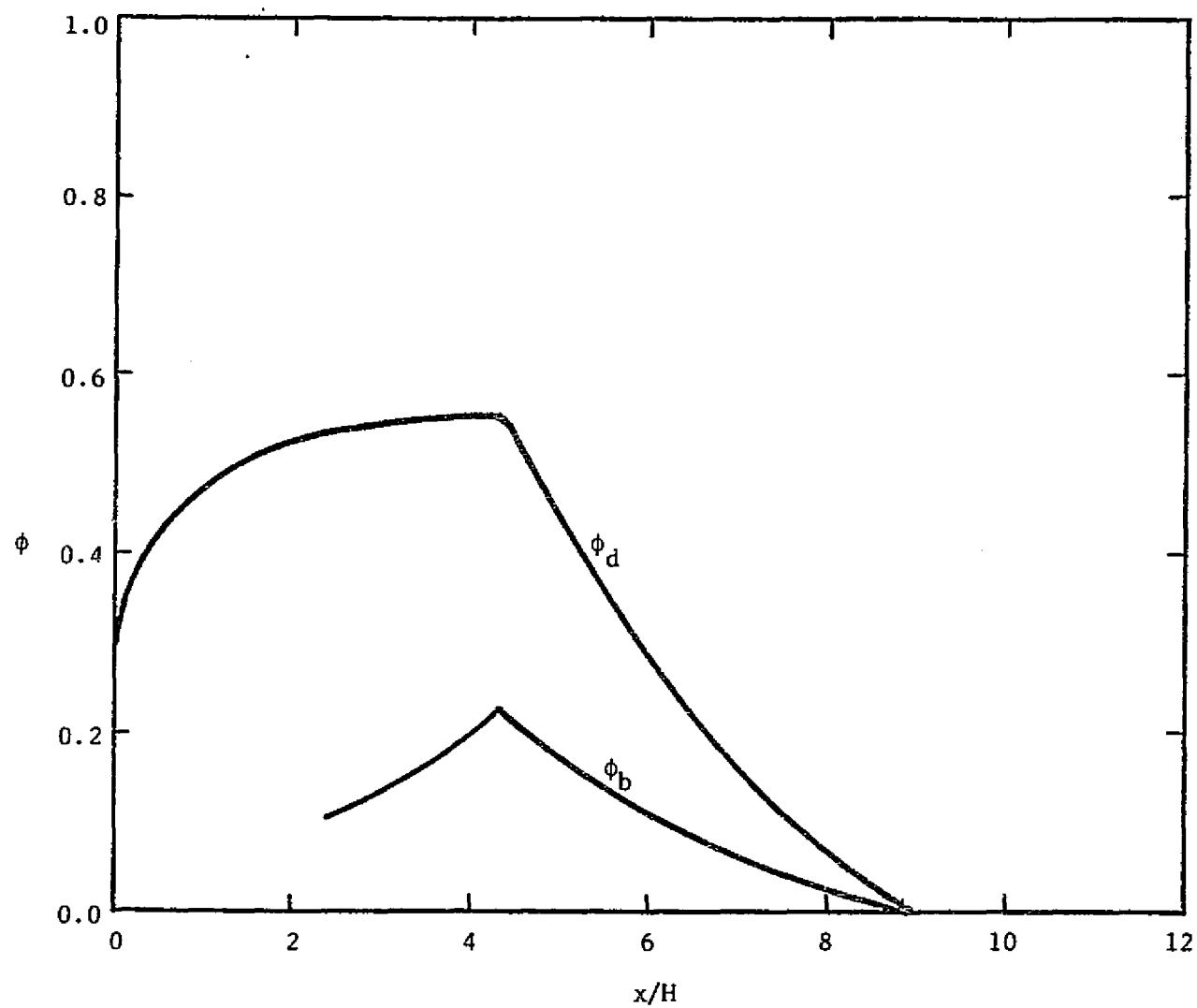


Figure 3.25 Variation of ϕ_d and ϕ_b in the Wake Region for a 5° Wedge with $\sigma = 14$ and $Re_H = 5 \times 10^4$

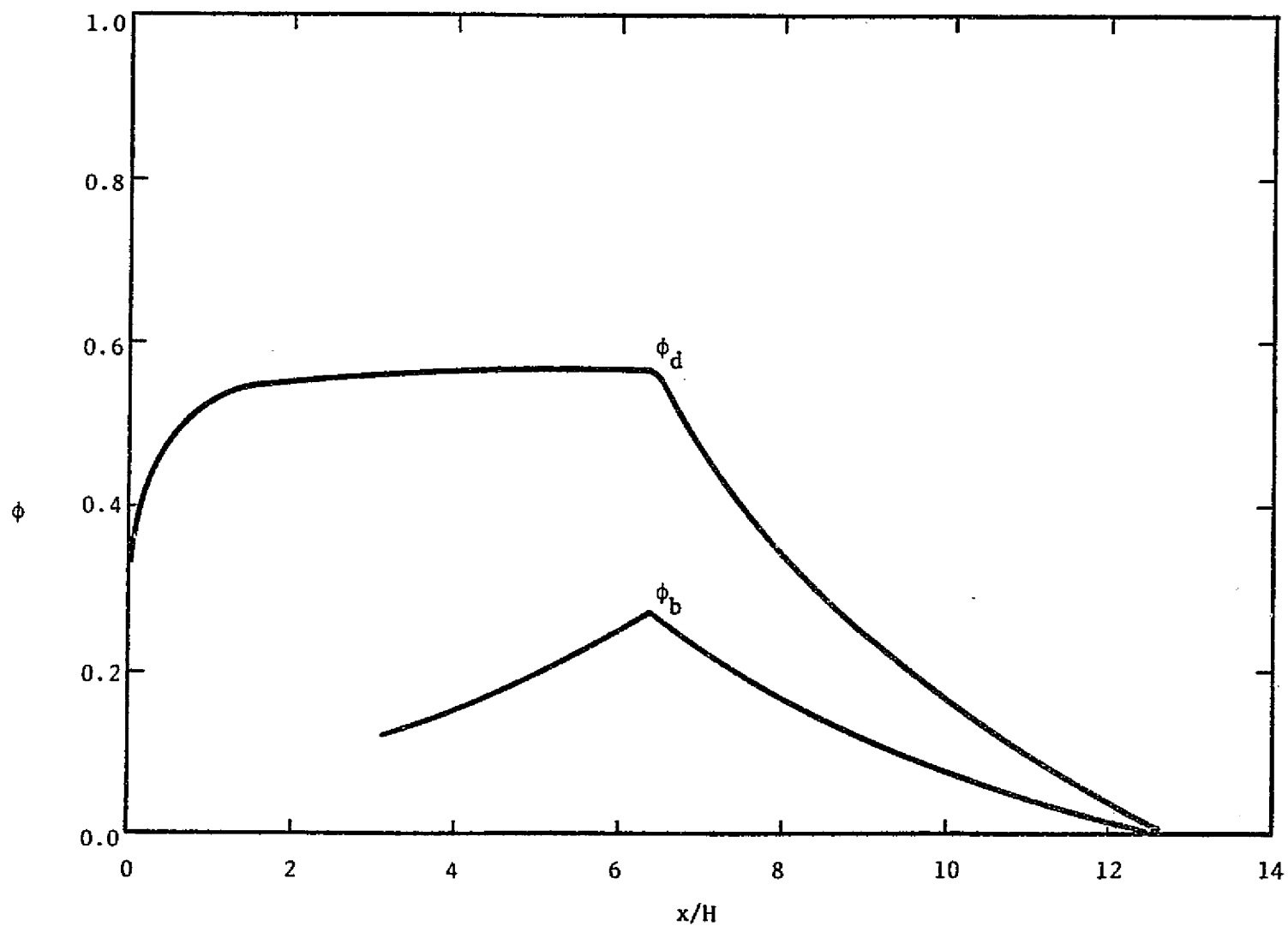


Figure 3.26 Variation of ϕ_d and ϕ_b in the Wake Region for a 15° Wedge with $\sigma = 14$ and $Re_H = 5 \times 10^4$

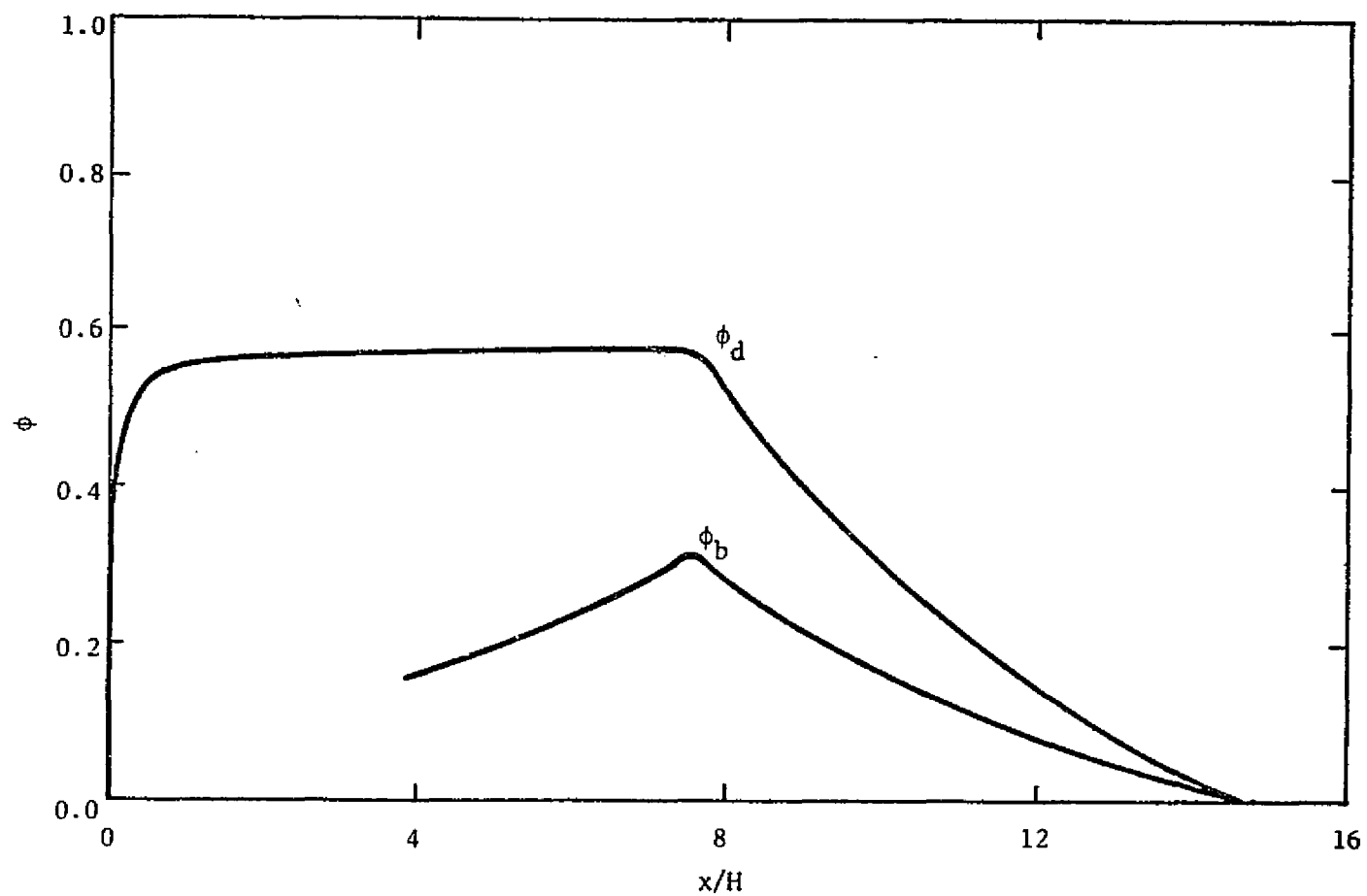


Figure 3.27 Variation of ϕ_d and ϕ_b in the Wake Region for a 30° Wedge
($\sigma = 12$ and $Re_H = 5 \times 10^4$)

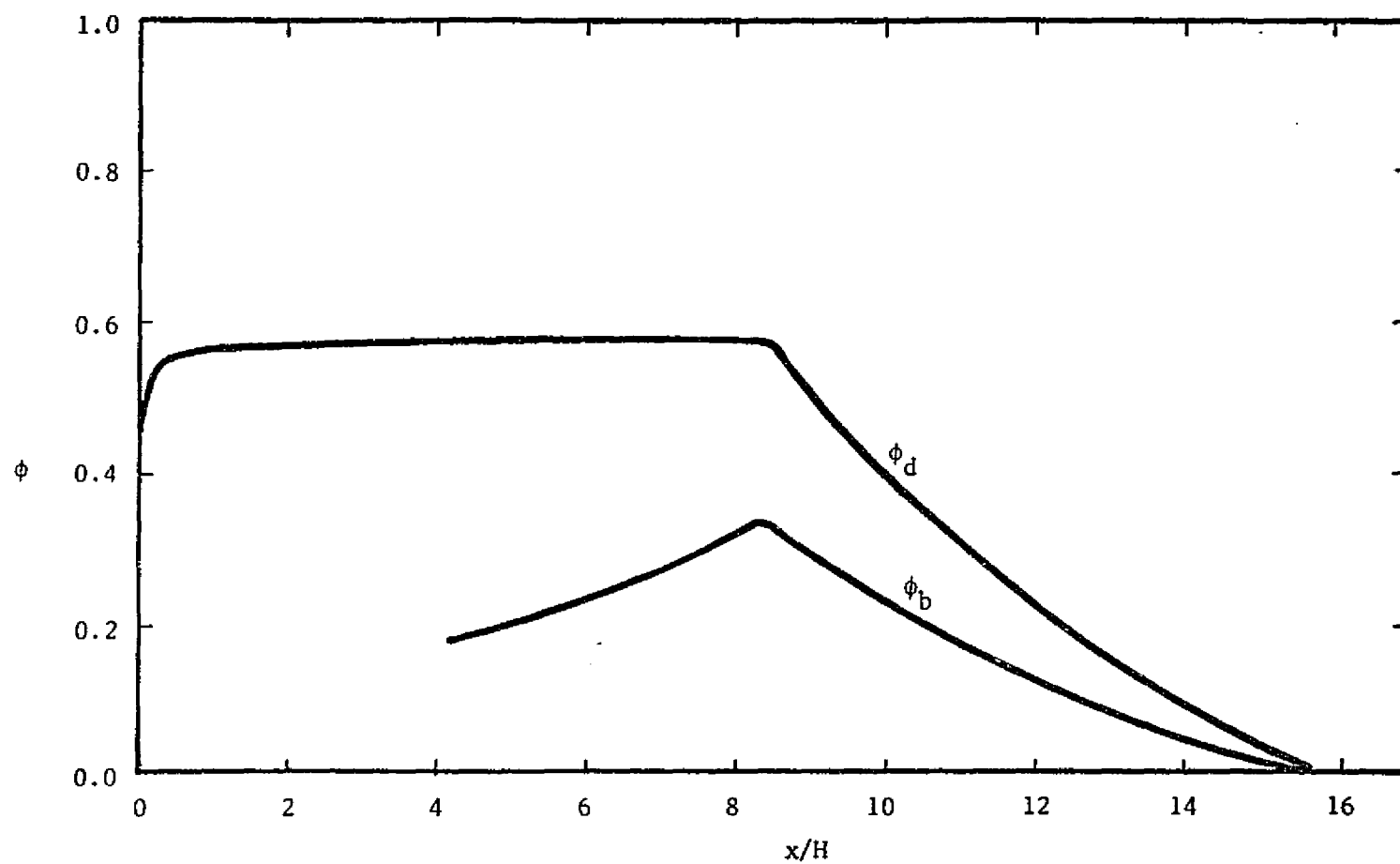


Figure 3.28 Variation of ϕ_d and ϕ_b in the Wake Region for a 60° Wedge with $\sigma = 10$ and $Re_H = 5 \times 10^4$

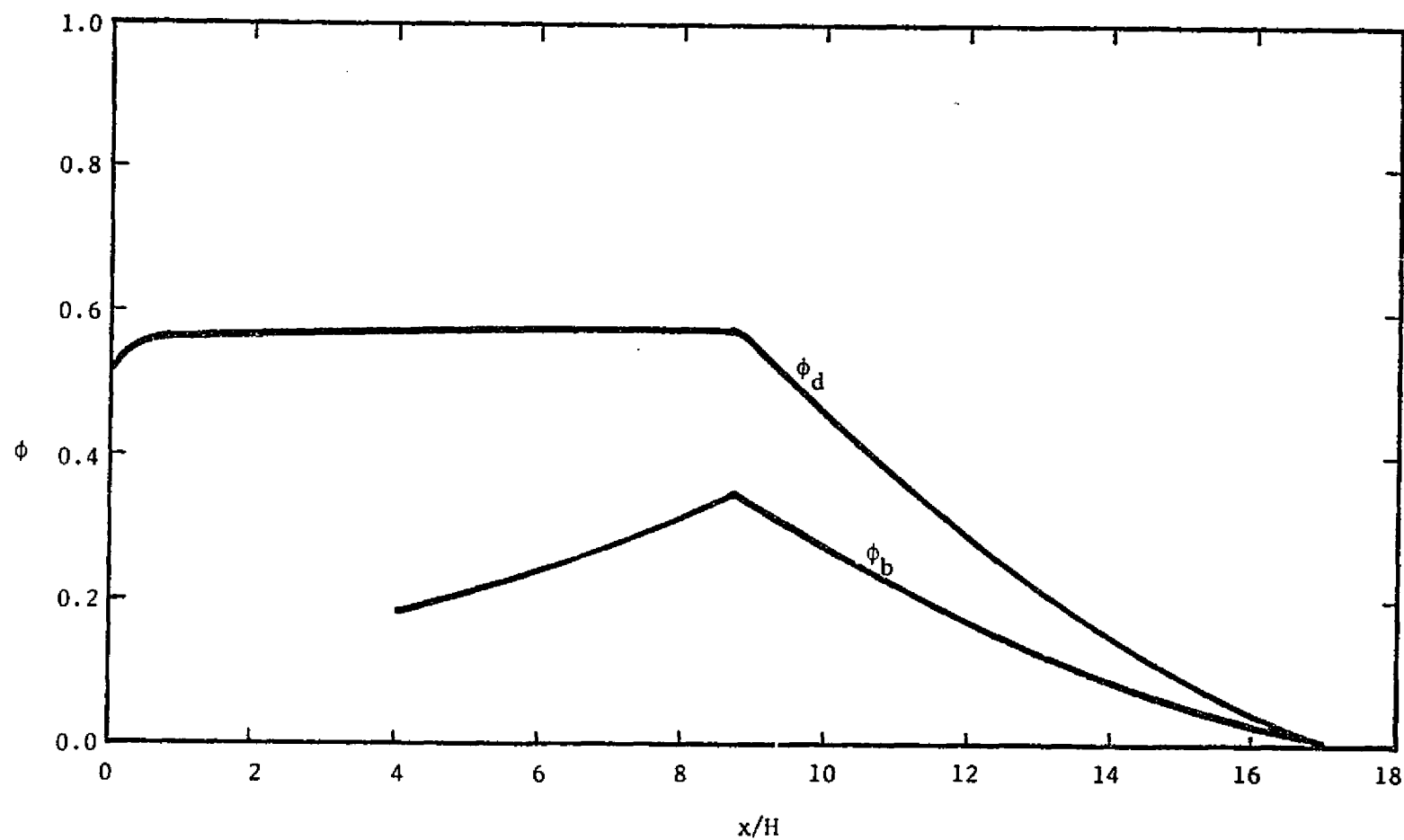


Figure 3.29 Variation of ϕ_d and ϕ_b in the Wake Region for a 90° Wedge with $\sigma = 9.3$ and $Re_H = 5 \times 10^4$

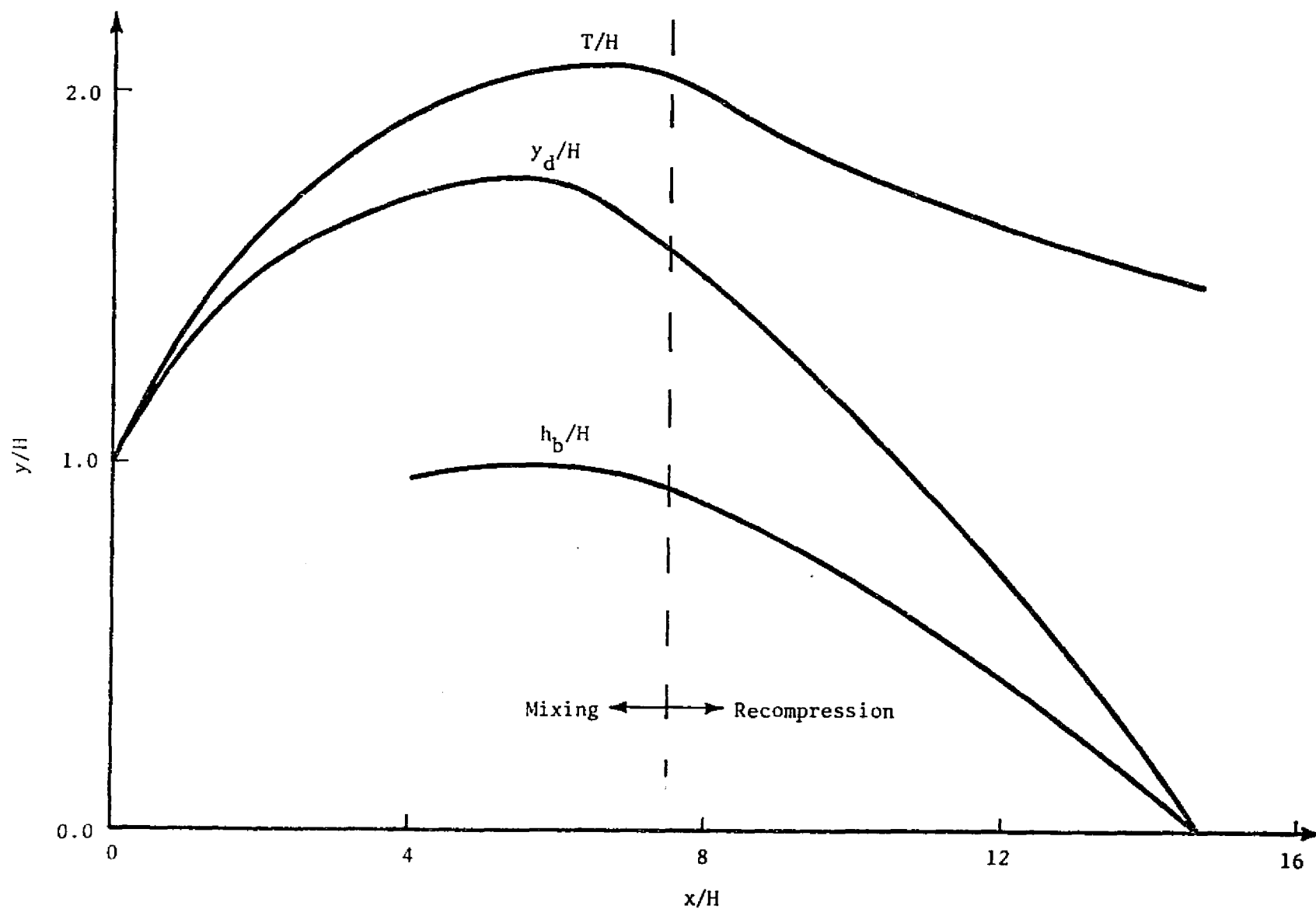


Figure 3.30 Geometry of the Mixing and Recompression Regions for a 30° Wedge with $\sigma = 12$ and $Re_H = 5 \times 10^4$

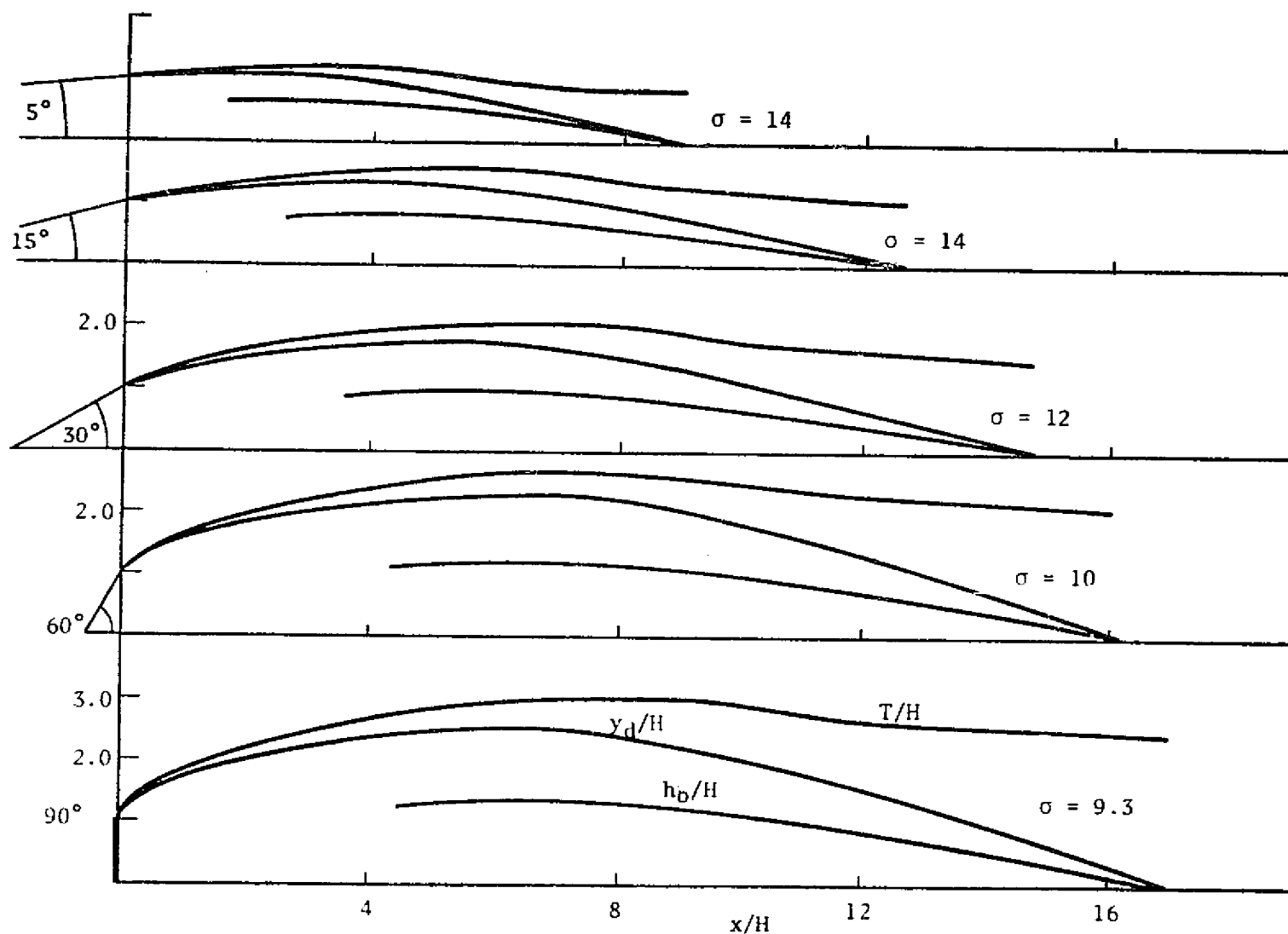


Figure 3.31 Comparison of Wake Dimensions for $Re_H = 5 \times 10^4$

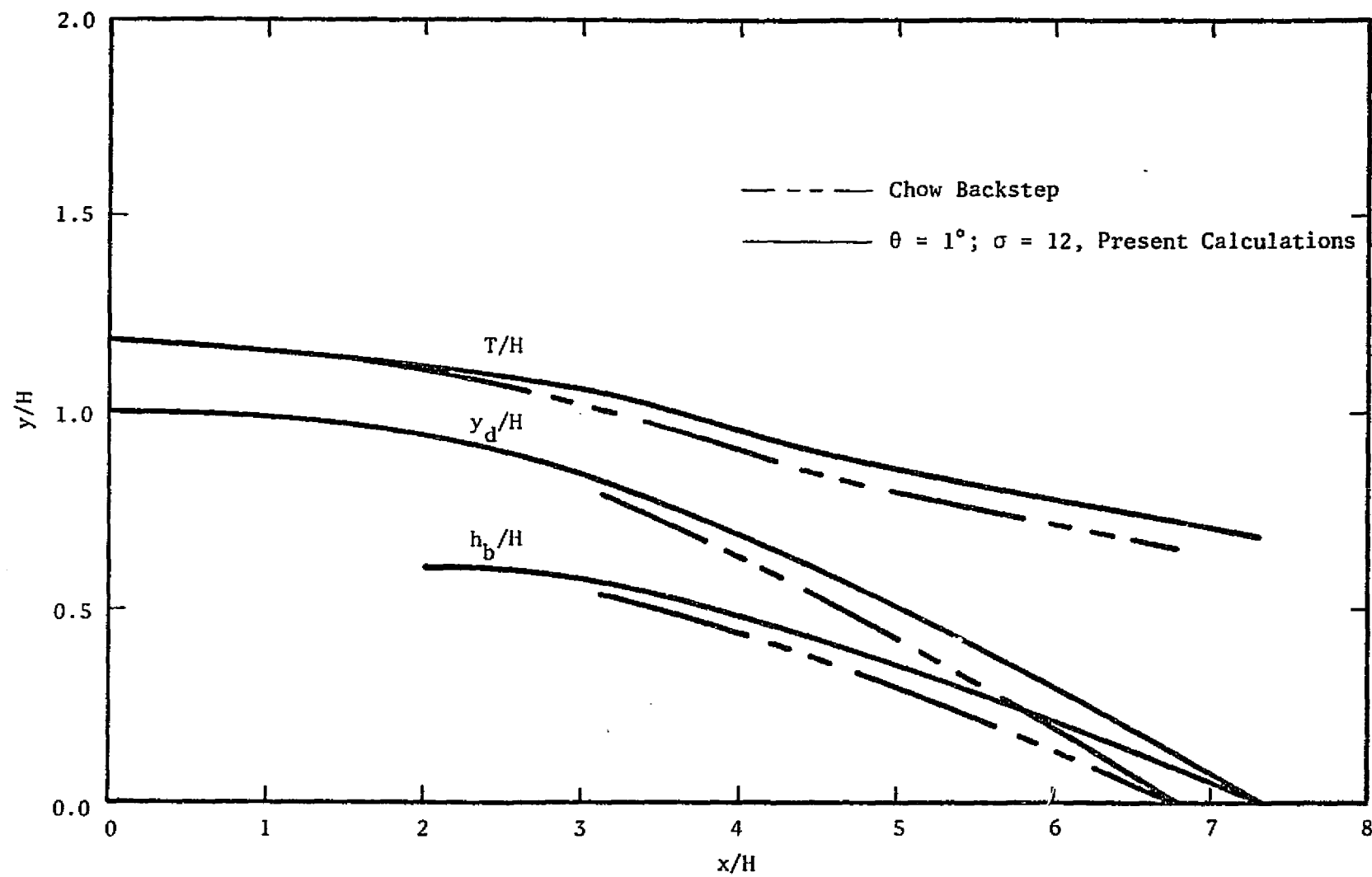


Figure 3.32 Comparison of Wake Geometries for a 1° Wedge and a Backstep as Calculated by Chow

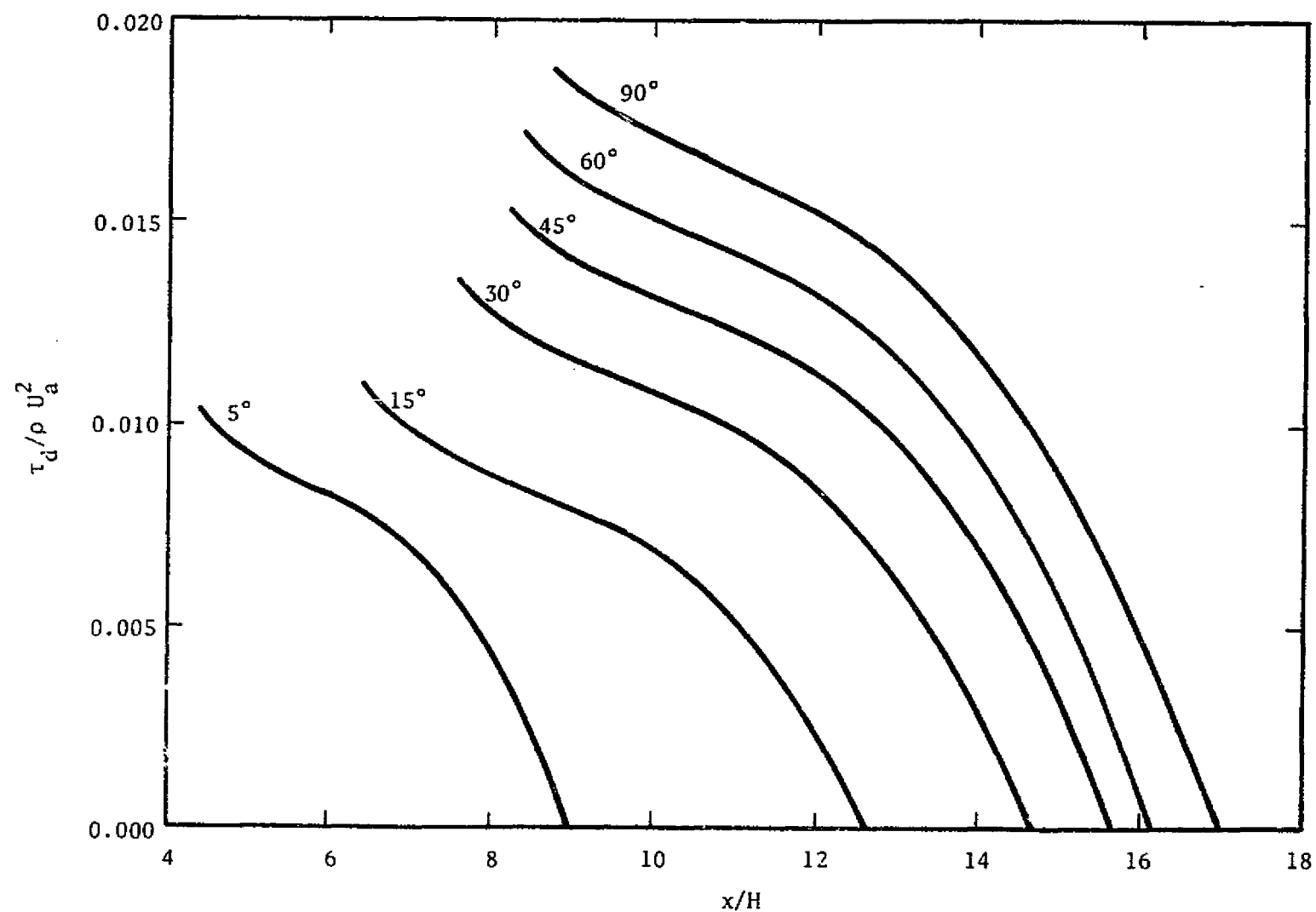


Figure 3.33 Shear Stress along the Dividing Streamline in the Recompression Region using the Adjusted σ Values and $Re_H = 5 \times 10^4$

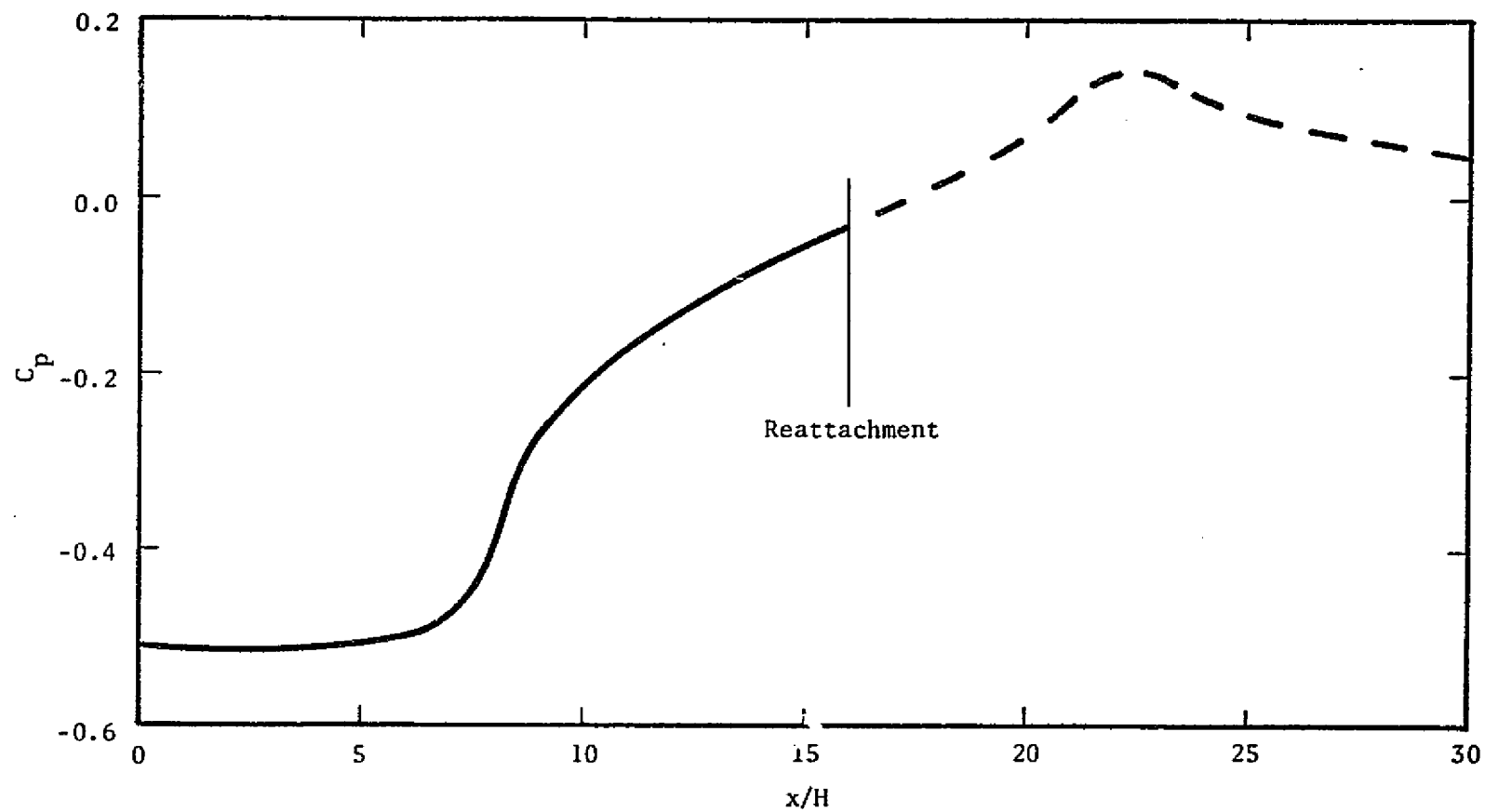


Figure 3.34 Pressure Distribution for a 30° Wedge with the Redevelopment Pressure evaluated by Streamline Tracing

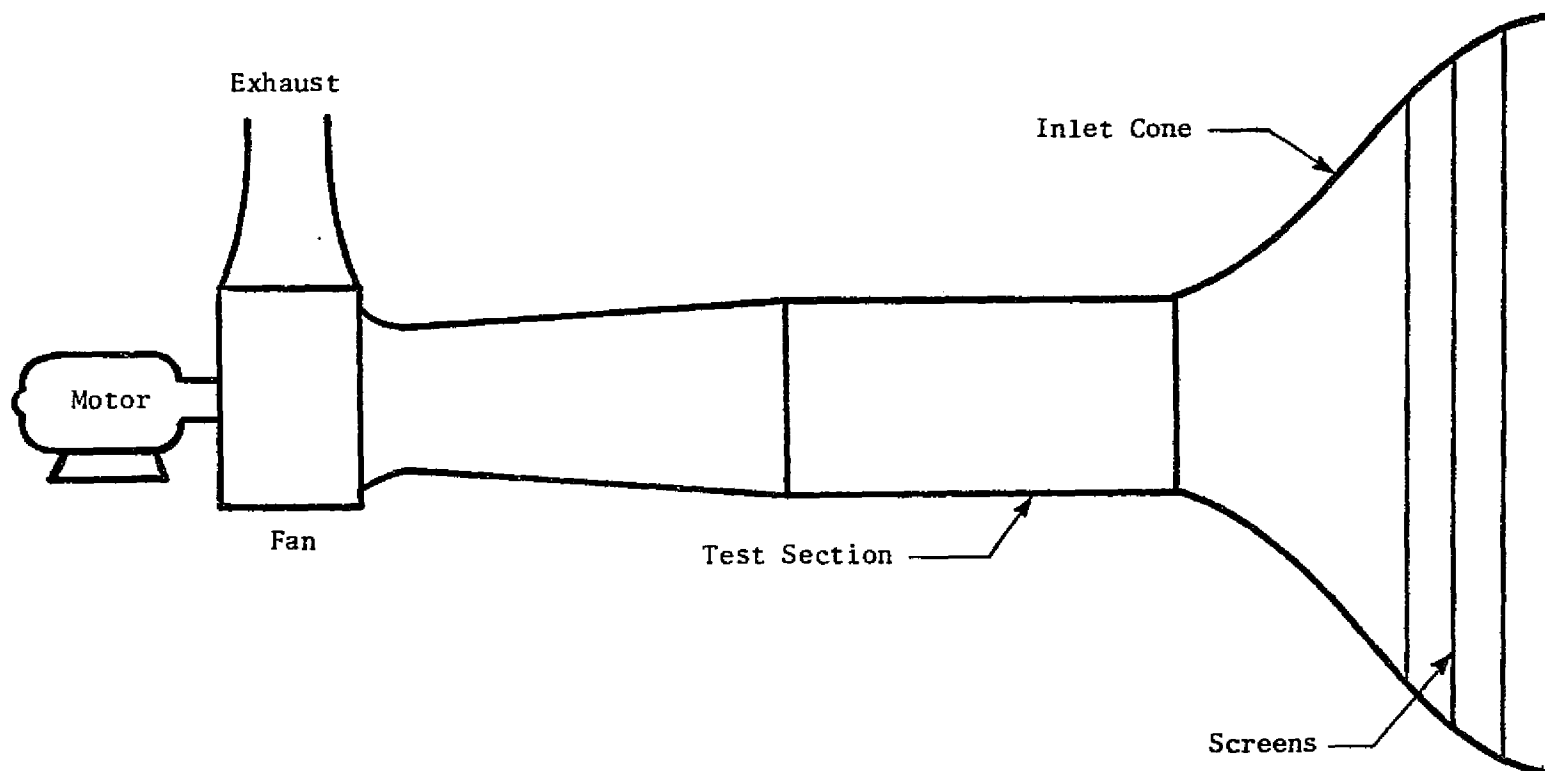


Figure 4.1 Wind Tunnel

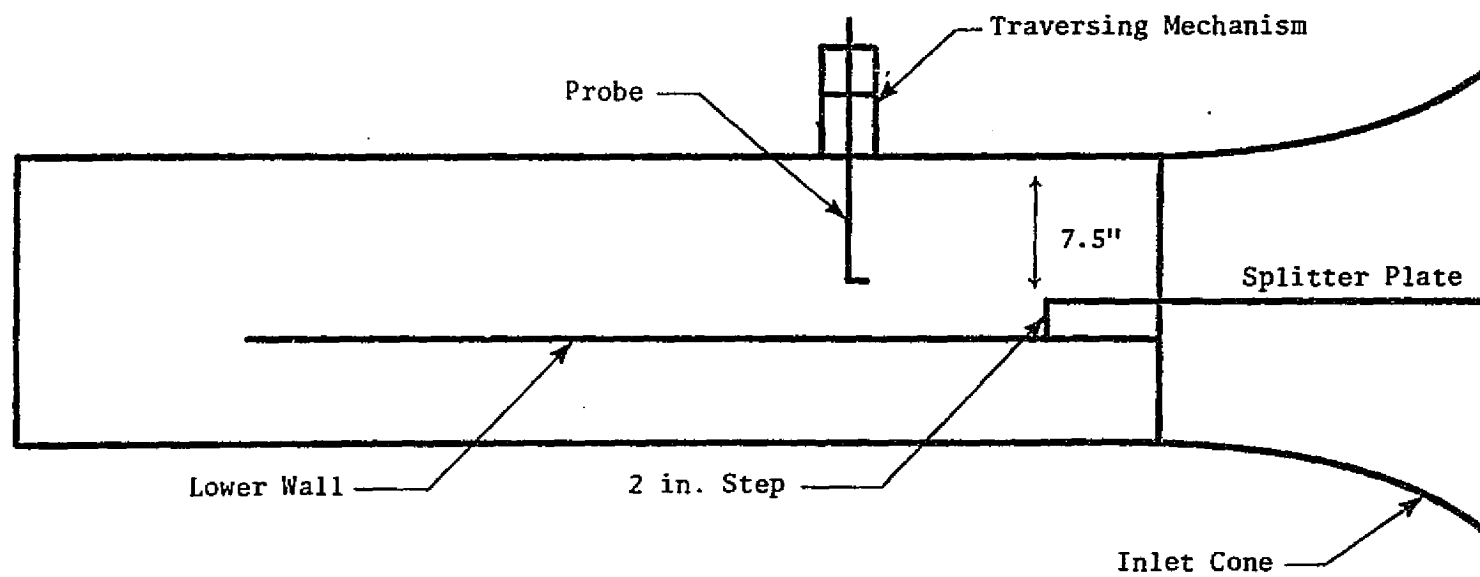
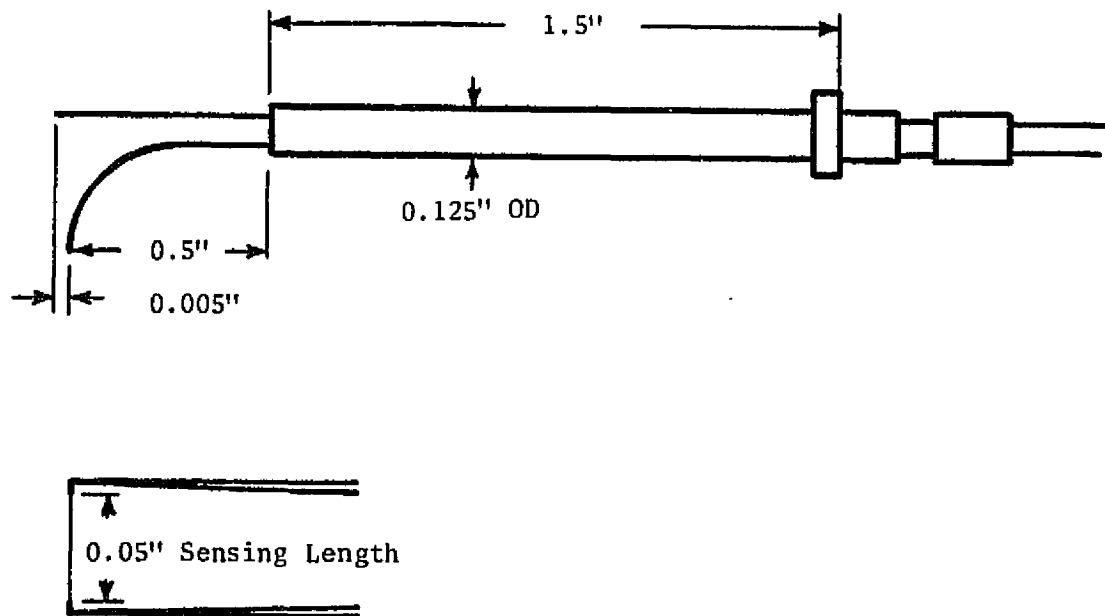
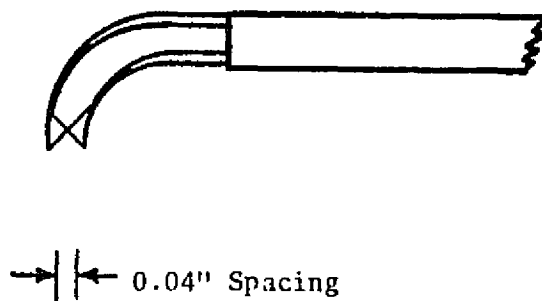


Figure 4.2 Test Section



(a) Boundary Layer Probe



(b) x-Wire Probe

Figure 4.3 Hot Wire Probes

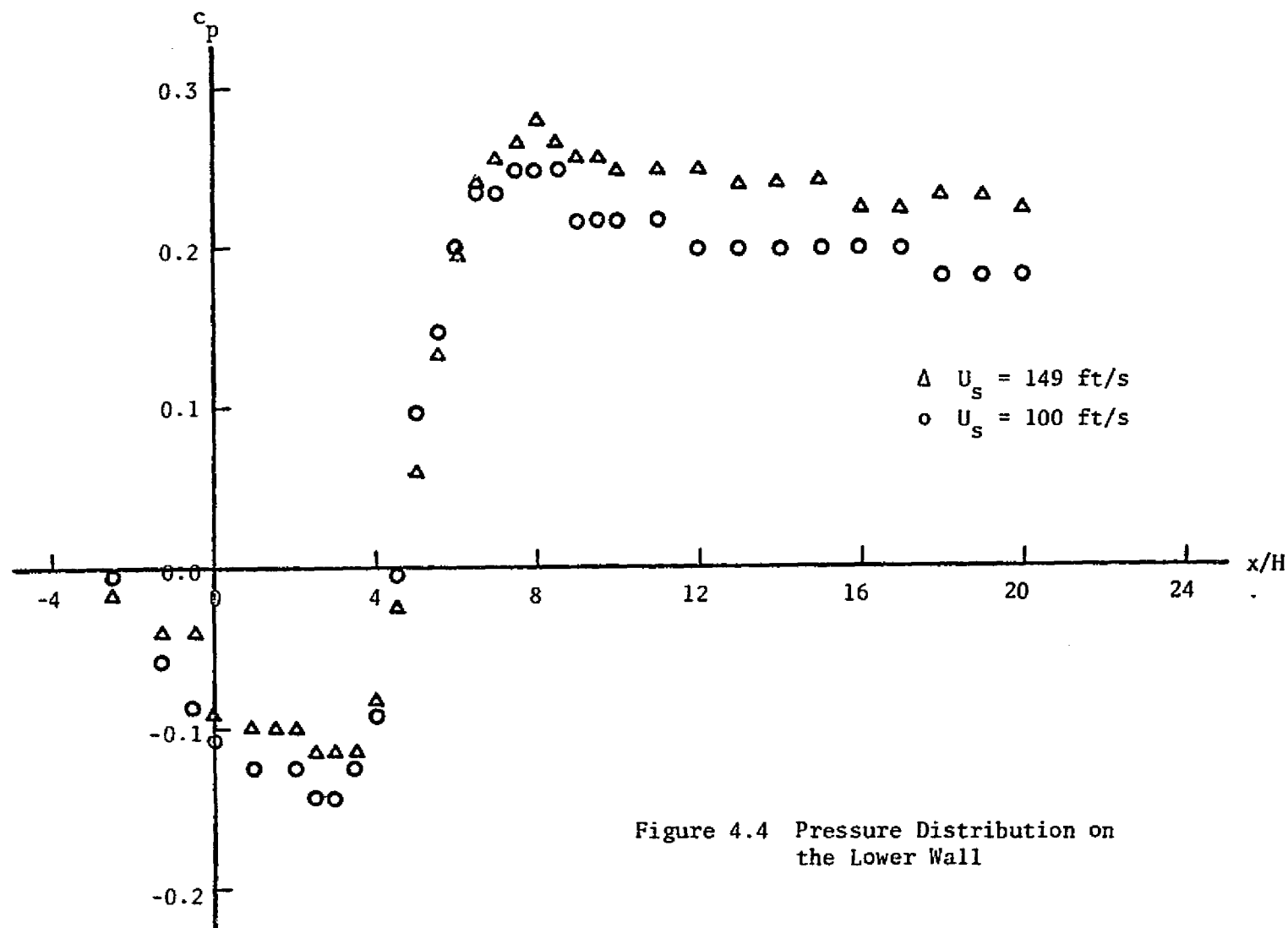


Figure 4.4 Pressure Distribution on the Lower Wall

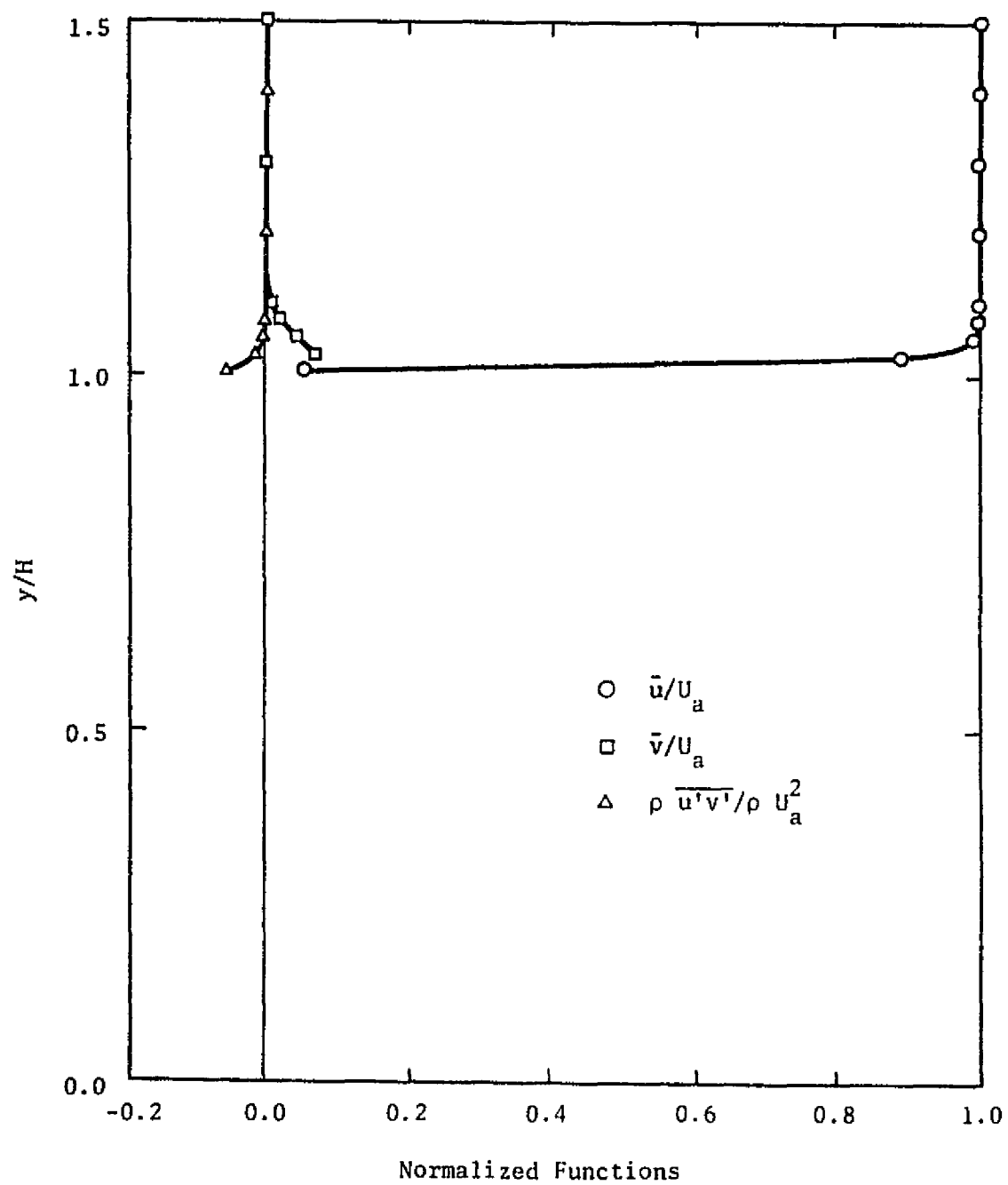


Figure 4.5 Velocity and Reynolds Stress Distributions
at $x/H = 0.0$

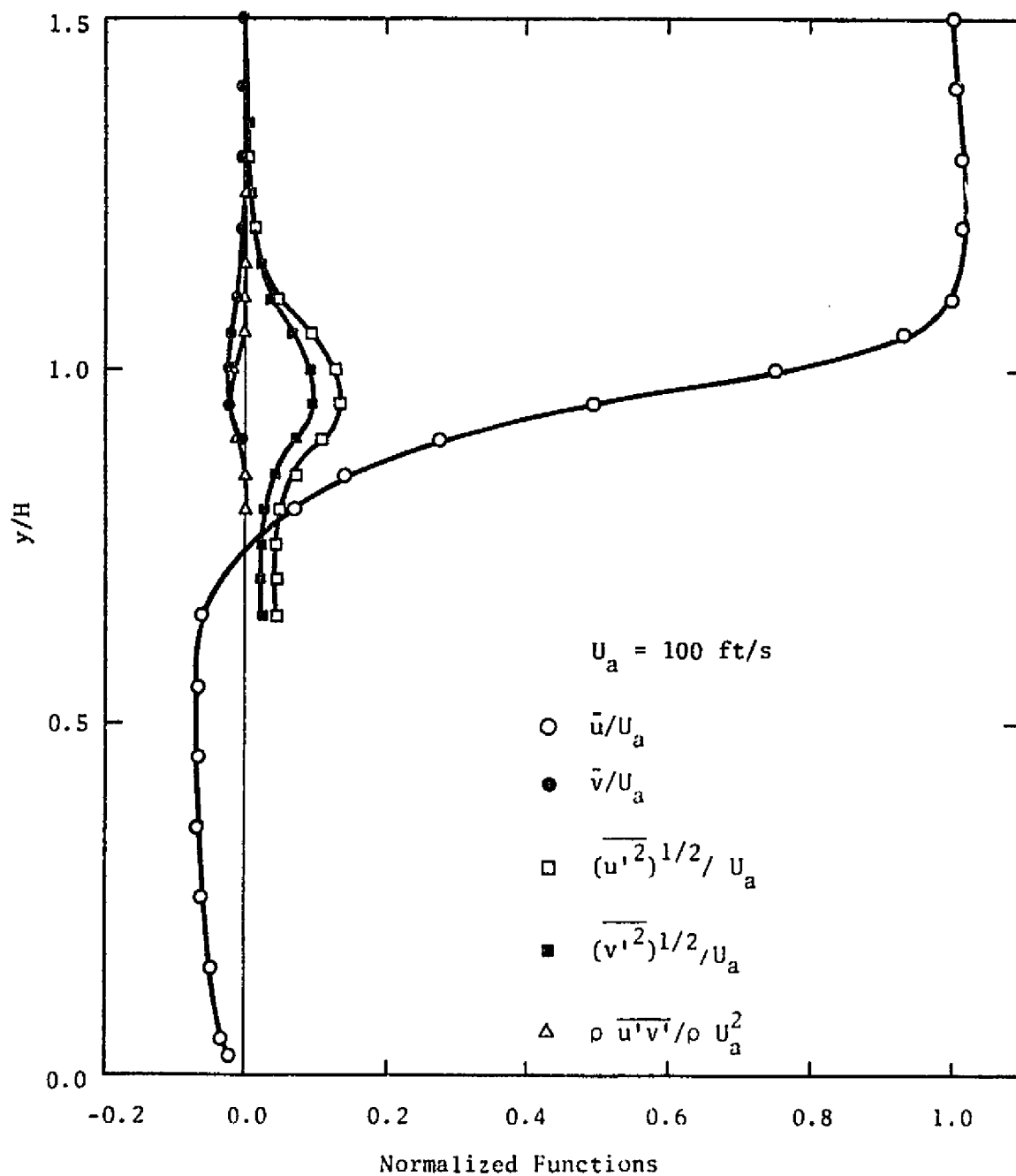


Figure 4.6 Velocity and Reynolds Stress Distributions
at $x/l = 1.0$

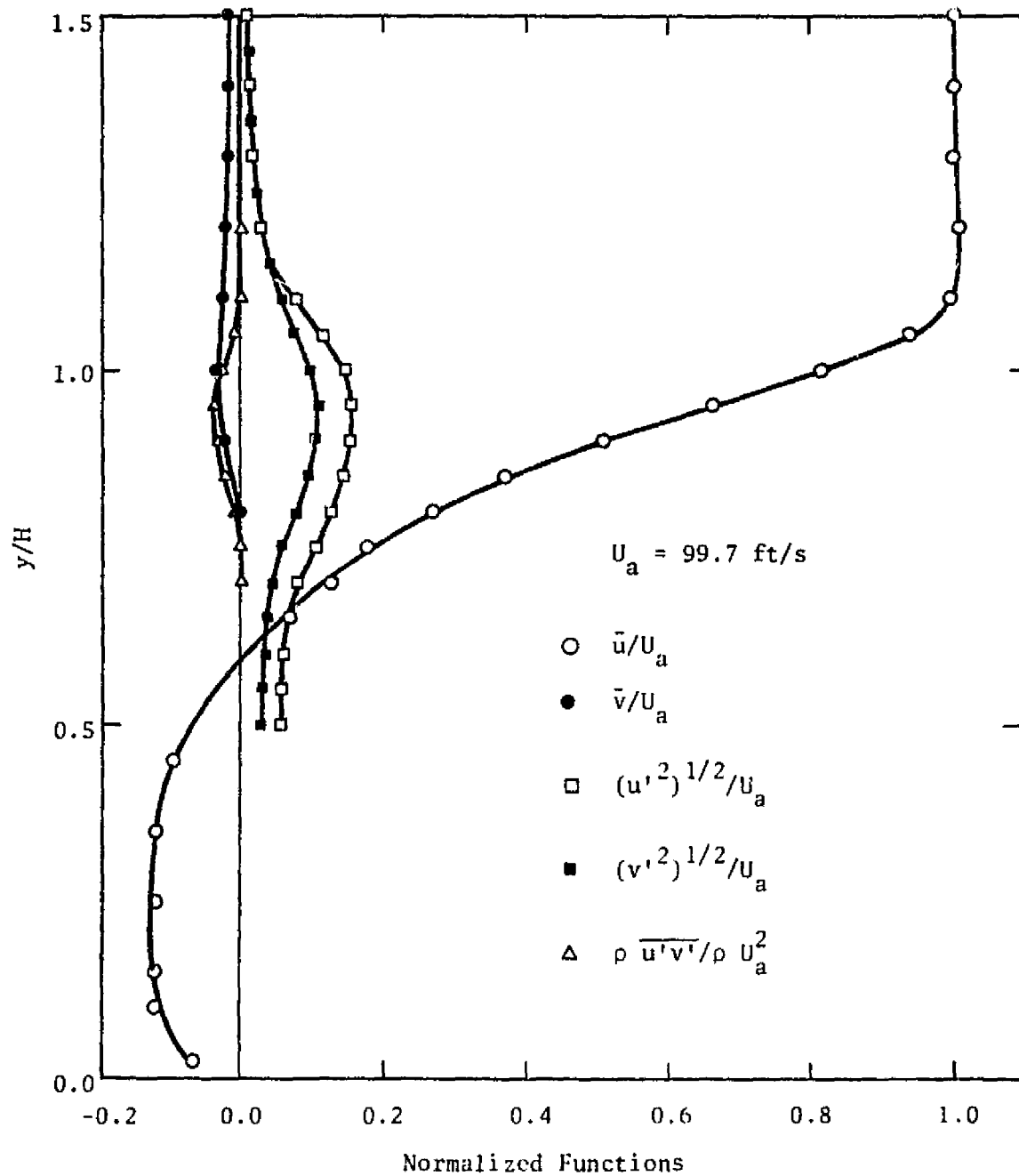


Figure 4.7 Velocity and Reynolds Stress Distributions
at $x/H = 2.0$

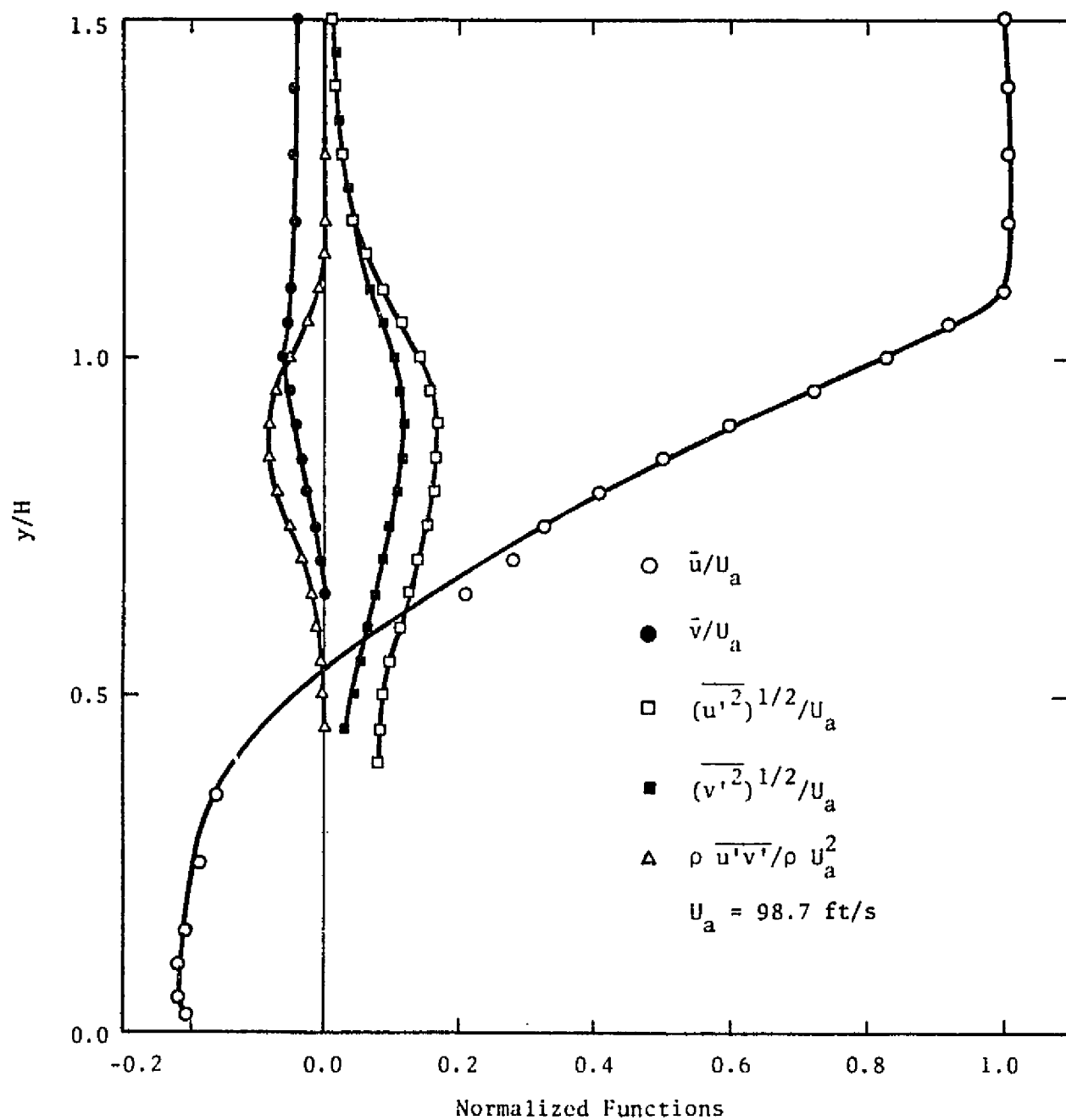


Figure 4.8 Velocity and Reynolds Stress Distributions at $x/H = 3.0$

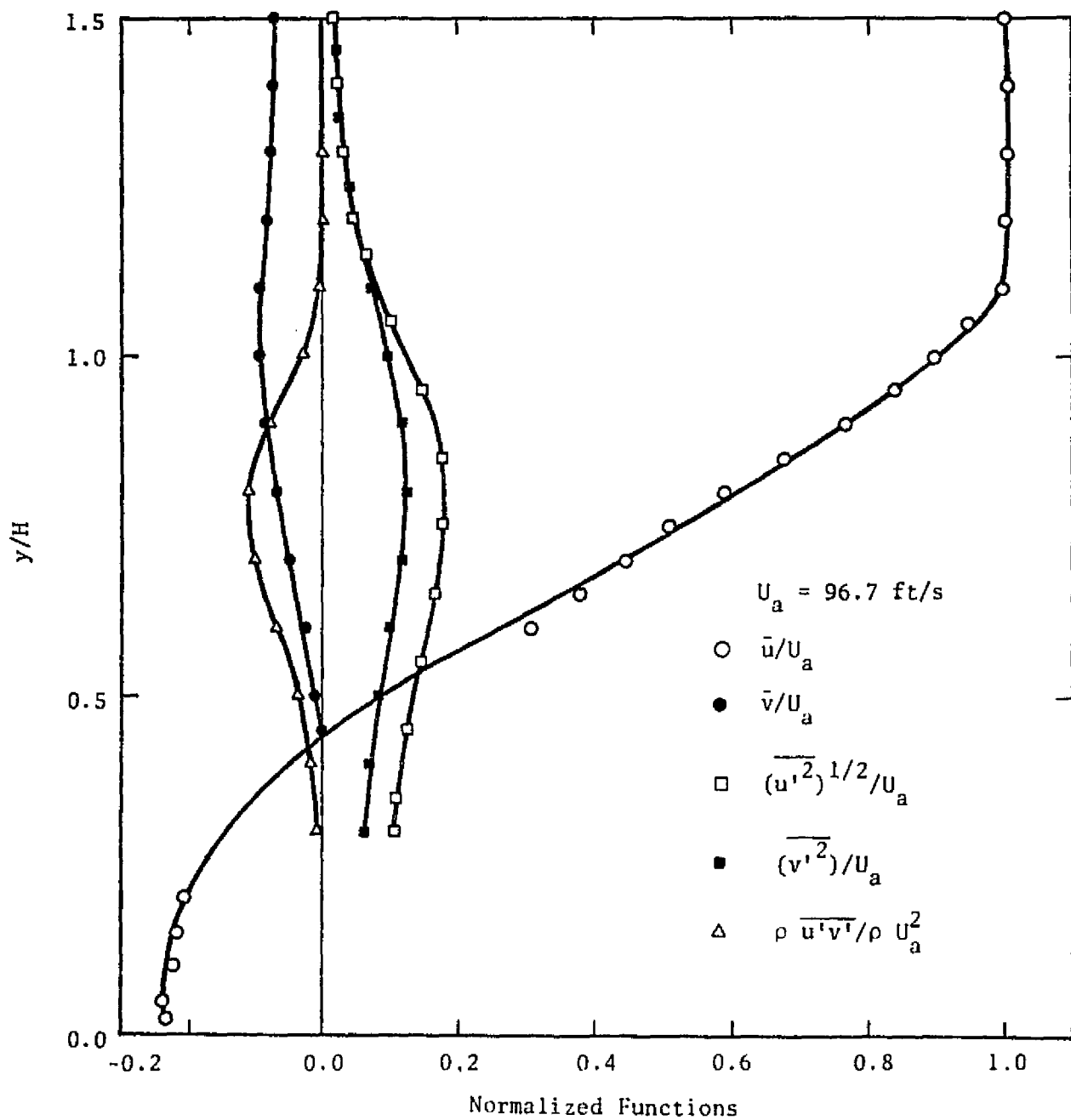


Figure 4.9 Velocity and Reynolds Stress Distributions
at $x/H = 4.0$

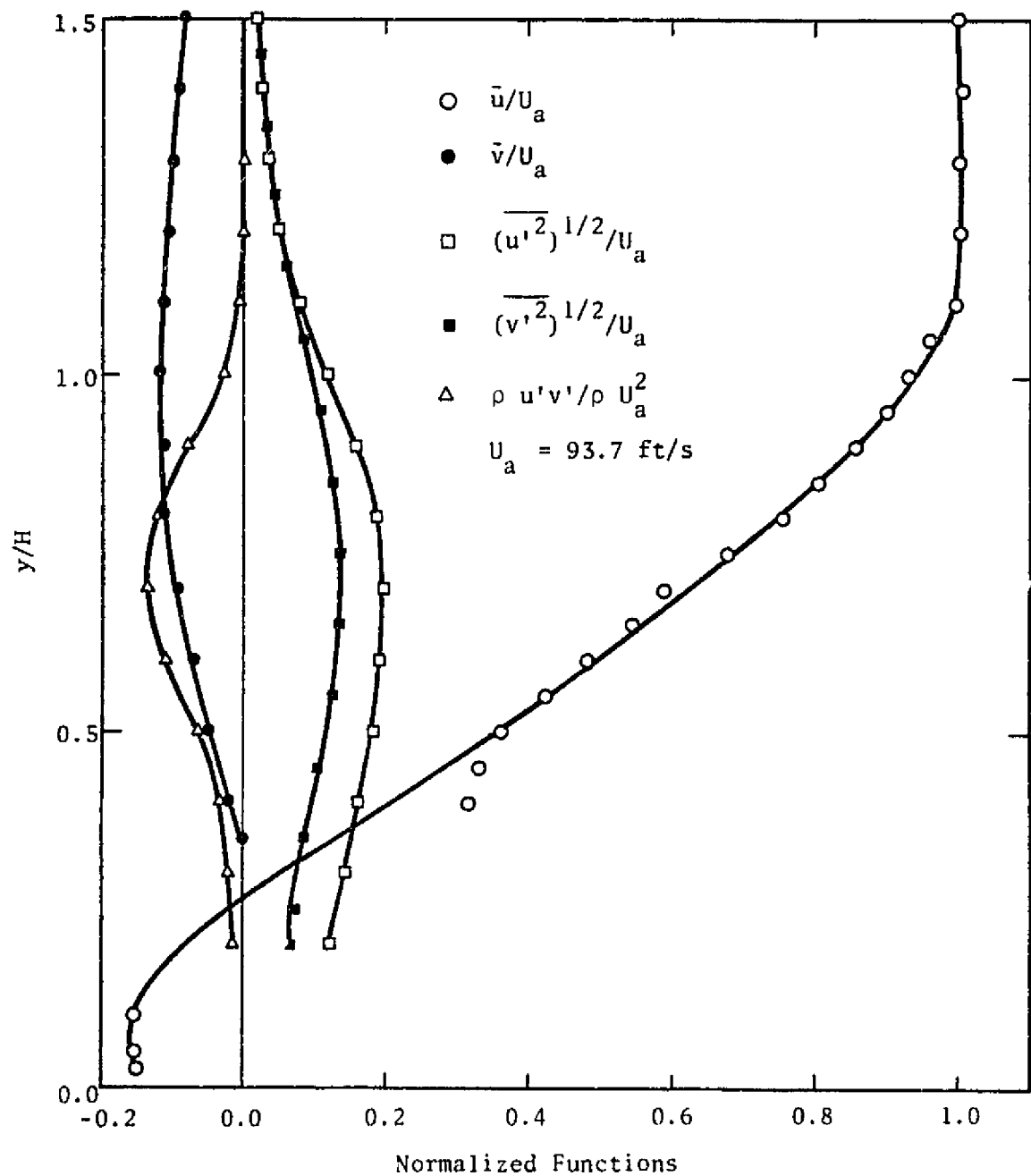


Figure 4.10 Velocity and Reynolds Stress Distributions at $x/H = 5.0$

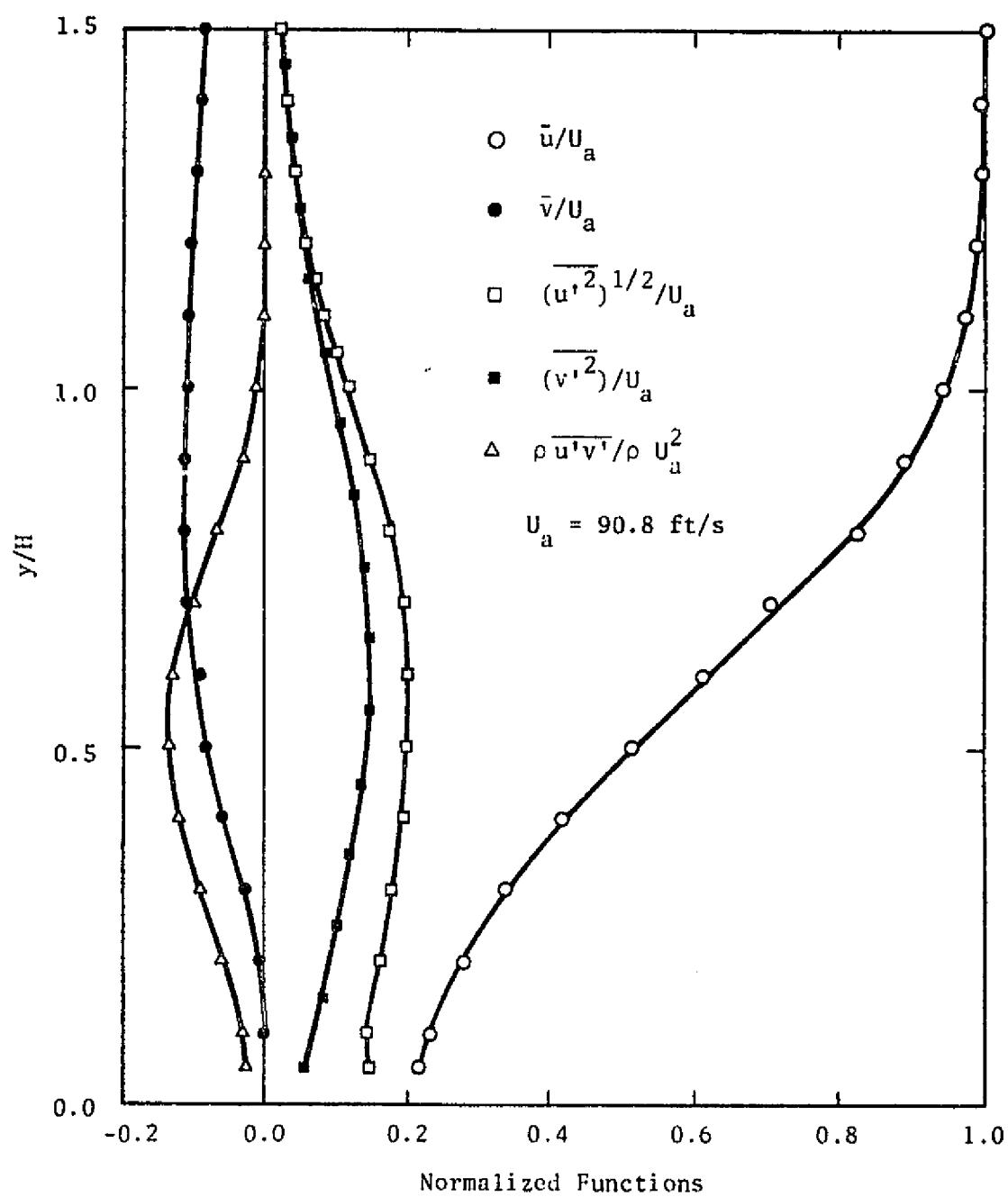


Figure 4.11 Velocity and Reynolds Stress Distributions at $x/H = 6.0$

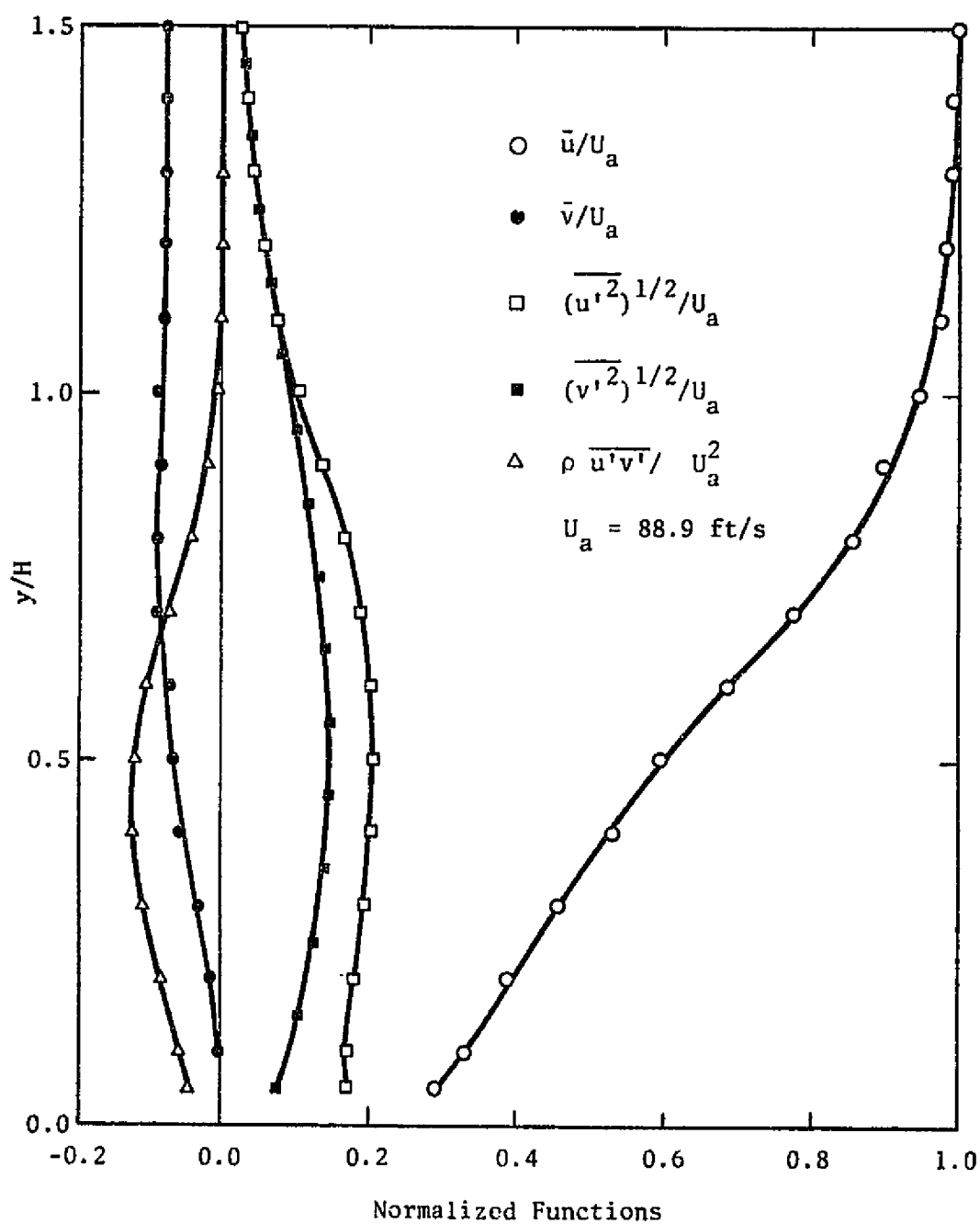


Figure 4.12 Velocity and Reynolds Stress Distributions at $x/H = 7.0$

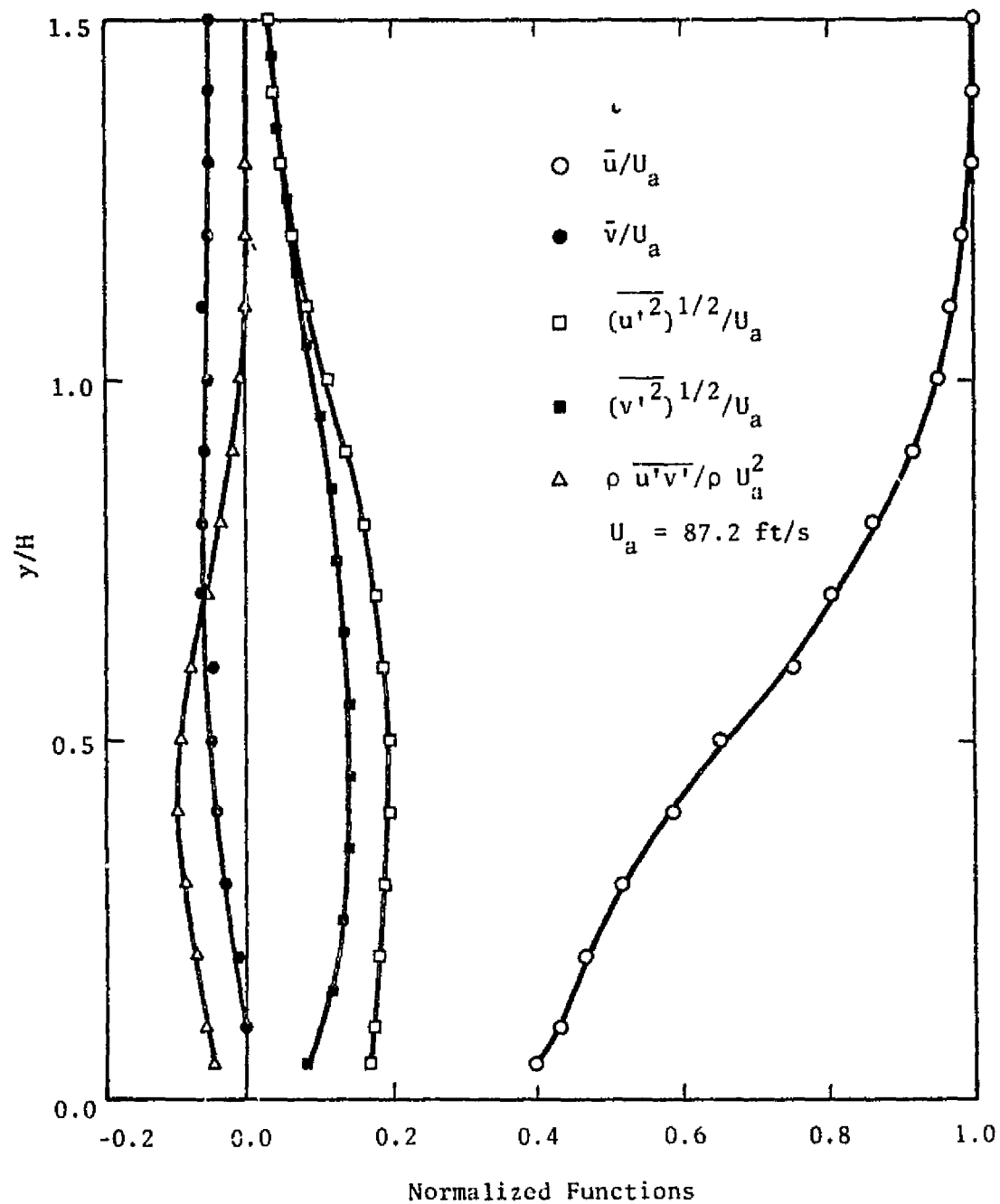


Figure 4.13 Velocity and Reynolds Stress Distributions at $x/H = 8.0$

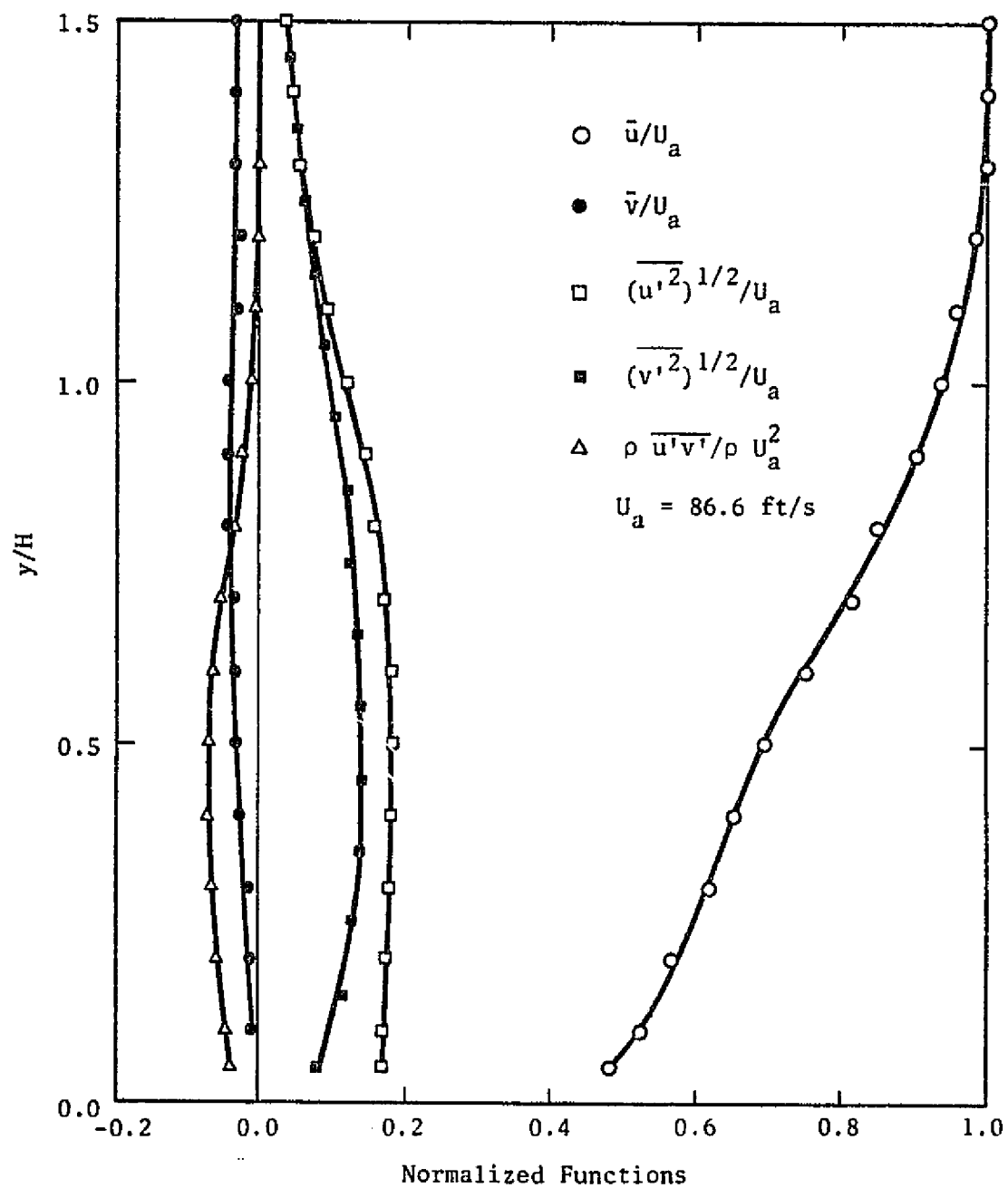


Figure 4.14 Velocity and Reynolds Stress Distributions at $x/H = 9.0$

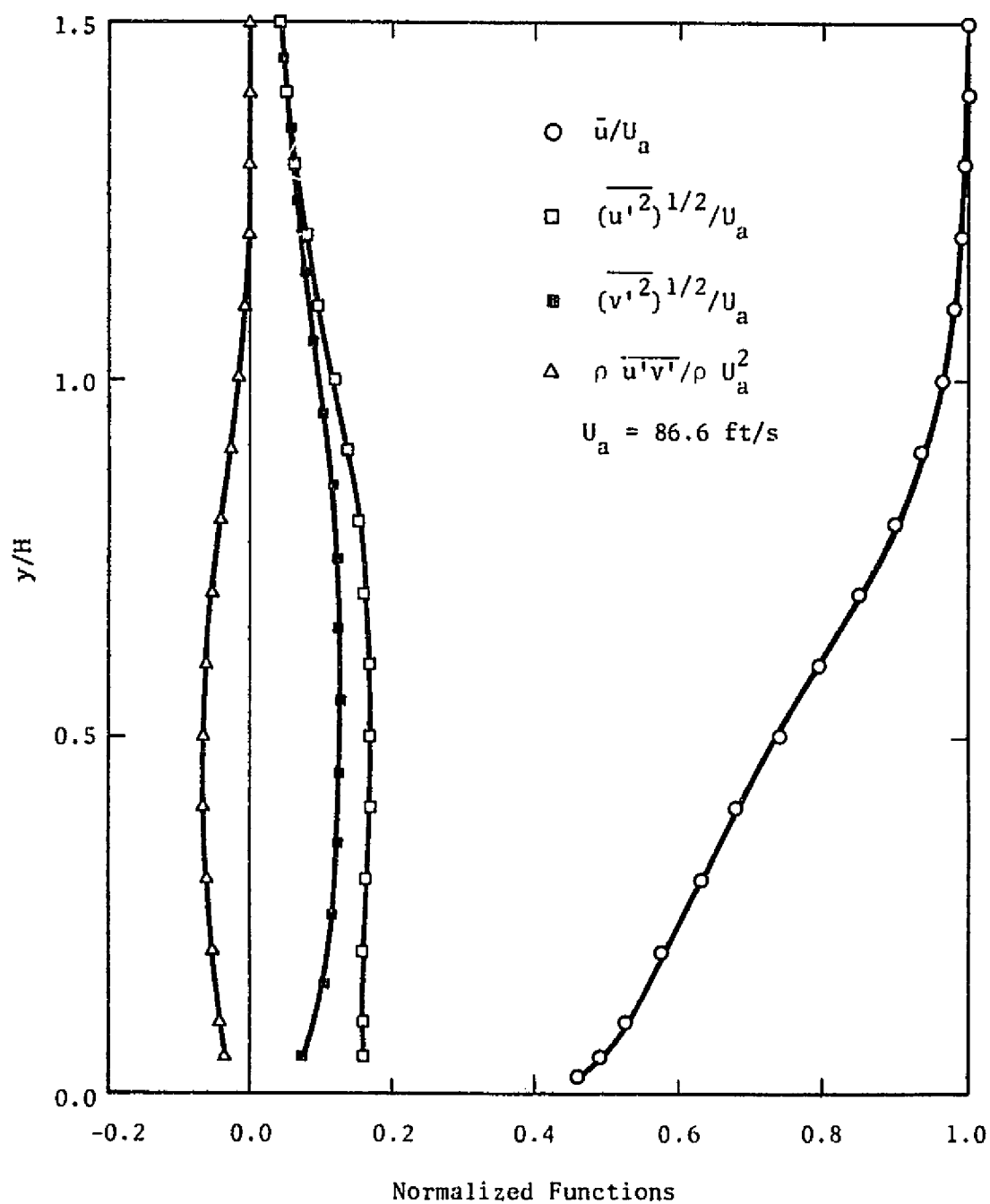


Figure 4.15 Velocity and Reynolds Stress Distributions at $x/H = 10.0$

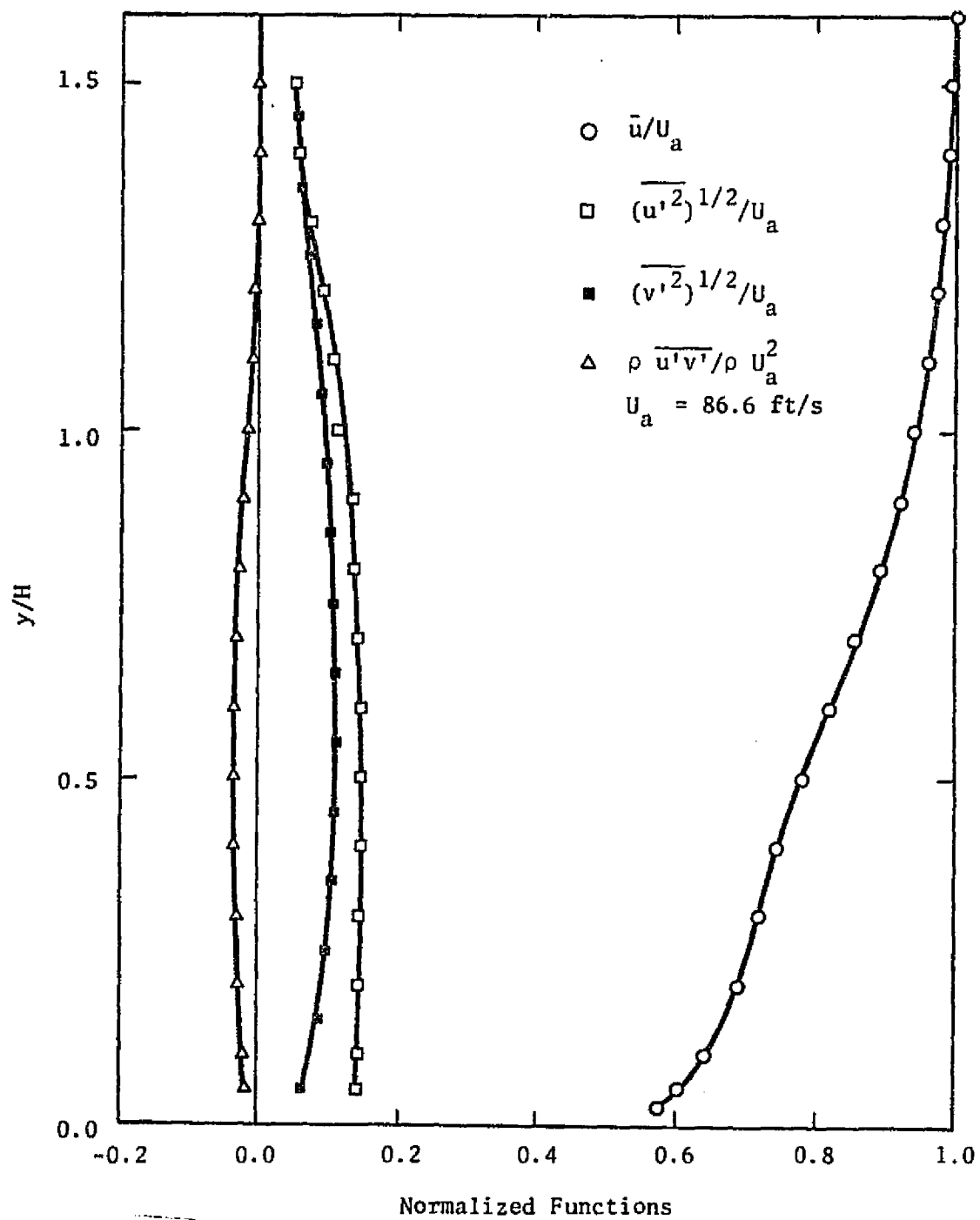


Figure 4.16 Velocity and Reynolds Stress Distributions at $x/H = 12.0$

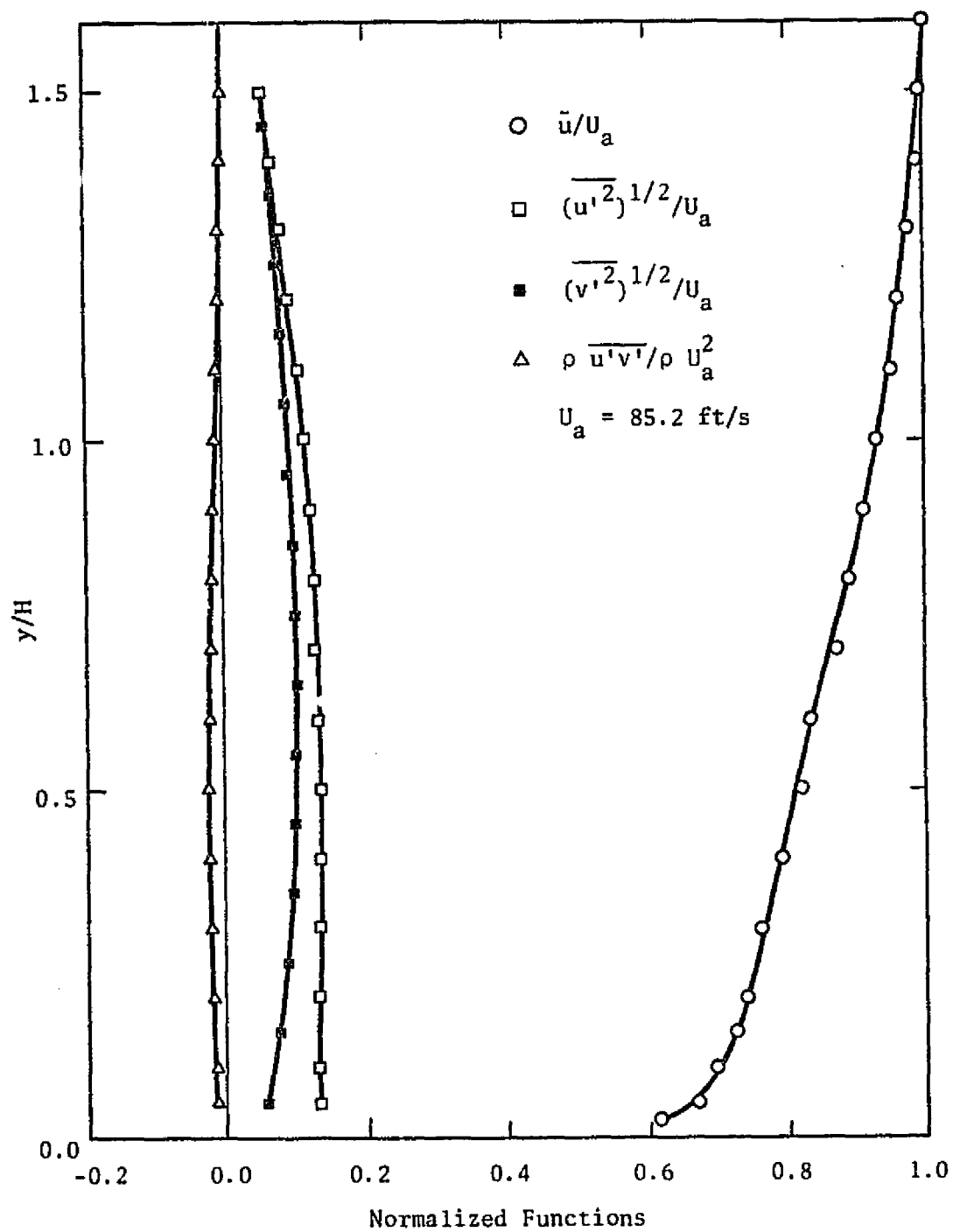


Figure 4.17 Velocity and Reynolds Stress Distributions at $x/H = 14.0$

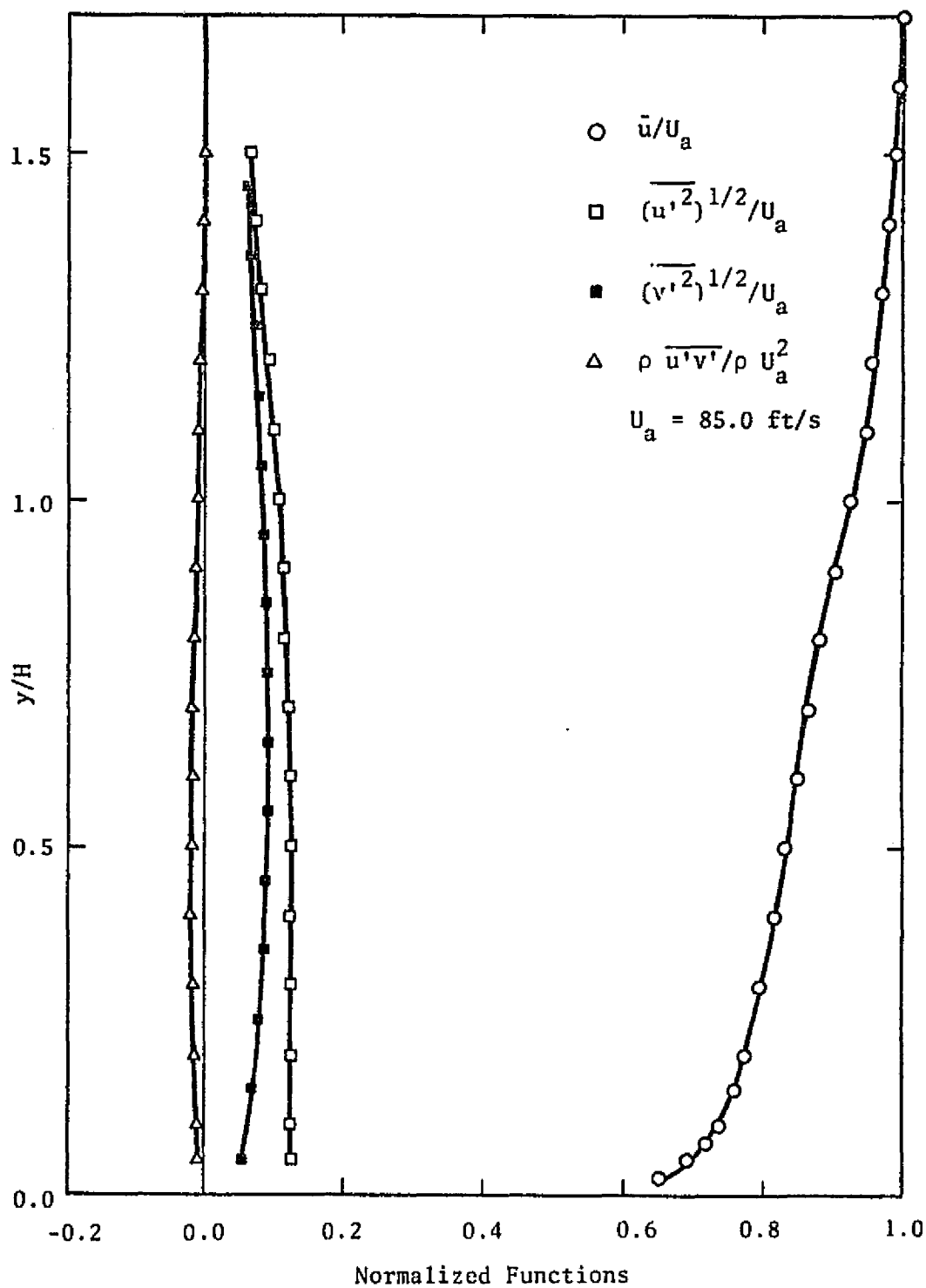


Figure 4.18 Velocity and Reynolds Stress Distributions at $x/H = 16.0$

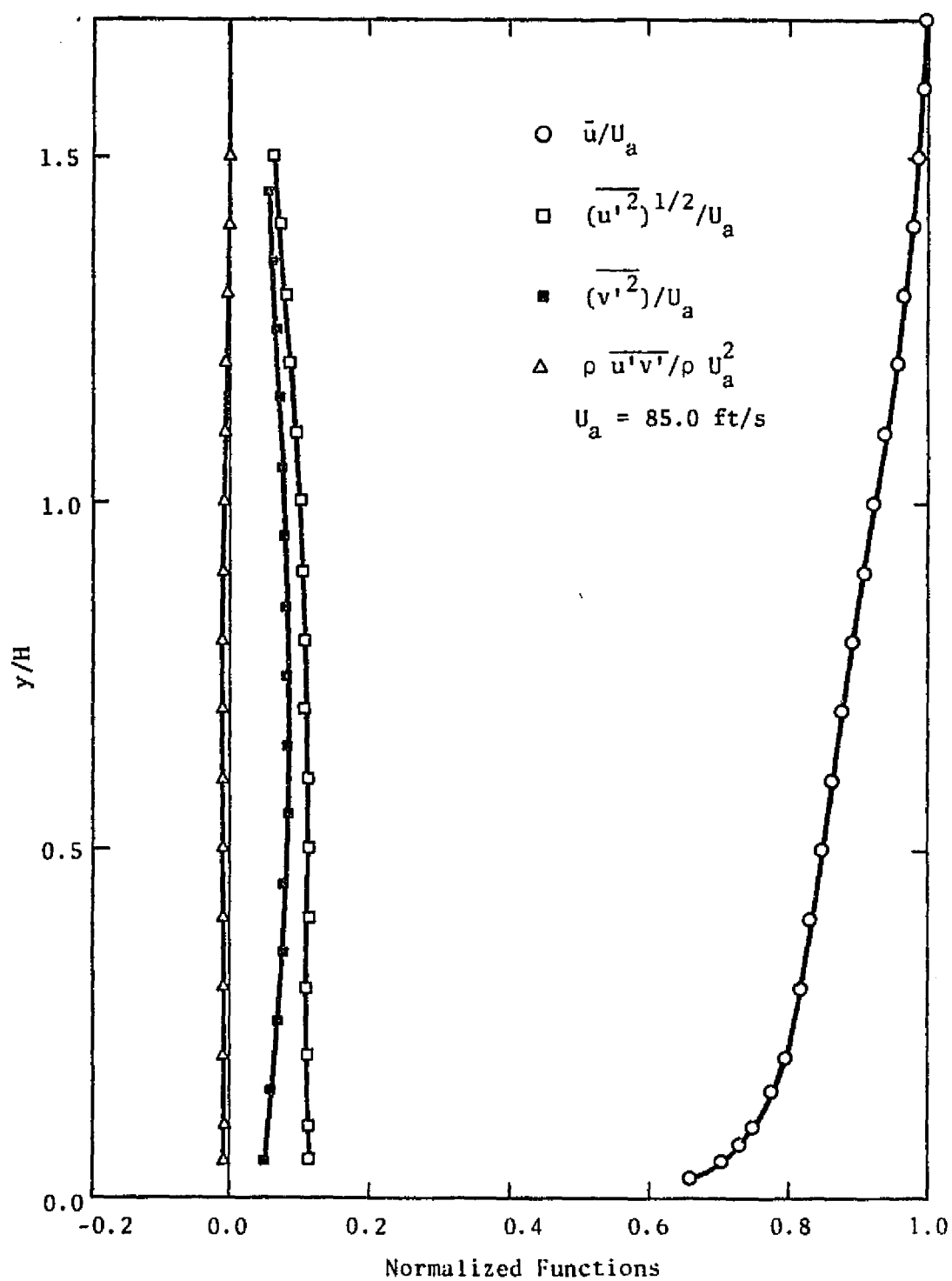


Figure 4.19 Velocity and Reynolds Stress Distributions at $x/H = 18.0$

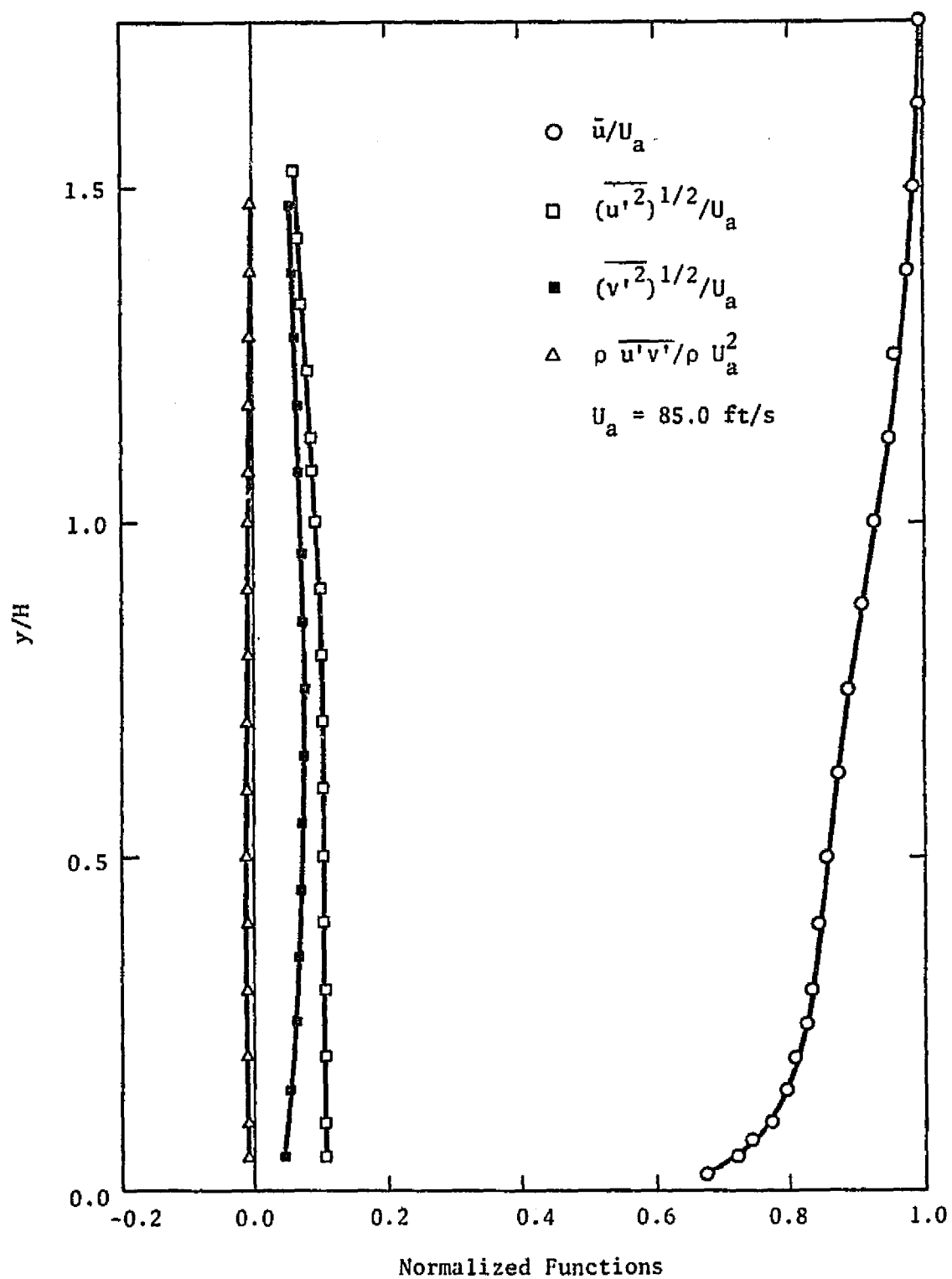


Figure 4.20 Velocity and Reynolds Stress Distributions at $x/H = 20.0$

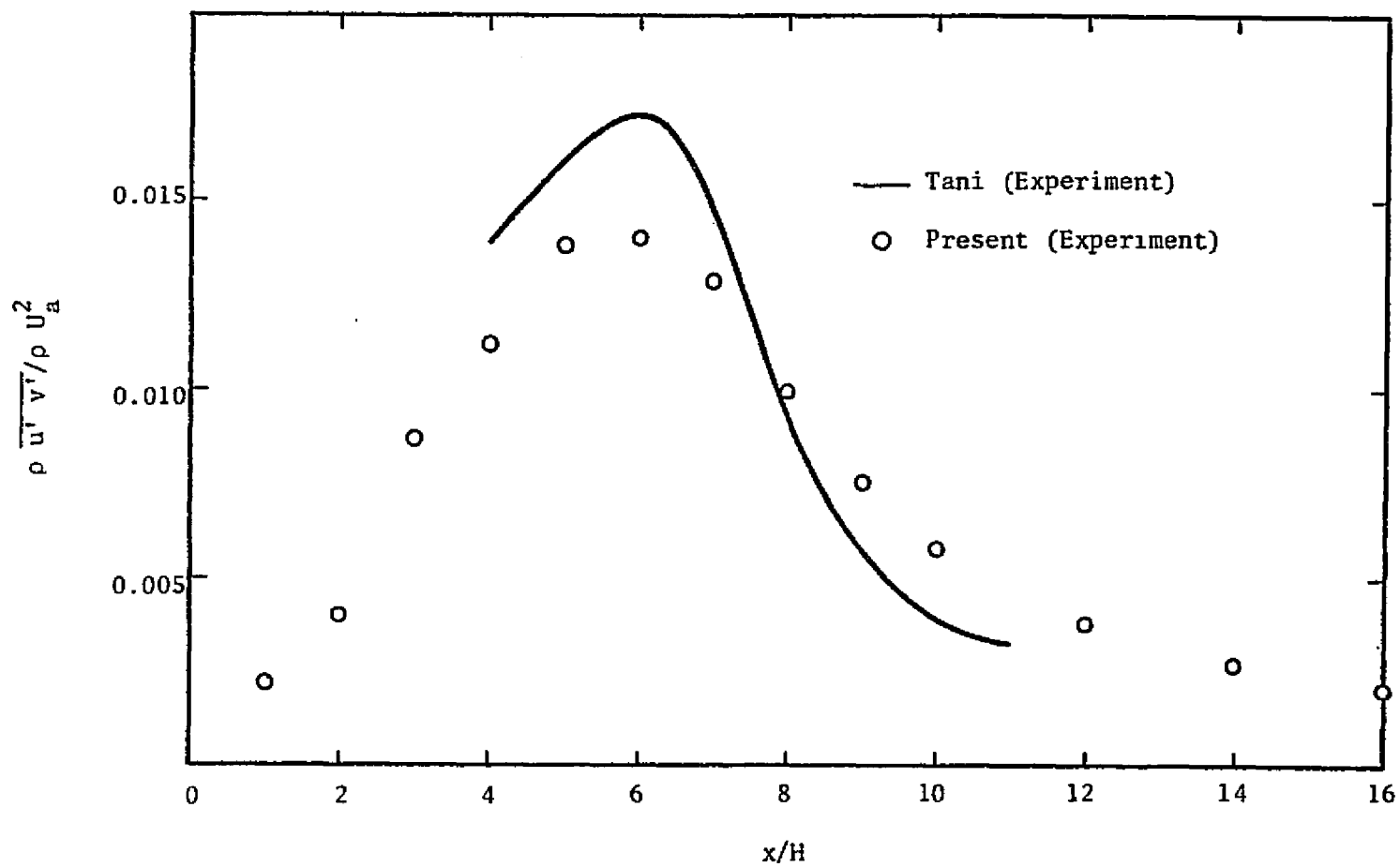


Figure 4.21 Variation of the Maximum Shear Stress in the Wake Region

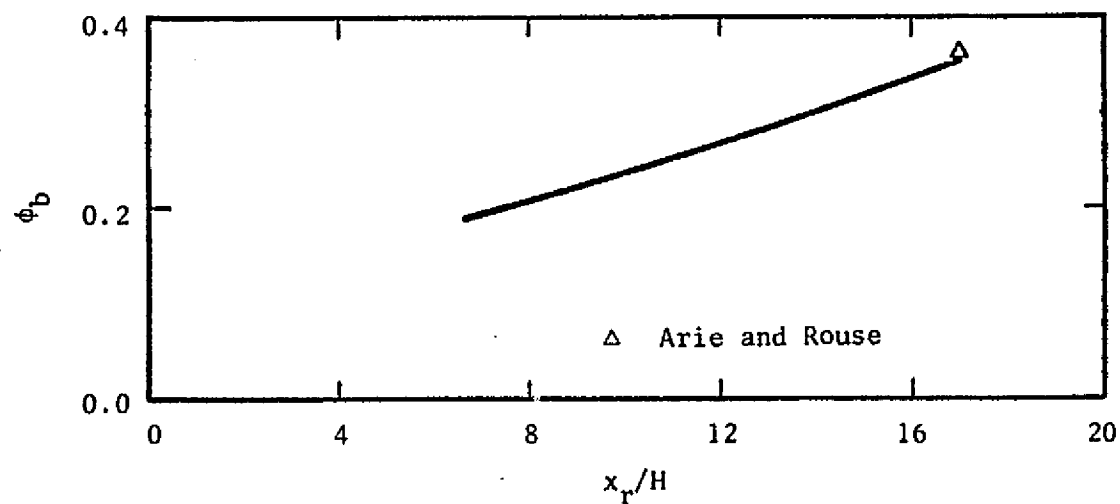
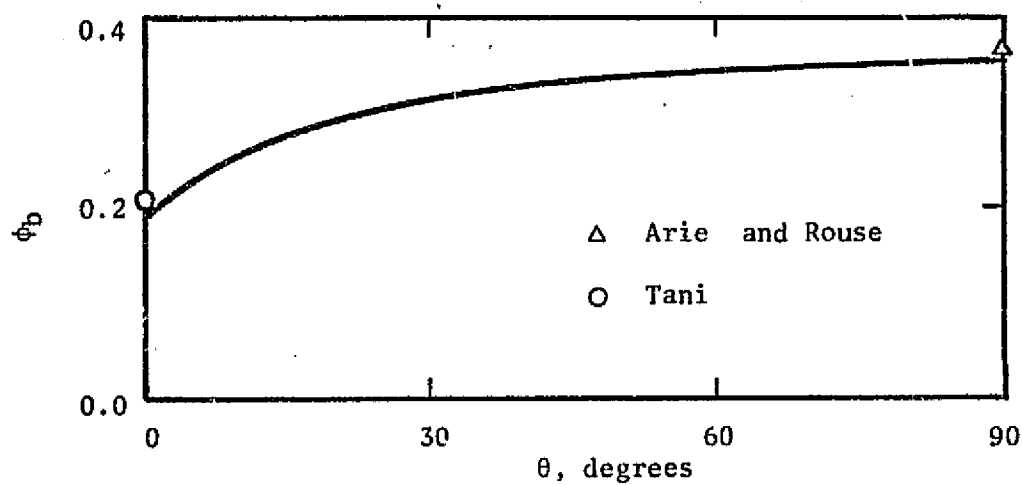


Figure 4.22 Variation of the Maximum Reverse Flow Velocity in the Wake Region

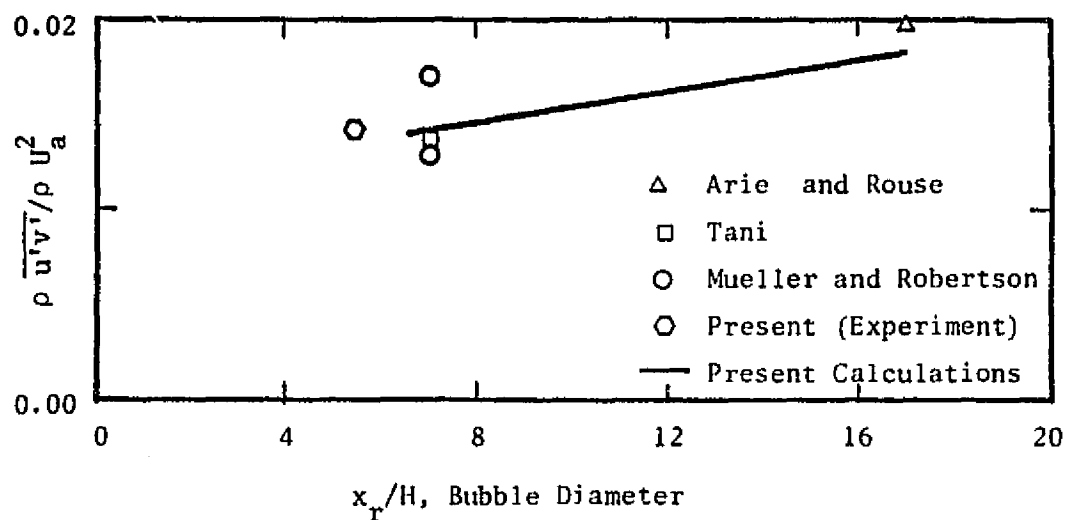
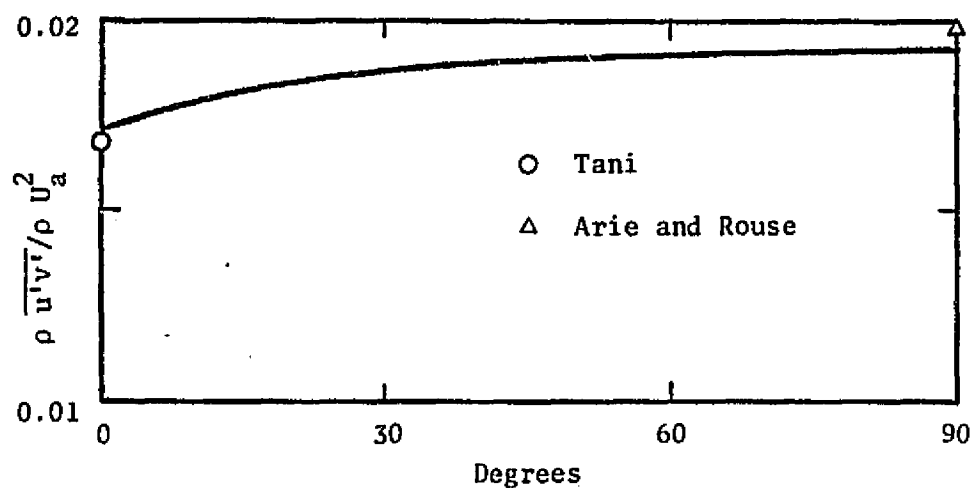


Figure 4.23 Variation of the Maximum Shear Stress in the Wake Region

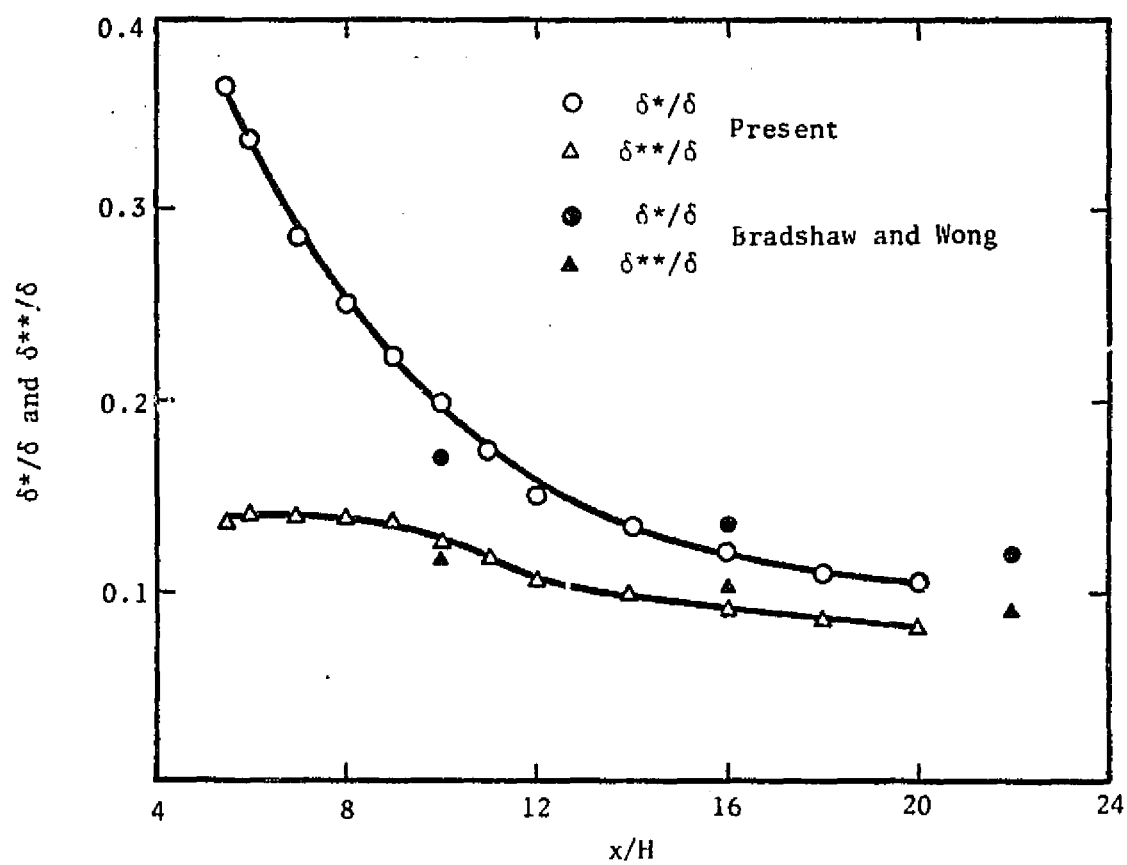


Figure 4.24 Variation of Displacement and Momentum Thickness after Reattachment

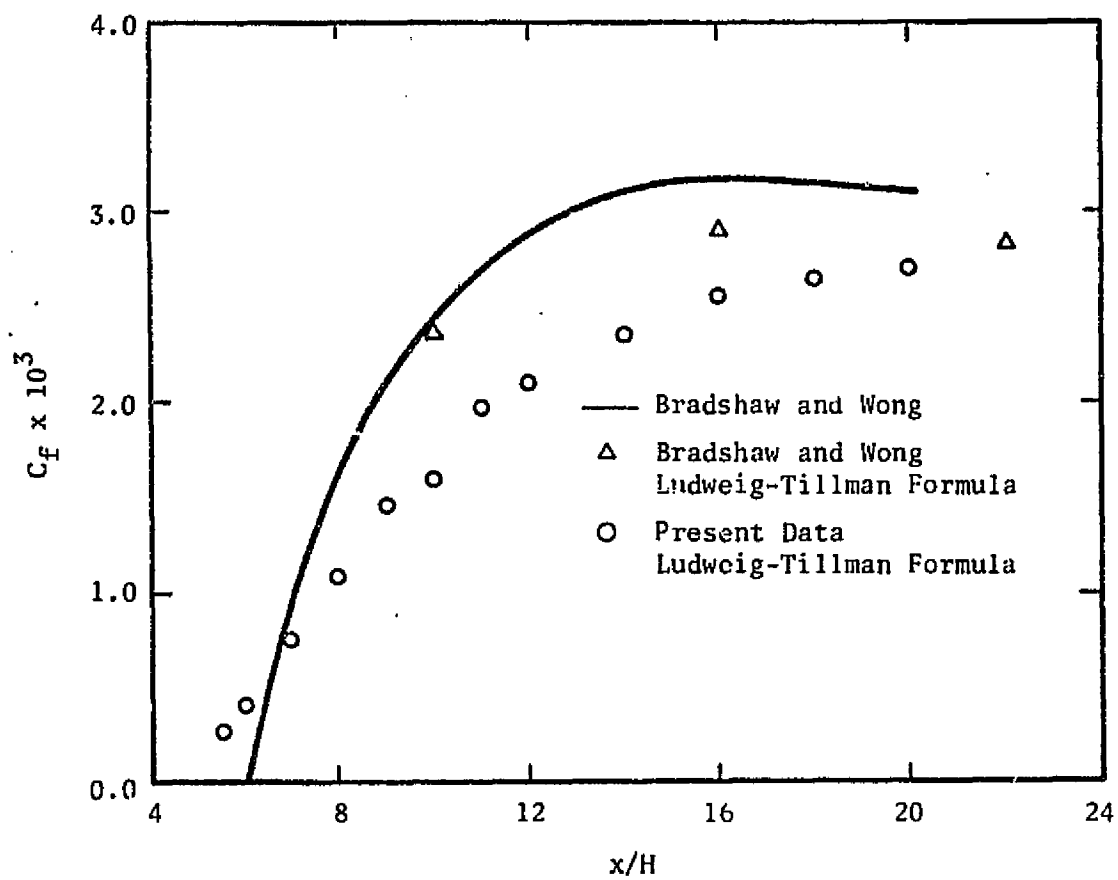


Figure 4.25 Variation of Shear Stress on the Wall after Reattachment

REFERENCES

1. Warpinski, N. R., "Incompressible Flow past Wedges at High Reynolds Numbers," Ph.D. Thesis, Department of Mechanical and Industrial Engineering, University of Illinois at Urbana-Champaign, Urbana, Ill., February 1977.
2. Kirchoff, G., "Zur Theorie freier Flussigkeitsstrahlen," Crelles Journal fur Mathematik, Vol. 70, 1869, pp. 289-298.
3. Riabouchinsky, D., Proc., London Mathematical Society, Vol. 19, No. 2, 1921, pp. 206-215.
4. Von Karman, T. and Ruback, H., "Über den Mechanisms des Flüssigkeitsund Luftwiderstandes," Phys. F., Vol. 49, 1912.
5. Heisenberg, W., "Die absoluten Dimensionen der Karmanschen Wirbelbewegung," Phys. Z., Vol. 22, 1922, pp. 363-366.
6. Kriesel, G., "Cavitation with Finite Cavitation Numbers," Admiralty Res. Lab., Report, No. R1/H/36, 1946.
7. Efros, D., "Hydrodynamical Theory of Two-dimensional Flow with Cavitation," Dokl. Akad. Nauk., SSSR 51, 1946, pp. 267-270.
8. Eppler, R., "Beitrage zur Theorie und Anwendung der Unstetigen Stronungen," J. Rat. Mech. Anal., Vol. 3, 1954, pp. 591-644.
9. Roshko, A., "A New Hodograph for Free Streamline Theory," NACA TN 3168, 1954.
10. Wu, T., "A Free Streamline Theory for Two-dimensional Fully Cavitated Hydrofoils," J. of Mathematical Physics, Vol. 35, 1956, pp. 236-265.
11. Parkinson, G. V. and T. Jandali, "A Wake Source Model for Bluff Body Potential Flow," Journal of Fluid Mechanics, 1970, Vol. 40, Part 3, pp. 477-594.
12. Crocco, L. and Lees, L., "A Mixing Theory for the Interaction between Dissipative Flows and Nearly Isentropic Streams," J. of Aerospace Science, Vol. 19, 1952, pp. 649-676.
13. Korst, H. H., "A Theory for Base Pressure in Transonic and Supersonic Flow," J. of Applied Mechanics, Vol. 23, 1956, pp. 593-600.
14. Chapman, D. R., "An Analysis of Base Pressure at Supersonic Velocities and Comparison with Experiment," NACA TN 2137, 1951.
15. Chapman, D. R., Kuehn, D. M., and Larson, H. K., "Investigation of Separated Flows in Supersonic and Subsonic Streams with Emphasis on the Effect of Transition," NACA TN 3869, 1957.

16. Moore, F. K., "Theory of Laminar Flow," Vol. IV, High Speed Aerodynamics and Jet Propulsion, Princeton University Press, Princeton, New Jersey, 1958.
17. Carriere, P. and Sirieix, M., "Facteurs d'Influence du Recollement d'un Ecollement Supersonique," Proc., Tenth Int. Congress of Applied Mechanics, Italy, September 1960.
18. Golik, R. J., "On the Dissipative Mechanics within Separated Flow Regions," Ph.D. Thesis, Department of Mechanical and Industrial Engineering, University of Illinois, Urbana, Ill., 1962.
19. Nash, J. F., "An Analysis of Two-dimensional Turbulent Base Flow Including the Effect of the Approaching Boundary Layer," ARC R&M No. 3344, 1962.
20. Nash, J. F., Quincy, V. G., and Callinan, J., "Experiments on Two-dimensional Base Flow at Supersonic and Transonic Speeds," NPL Aero Report No. 1070, 1963.
21. McDonald, H., "Turbulent Shear Layer Reattachment with Special Emphasis on the Base Pressure Problem," Aeronautical Quarterly, August 1964, XV, pp. 247.
22. McDonald, H., "An Analysis of the Turbulent Base Pressure Problem in Supersonic Axisymmetric Flow," Aeronautical Quarterly, May 1965, XVI, pp. 247-280.
23. Lees, L. and Reeves, B. L., "Supersonic Separated and Reattaching Laminar Flow: I. General Theory and Application to Adiabatic Boundary Layer-Shock Wave Interactions," AIAA J., 1964, No. 2, pp. 1907-1920.
24. Reeves, B. L. and Lees, L., "Theory of Laminar Near Wake of Blunt Bodies in Hypersonic Flow," AIAA J., 1965, No. 3, pp. 2061-2074.
25. Alber, I. E., "Integral Theory for Turbulent Base Flows at Subsonic and Supersonic Speeds," Ph.D. Thesis, California Institute of Technology, Pasadena, Cal., 1967.
26. Alber, I. E. and Lees, L., "Integral Theory for Supersonic Turbulent Base Flows," AIAA J., 1968, pp. 1343-1351.
27. Shamroth, S. J. and McDonald, H., "A New Solution of the Turbulent Near-Wake Recompression Problem," AIAA Paper No. 70-228, 1970.
28. Korst, H. H., Page, R. H., and Childs, M. E., "A Theory for Base Pressure in Transonic and Supersonic Flow," Department of Mechanical and Industrial Engineering, University of Illinois, ME TN-392-2, 1955.

29. Carpenter, P. W. and Tabakoff, W., "Survey and Evaluation of Supersonic Base Flow Theories," NASA CR 97129, 1968.
30. Chang, P. K., Separation of Flow, Pergamon Press, London, 1970.
31. Berger, S. A., Laminar Wakes, American Elsevier Pub. Co., Inc., New York, 1971.
32. Page, R. H., "A Review of Component Analysis of Base Pressure for Supersonic Turbulent Flow," Proc., Tenth Int. Symposium on Space Technology and Science, Tokyo, 1973, pp. 459-469.
33. Chow, W. L., "Recompression of a Two-dimensional Supersonic Turbulent Free Shear Layer," Development in Mechanics, Vol. 6, Proc., Twelfth Midwestern Mechanics Conference, University of Notre Dame, Notre Dame, Indiana, August 1971, pp. 319-332.
34. Spring, D. J., "Supersonic Laminar Flow Reattachment and Redevelopment behind a Two-dimensional Rearward Facing Step," Ph.D. Thesis, Department of Mechanical and Industrial Engineering, University of Illinois at Urbana-Champaign, Urbana, Ill., 1972.
35. Chow, W. L. and Spring, D. J., "The Viscous Interaction of Flow Redevelopment after Reattachment with Supersonic External Flows," AIAA J., Vol. 13, No. 12, December 1975, pp. 1576-1584.
36. Weng, C. H., "Base Pressure Problems Associated with Supersonic Axisymmetric External Flow Configurations," Ph.D. Thesis, Department of Mechanical and Industrial Engineering, University of Illinois at Urbana-Champaign, Urbana, Ill., 1975.
37. Green, J. E., "Two-dimensional Turbulent Reattachment as a Boundary-layer Problem," AGARD Conf. Proc., No. 4, 1966, pp. 393-427.
38. Tanner, M., "Totwasserbeeinflussung bei Keilströmungen," Deutsche Luft-und Raumfahrt, Forschungsbericht 64-39, November 1964.
39. Tanner, M., "Theorie der Totwasserströmungen um angestellte Keile," Deutsche Luft-und Raumfahrt, Forschungsbericht 65-14, March 1965.
40. Tanner, M., "Einfluss der Reynoldszahl und der Grenzschichtdicke auf den Totwasserdruck bei der Umströmungen von Keilen," Deutsche Luft-und Raumfahrt, Forschungsbericht 65-18, May 1965.
41. Tanner, M., "Ein Verfahren zur Berechnung des Totwasserdruckes und Widerstandes von stumpfen Körpern bei inkompressibler nichtperiodischer Totwasserströmung," Dissertation Braunschweig, 1967, Mitteilungen aus dem Max-Planck-Institut für Strömungsforschung und der Aerodynamischen Versuchsanstalt, Göttingen, No. 39, 1967.

42. Tanner, M., "Theoretical Prediction of Base Pressure for Steady Base Flow," Progress in Aerospace Sciences, Vol. 14, Pergamon Press, London, 1973, pp. 177-225.
43. Schlichting, H., "Recent Progress in Boundary Layer Research," AIAA J., Vol. 12, No. 4, April 1974, pp. 427-440.
44. Chow, W. L. and Spring, D. J., "The Viscous Interaction of Incompressible Separated Flows," TR RD-73-22, U.S. Army Missile Command, Redstone Arsenal, Ala., May 1974.
45. Chow, W. L. and Spring, D. J., "Viscid-Inviscid Interaction of Incompressible Separated Flows," J. of Applied Mechanics, Vol. 98, No. 3, September 1976, pp. 387-395.
46. Tani, I., "Experimental Investigation of Flow Separation over a Step," Grenzschichtforschung IUTAM-Symposium, Freiburg, 1957, Springer-Verlag, 1958, pp. 377-386.
47. Pohlhausen, K., "Zur näherungsweise Integration der Differentialgleichung der laminaren Reibungsschicht," ZAMM 1, 1921, pp. 252-268.
48. Holstein, H. and Bohlen, T., "Ein einfaches Verfahren zur Berechnung laminarer Reibungsschichten die dem Näherungsansatz von K. Pohlhausen genügen," Lilienthal-Bericht, S 10, 1940, pp. 5-16.
49. Truckenbrodt, E., "Ein Quadraturverfahren zur Berechnung der laminaren und turbulenten Reibungsschicht bei ebener und rotationssymmetrischer Strömung," Ing.-Arch., 20, 1952, pp. 211-228.
50. Brink, D. F. and Chow, W. L., "Two-dimensional Jet Mixing with a Pressure Gradient," J. of Applied Mechanics, Vol. 42, Series E, No. 1, pp. 55-60.
51. Bradshaw, P. and Wong, F.Y.F., "The Reattachment and Relaxation of a Turbulent Shear Layer," J. of Fluid Mechanics, Vol. 52, Part 1, 1972, pp. 113-135.
52. Arie, M. and Rouse, H., "Experiments on Two-dimensional Flow over a Normal Wall," J. of Fluid Mechanics, Vol. 1, Part 2, 1956, pp. 129-141.
53. Tani, I., Iuchi, M., and Komoda, H., "Experimental Investigation of Flow Separation associated with Step or Groove," University of Tokyo-Aeronautical Research Institute Report No. 364, April 1961, pp. 119-137.
54. Mueller, T. J. and Robertson, J. M., "A Study of the Mean Motion and Turbulence Downstream of a Roughness Element," Developments in Theoretical and Applied Mechanics, Vol. 1, Plenum Press, 1963, pp. 326-340.

APPENDIX A

THE CORRESPONDING INVISCID FLOW WITH A TOP WALL BOUNDARY

In order to assess the effect of a top wall at a certain distance from a wedge, an analysis has been devised which considers the effect of this wall on the corresponding inviscid flow. The situation is exactly the same as that described in Chapter 2. In addition, there exists a bounding top wall at a distance R from the centerline of the wedge as shown in Fig. A.1a.

The fluid on the bounding streamline along the wedge surface will behave in the same way as described for the infinite corresponding inviscid flow; however, the bounding streamline of the top wall must also be considered. The fluid on this streamline must accelerate from state A to some unknown state P in the hodograph which is physically located above and near the wake region. Afterward, it must decelerate until it achieves the downstream condition at F. The hodograph for the entire flow is shown in Fig. A.2a where

$$\bar{q} = u - iv. \quad (A.1)$$

It should be mentioned that states A and F need not be the same ($R_F \neq R$) and the most noticeable effect of incorporating the top wall is the extension of the branch cut along the u axis. The corresponding ζ and ω planes with

$$\zeta = 1/\bar{q} \quad (A.2)$$

and

$$\omega = \ln \zeta \quad (A.3)$$

are shown in Figs. A.2b and A.3a, respectively.

The ω plane is polygonal and a Schwarz-Christoffel transformation can subsequently be employed to map the interior of the polygon into the upper half of the t plane as shown in Fig. A.3b. This transformation is expressed as

$$\omega = c_1 \int \frac{\left(t + \frac{1}{k_1}\right) dt}{\left(t + \frac{1}{k_3}\right) \left(t - \frac{1}{k_4}\right) \sqrt{t^2 - 1}} + c_2 \quad (A.4)$$

The constant k_2 , which is the corresponding location of the upstream infinite state, does not enter into the transformation. The constants c_1 and c_2 are to be evaluated from the conditions of

$$\omega(t = 1) = -i\alpha \text{ and } \omega(t = -1) = i\theta \quad (A.5)$$

and k_1 , k_2 , k_3 , and k_4 are unknown parameters which must be determined from the analysis.

The upper half t plane can be transformed into the ℓ plane shown in Fig. A.3c by the transformation

$$\ell = \frac{R}{\pi} \log \left(t + \frac{1}{k_2} \right) \quad (A.6)$$

The final W plane can now be written as

$$W = U \ell \quad (A.7)$$

where U is a constant and is the value of a uniform velocity between the two boundaries. From mass flow considerations, it is obvious that

$U = V_{\infty A}$ if R has the same value for the ℓ plane as it does for the physical plane. W can finally be written as

$$W = \frac{V_{\infty A} R}{\pi} \log \left(t + \frac{1}{k_2} \right) \quad (A.8)$$

Upon integrating Eq. (A.4) and determining the constants c_1 and c_2 , the conjugate velocity \bar{q} is found to be given by

$$\bar{q} = \frac{1}{\zeta} = \left[\frac{t + \frac{1}{k_3}}{1 + \frac{t}{k_3} + \sqrt{\left(\frac{1}{k_3^2} - 1\right)(t^2 - 1)}} \right]^{\theta/\pi} \left[\frac{t - \frac{1}{k_4}}{\frac{t}{k_4} - 1 + \sqrt{\left(\frac{1}{k_4^2} - 1\right)(t^2 - 1)}} \right]^{\alpha/\pi} \quad (\text{A.9})$$

which is the same expression as that derived for the infinite case. This is entirely reasonable since the ζ planes for the two cases are identical except for the extended branch cut which only limits the region of applicability.

In order to relate locations in the t plane to locations in the physical plane, it is necessary to employ the usual definition of

$$\bar{q} = \frac{1}{\zeta} = \frac{1}{V_o} \frac{dW}{dz} = \frac{1}{V_o} \frac{dW}{dt} \frac{dt}{dz} \quad (\text{A.10})$$

Substituting Eq. (A.8) for W , Eq. (A.10) becomes

$$\frac{1}{\zeta} = \frac{1}{V_o} \left[\frac{V_{\infty A} R}{\pi} \frac{1}{\left(t + \frac{1}{k_2}\right)} \right] \frac{dt}{dz} \quad (\text{A.11})$$

and by rearranging, it is found that

$$\frac{dz}{dt} = \frac{V_{\infty A} R}{V_o} \frac{1}{\pi} \frac{\zeta}{\left(t + \frac{1}{k_2}\right)} \quad (\text{A.12})$$

The one-to-one correspondence between the t plane and the physical plane is determined by integrating Eq. (A.12) so that

$$\int d(z/H) = \frac{V_{\infty A} R}{V_o} \frac{1}{H} \frac{1}{\pi} \int \frac{\zeta dt}{t + \frac{1}{k_2}} \quad (\text{A.13})$$

where the expression for ζ is given in Eq. (A.9).

For a particular problem, θ and R/H are given and a pair of values of α and k_4 are arbitrarily selected. Constants k_1 , k_2 , and k_3 must then be determined.

One criterion that must be met is

$$V_{\infty F} R_F = V_{\infty A} R \quad (A.14)$$

which can be converted into

$$R_F \left[\frac{1}{\frac{1}{k_3} + \sqrt{\frac{1}{k_3^2} - 1}} \right]^{\theta/\pi} \left[\frac{1}{\frac{1}{k_4} + \sqrt{\frac{1}{k_4^2} - 1}} \right]^{\alpha/\pi} =$$

$$R \left[\frac{1/k_2 - 1/k_3}{\frac{1}{k_2 k_3} - 1 + \sqrt{\left(\frac{1}{k_3^2} - 1\right)\left(\frac{1}{k_2^2} - 1\right)}} \right]^{\theta/\pi} \left[\frac{1/k_2 + 1/k_4}{\frac{1}{k_2 k_4} + 1 + \sqrt{\left(\frac{1}{k_4^2} - 1\right)\left(\frac{1}{k_2^2} - 1\right)}} \right]^{\alpha/\pi} \quad (A.15)$$

This equation involves k_2 , k_3 , and k_4 and cannot be solved explicitly for any of them. To obtain a second relation, Eq. (A.13) is integrated from B to C in the physical plane and from $-1/k_3$ to -1 in the t plane to obtain

$$\frac{1}{\sin \theta} = \frac{V_{\infty A}}{V_0} \frac{1}{(H + R - R_F) \pi} \int_{-1/k_3}^{-1} \frac{\zeta dt}{t + 1/k_2} \quad (A.16)$$

$V_{\infty A}/V_0$ is given by the right-hand side of Eq. (A.15) and the correct value of k_2 is determined through integration. Since ζ and $V_{\infty A}/V_0$ are functions of k_3 and k_4 , Eqs. (A.15) and (A.16) must be solved together through an iteration procedure. k_1 can be determined explicitly from the equation

$$\frac{1}{k_1} = \frac{\left(\frac{1}{k_3} \frac{\alpha}{\theta} \frac{\sqrt{1/k_4^2 - 1}}{\sqrt{1/k_3^2 - 1}} \right) + \frac{1}{k_4}}{\left(\frac{\alpha}{\theta} \frac{\sqrt{1/k_4^2 - 1}}{\sqrt{1/k_3^2 - 1}} \right) - 1} \quad (\text{A.17})$$

which is obtained by examining the transformation around either the singularity at $t = -1/k_3$ or $t = 1/k_4$. Once the constants have been determined, the analysis is handled in exactly the same way described in Chapter 2. The same transformations are employed at singularities $-1/k_3$ and $1/k_4$ and the negative branch of both square root functions within Eq. (A.15) must be employed when $t < -1$.

The calculations described in Chapter 3 are performed with $R_F = R$ and various values of R/H . The analysis must be handled carefully for $R/H < 10$ since the constants k_2 and k_3 approach one.

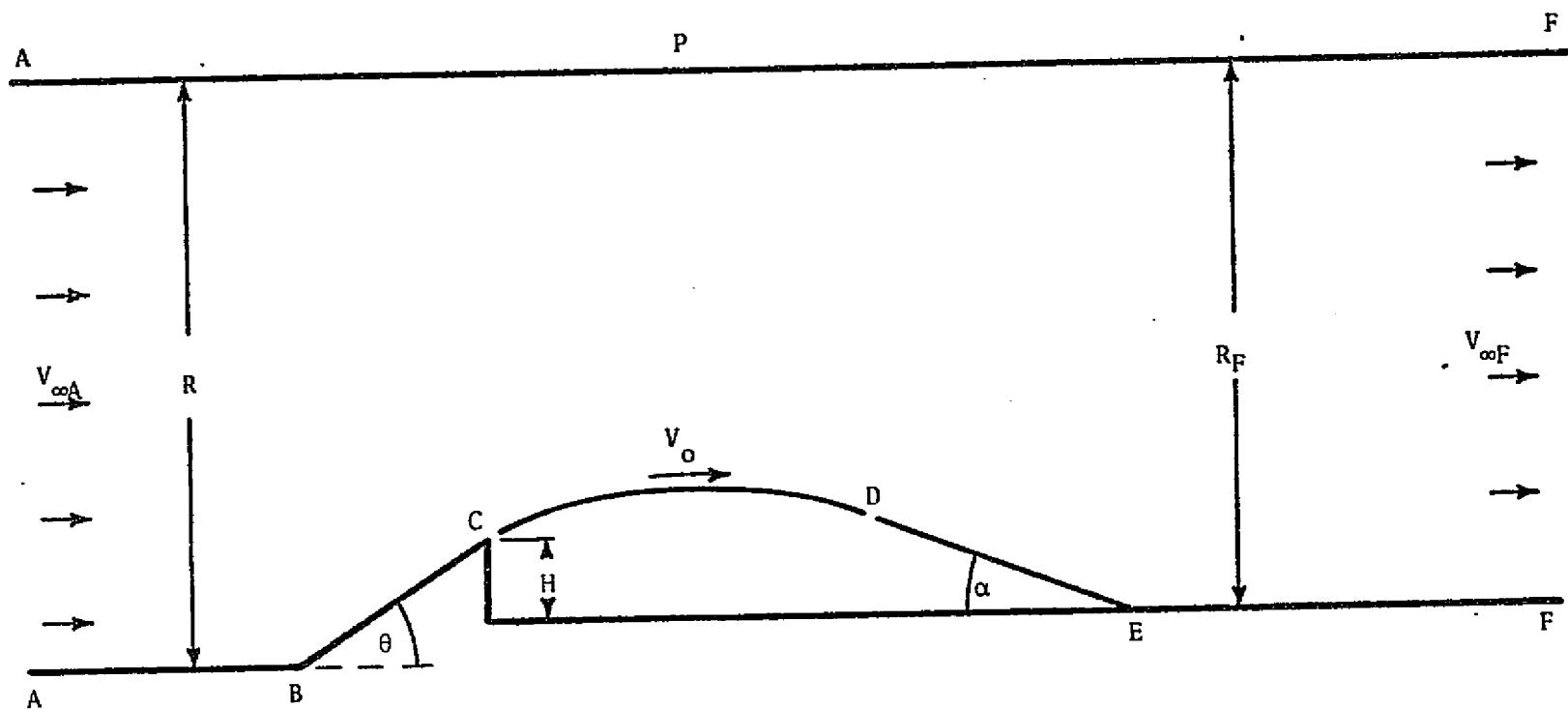
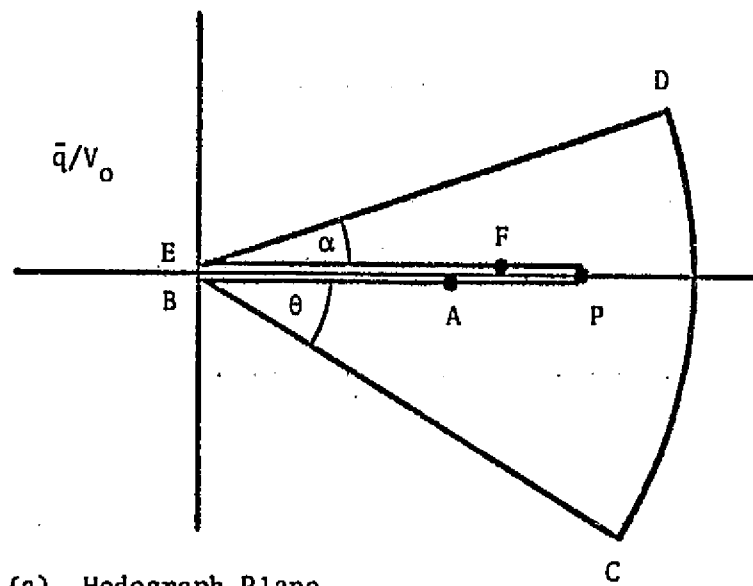
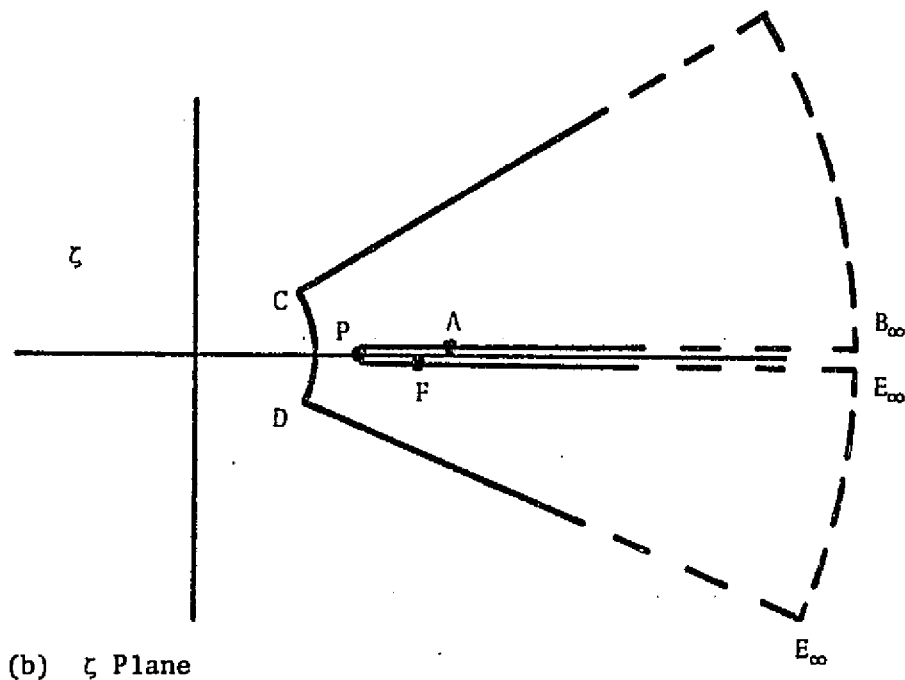


Figure A.1 Inviscid Flow past a Wedge with a Top Wall Boundary

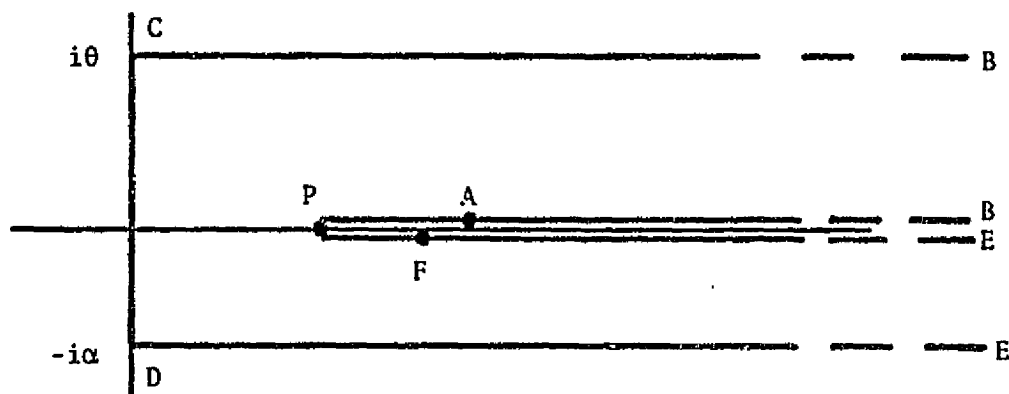


(a) Hodograph Plane

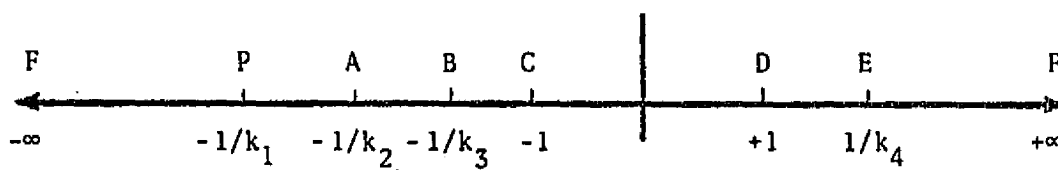


(b) ζ Plane

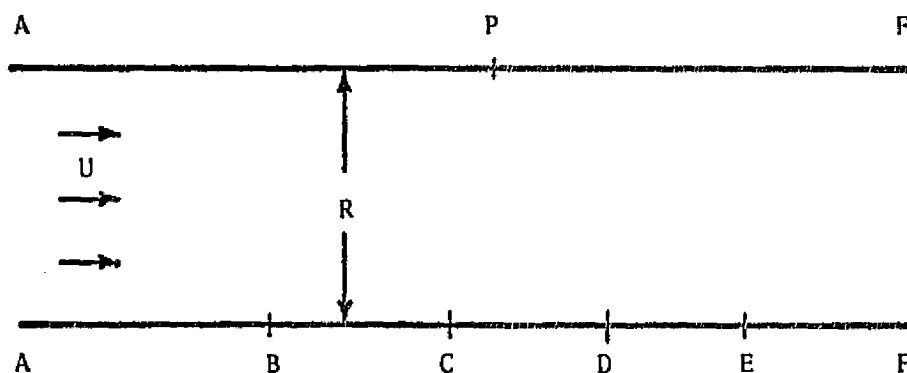
Figure A.2 Transformations for the Corresponding Inviscid Flow



(a) ω Plane



(b) t Plane



(c) l Plane

Figure A.3 Transformation for the Corresponding Inviscid Flow

APPENDIX B

DETERMINATION OF THE POTENTIAL FLOW VELOCITY

NEAR THE LEADING EDGE OF A WEDGE

The Faulkner-Skan equation

$$f''' + ff'' + \beta(1 - f'^2) = 0 \quad (B.1)$$

is valid only for situations when the potential flow velocity can be expressed as

$$U = C_1 x^m. \quad (B.2)$$

Such situations exist near the leading edge of a wedge with an included angle of $\pi\beta$. m is defined as

$$m = \frac{\beta}{2 - \beta} \quad (B.3)$$

since

$$\pi\beta = 2\theta \quad (B.4)$$

where θ is the wedge half angle of the present analysis, m can finally be expressed as

$$m = \frac{\theta}{\pi - \theta}. \quad (B.5)$$

It is necessary to investigate the velocity in the vicinity of the stagnation point where t may be given by

$$t = -\frac{1}{k_1} + \epsilon \quad (B.6)$$

with ϵ being a small quantity.

The complex velocity is given by

$$\frac{q}{V_0} = \left[\frac{t - \frac{1}{k_2}}{\sqrt{\left(\frac{1}{k_2^2} - 1\right)(t^2 - 1) + \frac{t}{k_2} - 1}} \right]^{\frac{\alpha}{\pi}} \left[\frac{t + \frac{1}{k_1}}{\sqrt{\left(\frac{1}{k_1^2} - 1\right)(t^2 - 1) + \frac{t}{k_1} + 1}} \right]^{\frac{\theta}{\pi}} \quad (B.7)$$

For $t < -1$, the negative branch of both square root functions must be employed. Near the front stagnation point, Eq. (B.7) is reduced to

$$\frac{\bar{q}}{V_o} = \left[\frac{1/k_1 + 1/k_2}{\sqrt{\left(\frac{1}{k_2^2} - 1\right)\left(\frac{1}{k_1^2} - 1\right)} + 1 + \frac{1}{k_1 k_2}} \right]^{\alpha/\pi} \left[\frac{\epsilon}{\sqrt{\left(\frac{1}{k_1^2} - 1\right)\left(\frac{1}{k_1^2} - 1\right)} + \frac{1}{k_1^2} - 1} \right]^{\theta/\pi} \quad (\text{B.8})$$

which can be rewritten as

$$\frac{\bar{q}}{V_o} = C'_1 \epsilon^{\theta/\pi} \quad (\text{B.9})$$

where

$$C'_1 = \left[\frac{1/k_1 + 1/k_2}{\sqrt{\left(\frac{1}{k_2^2} - 1\right)\left(\frac{1}{k_1^2} - 1\right)} + 1 + \frac{1}{k_1 k_2}} \right]^{\alpha/\pi} \left[\frac{1}{\sqrt{\left(\frac{1}{k_1^2} - 1\right)}} \right]^{\theta/\pi} \quad (\text{B.10})$$

To relate ϵ in the t plane to z/H in the physical plane, it is necessary to employ Eq. (2.11) which can be rearranged to give

$$d\left(\frac{z}{H}\right) = \frac{\phi_D}{V_o H} \left[\frac{\sqrt{(1/k_2^2 - 1)(t^2 - 1)} + t/k_2 - 1}{t - \frac{1}{k_2}} \right]^{\alpha/\pi} \cdot \left[\frac{\sqrt{(1/k_1^2 - 1)(t^2 - 1)} + t/k_1 + 1}{t + \frac{1}{k_1}} \right]^{\theta/\pi} dt. \quad (\text{B.11})$$

Upon integrating from $-1/k_1$ to $-1/k_1 + \epsilon$ in the t plane and 0 to z/H in the physical plane and employing the negative branch of both square root functions, Eq. (B.11) can be reduced to

$$\frac{z}{H} = \frac{\phi_D}{V_o H} \left[\frac{\sqrt{(1/k_2^2 - 1)(1/k_1^2 - 1)} + 1 + 1/(k_1 k_2)}{\frac{1}{k_1} + \frac{1}{k_2}} \right]^{\frac{\alpha}{\pi}} \left[2 \left(\frac{1}{k_1^2} - 1 \right) \right]^{\frac{\theta}{\pi}} \cdot e^{i\theta} \int_0^\epsilon \frac{d\epsilon}{\epsilon^{\theta/\pi}} \quad (B.12)$$

After integration, Eq. (B.12) can be rewritten as

$$\left| \frac{z}{H} \right| = C'_2 \epsilon^{(\pi-\theta)/\pi} \quad (B.13)$$

where

$$C'_2 = \left[\frac{\sqrt{(1/k_2^2 - 1)(1/k_1^2 - 1)} + 1 + 1/(k_1 k_2)}{\frac{1}{k_1} + \frac{1}{k_2}} \right]^{\alpha/\pi} \frac{\phi_D}{V_o H} \cdot \left[2 \left(\frac{1}{k_1^2} - 1 \right) \right]^{\theta/\pi} \frac{\pi}{\pi - \theta} \quad (B.14)$$

By solving for ϵ in Eq. (B.13) and substituting into Eq. (B.9), it is found that

$$|\bar{q}| = V_o \frac{C'_1}{C'_2} \left| \frac{z}{H} \right|^{\theta/(\pi-\theta)} \quad (B.15)$$

which is precisely

$$|\bar{q}| = C_1 |z|^m \quad (B.16)$$

with

$$C_1 = V_o \frac{C'_1}{C'_2} \frac{1}{H^m} \quad (B.17)$$

It is more convenient to express C_1 as

$$C_1 = \frac{V_\infty}{H^m} \frac{V_o}{V_\infty} \frac{C'_1}{C'_2 (\theta/\pi - \theta)} \quad (B.18)$$

or

$$C_1 = \frac{V_\infty}{H^m} C \quad (B.19)$$

where

$$C = \frac{V_o}{V_\infty} \frac{C_1}{C'_2 (\theta/\pi - \theta)} \quad (B.20)$$

The constant C_1 is shown in Fig. B.1 as a function of m with α and V_o/V_∞ obtained from calculations for $\sigma = 12$ and $Re_H = 5 \times 10^4$. It has a constant value of about 0.35 for $0.5 < m < 1.0$ and increases sharply as $m \rightarrow 0$. The results for the adjusted σ values are almost identical to those for $\sigma = 12$ and are, therefore, not shown here.

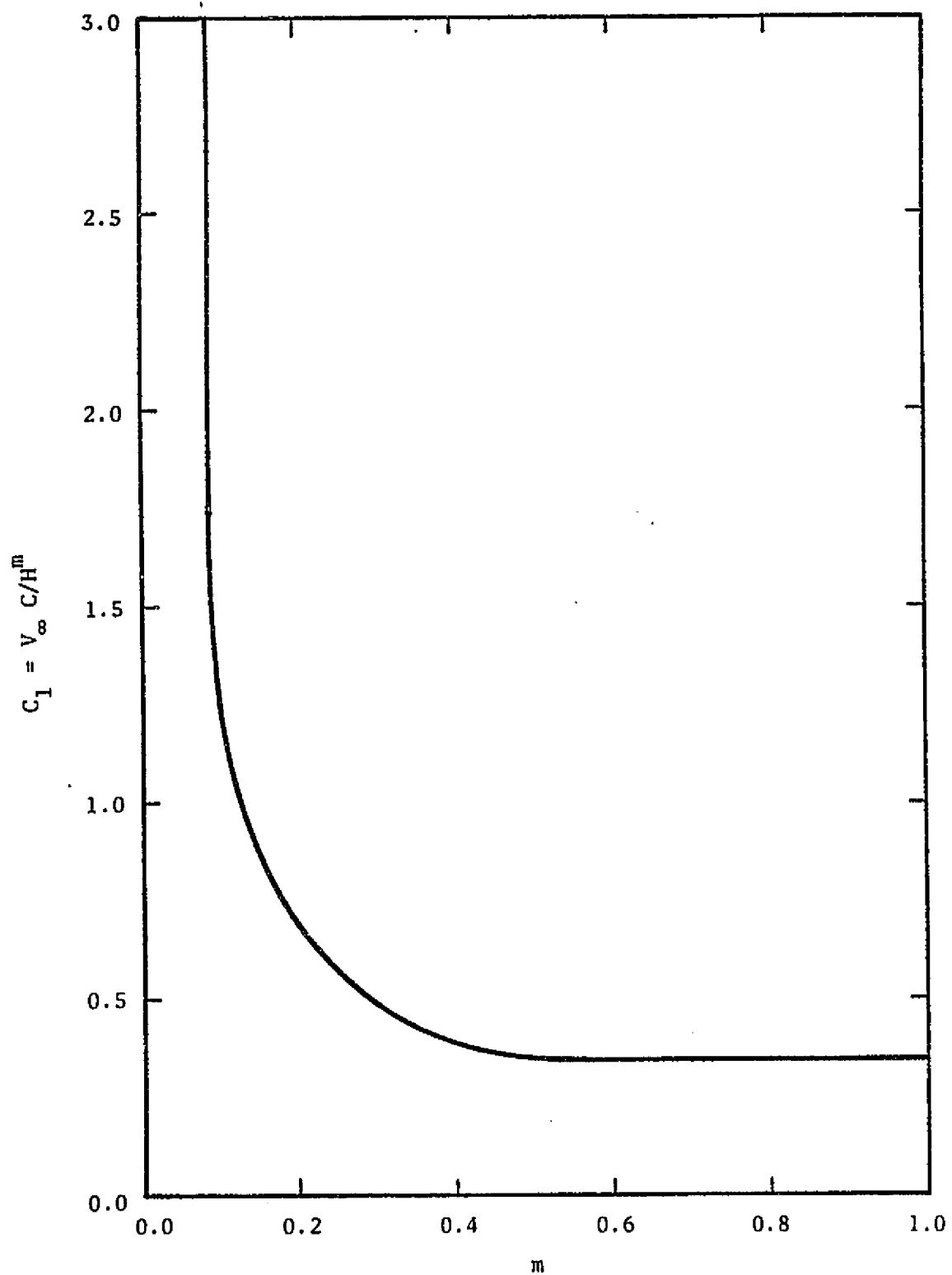


Figure B.1 Variation of the Constant for Flow Near the Stagnation Point of a Wedge